



Préparation de nanoparticules d'argent stabilisées par du dextran ou des amphiphiles oligosaccharidiques pour des applications en catalyse et biocapteurs

Renato Eising

► To cite this version:

Renato Eising. Préparation de nanoparticules d'argent stabilisées par du dextran ou des amphiphiles oligosaccharidiques pour des applications en catalyse et biocapteurs. Sciences agricoles. Université de Grenoble; UNIVERSIDADE FEDERAL SANTA CATARINA UFSC, 2013. Français. NNT : 2013GRENV006 . tel-00949189

HAL Id: tel-00949189

<https://theses.hal.science/tel-00949189>

Submitted on 19 Feb 2014

HAL is a multi-disciplinary open access archive for the deposit and dissemination of scientific research documents, whether they are published or not. The documents may come from teaching and research institutions in France or abroad, or from public or private research centers.

L'archive ouverte pluridisciplinaire **HAL**, est destinée au dépôt et à la diffusion de documents scientifiques de niveau recherche, publiés ou non, émanant des établissements d'enseignement et de recherche français ou étrangers, des laboratoires publics ou privés.



UNIVERSIDADE FEDERAL DE SANTA CATARINA
DEPARTAMENTO DE QUÍMICA - CFM
PROGRAMA DE PÓS-GRADUAÇÃO EM QUÍMICA
AND
UNIVERSITÉ DE GRENOBLE
ECOLE DOCTORALE CHIMIE ET SCIENCE DU
VIVANT



Renato Eising

**Preparation of Silver Nanoparticles Stabilized by Dextran and
Oligosaccharides-Based Amphiphiles for Application in Catalysis and
Sensors**

Thesis in cotutelle submitted to Programa de Pós-Graduação em Química da Universidade Federal de Santa Catarina and to Université de Grenoble for the obtention of Doctor Grade in Chemistry.

Supervisors:

Prof. Dr. Josiel Barbosa Domingos (UFSC)
Dr. Sébastien Fort (CNRS-Université de Grenoble)

Florianópolis - SC

2013

Ficha de identificação da obra elaborada pelo autor,
através do Programa de Geração Automática da Biblioteca Universitária da UFSC.

Eising, Renato

Preparation of silver nanoparticles stabilized by dextran and oligosaccharides-based amphiphiles for application in catalysis and sensors / Renato Eising ; orientador, Josiel Barbosa Domingos ; co-orientador, Sébastien Fort. - Florianópolis, SC, 2013.

139 p.

Tese (doutorado) - Universidade Federal de Santa Catarina, Centro de Ciências Físicas e Matemáticas. Programa de Pós-Graduação em Química.

Inclui referências

1. Química. 2. silver nanoparticles. 3. catalysis. 4. oligosaccharide-based amphiphiles. 5. dextran. I. Domingos, Josiel Barbosa. II. Fort, Sébastien. III. Universidade Federal de Santa Catarina. Programa de Pós-Graduação em Química. IV. Título.

Renato Eising

**Preparation of Silver Nanoparticles Stabilized by Dextran and
Oligosaccharides-Based Amphiphiles for Application in Catalysis
and Sensors**

Esta Tese foi julgada e aprovada para obtenção do título de
Doutor em Química, e aprovada em sua forma final pelo Programa de
Pós-Graduação em Química da Universidade Federal de Santa Catarina.

Florianópolis, 22 de abril de 2013.



Prof. Dr. Almir Spinelli
Coordenador do Programa

Banca Examinadora:



Dr. Josiel B. Domingos
Orientador - UFSC



Dr. Laurent David
Relator - UL1



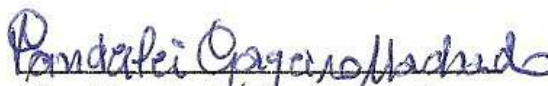
Dr. Redoune Borsali
Examinador - CNRS/UG



Dr. Sébastien Fort
Orientador - CNRS/UG



Dr. Paulo A. Z. Suarez
Relator - UnB



Dr. Vandereí G. Machado
Examinador - UFSC



UNIVERSIDADE FEDERAL
DE SANTA CATARINA

UNIVERSITÉ DE
GRENOBLE

THÈSE

Pour obtenir le grade de

DOCTEUR DE L'UNIVERSITÉ DE GRENOBLE

**préparée dans le cadre d'une cotutelle entre
l'Université de Grenoble et l'Universidade Federal
de Santa Catarina**

Spécialité : **Chimie Organique**

Arrêté ministériel : le 6 janvier 2005 -7 août 2006

Présentée par

« **Renato / EISING** »

Thèse dirigée par « **Sébastien/FORT** » et « **Josiel B./DOMINGOS** »

préparée au sein des **Laboratoires CERMAV et LaCBio**

dans le **École Doctorale Chimie et Sciences du Vivant et
Programa de Pós-Graduação em Química**

Préparation de nanoparticules d'argent stabilisées par dextran et amphiphiles à base d'oligosaccharides pour l'application en catalyse et capteurs

Thèse soutenue publiquement le « **22/04/2013** », devant le jury composé de :

M, Laurent, DAVID

Professeur Université de Lyon I (Rapporteur)

M, Paulo A. Z, SUAREZ

Professeur Universidade de Brasília - UnB (Rapporteur)

M, Sébastien, FORT

Chargé de Recherche CNRS/CERMAV (Directeur de thèse)

M, Josiel B., DOMINGOS

Professeur/ Universidade Federal de Santa Catarina (Directeur de thèse)

M, Redoune, BORSALI

Directeur de Recherche CNRS/CERMAV (Membre)

M, Vanderlei G., MACHADO

Professeur/ Universidade Federal de Santa (Président)

Université Joseph Fourier / Université Pierre Mendès France /
Université Stendhal / Université de Savoie / Grenoble INP



ACKNOWLEDGMENTS

After four years I am finishing an important period of my life. I could not accomplish this work without the assistance of many people which I am very grateful and I apologize if by chance I forget any name.

In first place I would like to thank God and my family, who supported me since the beginning to accomplish my studies. I also thank my supervisors Josiel Barbosa Domingos and Sébastien Fort by the opportunities, advices and friendship.

To my friends and colleagues at LaCBio, Lidiane, Tula, Aline, Welman, Eloah, Deonildo, Brunno, Kelly, Táбата, Caio, Juan, Marcelo, Juliano, Luciano, for their valuable contributions and discussions on the work and also for moments of relaxation, but I'm going to owe the article with the name of everyone, at least for now.

To my friends and colleagues at CERMAV specially in CBO team, Alex, Nathalie, Helene, Tinaig, Helene, Cony, Ludovic, Maud, Remi, Laurine, Marine-Océane, Stéphanie, Samuel, Patricia, Sami, Sylvain, Sylvie, Aurelie and Bernard, for the friendship and French lessons every day during my stay in Grenoble.

To Professor Edson Minatti, Professor Fernando Giacomelli, Cyrille Rochas and Christophe Travelet for the help with DLS and SASX techniques and the productive discussions about these techniques.

For the help in TEM analysis to Isabelle Pignot-Paintrand, in NMR analysis to Isabelle Jeacomine, mass spectrometry analysis to Stéphanie Boullanger, my thanks. For Grace and Jadir at UFSC and Isabelle Caldara for help with the administrative affairs.

To the jury members: Jean-Jaques Robin, Paulo A. Z. Suarez, Redoune Borsali and Vanderlei G. Machado for accepted to participate and their contributions.

To all my friends for their friendship and help, specially to Fabio Hansen, Ismael C. Bellettini, Aline C. de Mello, Alexander Guerri, Nathalie Claisse and Dino Zanette.

To CAPES and CNPq for the financial supporting.

"Debaixo do céu há tempo para tudo,
e um tempo certo para cada coisa."

SUMMARY

ACKNOWLEDGMENTS	VII
LIST OF FIGURES	XI
LIST OF TABLES.....	XV
LIST OF ABBREVIATIONS AND ACRONYSM.....	XVII
ABSTRACT	XIX
RÉSUMÉ	XXI
RESUMO.....	XXIII
1 Introduction.....	XXV
2 Bibliographic revision.....	27
2.1 Metal nanoparticles (M-NPs).....	27
2.2 M-NPs preparation and stabilization.....	28
2.3 Carbohydrates in the metal nanoparticles preparation	31
2.4 M-NPs catalytic activity	33
2.4.1 <i>p</i> -Nitrophenol (Nip) reduction.....	35
2.4.2 Silver nanoparticles (AgNPs)	36
2.4.3 Solvent effect.....	37
2.5 Biosensors for lectins recognition.....	38
3 Objective.....	41
4 Experimental section.....	43
4.1 Reactants and solvents.....	43
4.2 Materials, equipments and techniques	43
4.3 Multivariate analysis optimization in the preparation of silver nanoparticles stabilized by dextran (AgNPs-dextran).....	45
4.4 AgNPS-dextran catalytic activity.....	47
4.5 Oligosaccharide based amphiphiles synthesis.....	48
4.6 Multivariate analysis optimization in the preparation of silver nanoparticles stabilized by amphiphiles compounds synthesized (AgNPs-amphiphiles).....	57
4.7 AgNPs-amphiphiles catalytic activity.....	59
4.8 Lectin interaction detection with AgNPs-amphiphiles.....	59
5 Results and discussion	61
5.1 Silver nanoparticles stabilized by dextran polysaccharide	61
5.1.1 Silver nanoparticles preparation and characterization (AgNPs-dextran)	61
5.1.2 Catalytic activity of AgNPs-dextran.....	66
5.2 Silver nanoparticles stabilized by oligosaccharides-based amphiphiles.....	72
5.2.1 Synthesis of oligosaccharides-based amphiphiles	72
5.2.2 Preparation and characterization silver nanoparticles stabilized by oligosaccharides-based amphiphiles	77
5.2.3 Catalytic activity of AgNPs stabilized by oligosaccharides based amphiphiles	86
5.2.4 Lectins interactions with AgNPs stabilized by oligosaccharides based amphiphiles.....	93
6 Conclusions.....	99
7 Bibliography	101
8 Appendix.....	107
8.1 ANOVA table for AgNPs-Dextran optimization.....	107
8.2 ¹ H and ¹³ C NMR spectra for synthesized amphiphilic compounds.....	107

8.3 ANOVA table for AgNPs-Amphiphilic compounds optimization	117
8.4 Response surface for AgNPs-Amphiphilic compounds optimization.	119

LIST OF FIGURES

Figure 1. Illustration of surface atoms percentage with the particle size increase	27
Figure 2. A – In noble metal nanoparticles light induces collective oscillations of electrons ("Plasmon"). B – The scattering efficiency Q_{sca} , and the resonance wavelength are dependent on the exact particle shape, particle size and on the surrounding medium	28
Figure 3. Illustration of preparation methodologies for metal nanoparticles.	29
Figure 4. Stabilization of platinum nanoparticles by a hyperbranched polyglycerol	30
Figure 5. Scheme of stabilization electrostatic (left) and steric (right).	31
Figure 6. Electrosteric stabilization.	31
Figure 7: Example of metal glyconanoparticle	32
Figure 8. The two major mechanisms in heterogeneous catalysis: a) Langmuir-Hinshelwood; b) Eley-Rideal.....	34
Figure 9. Mechanistic model (Langmuir-Hinshelwood mechanism) of the reduction of Nip by borohydride in the presence of metallic nanoparticles (gray spheres)	36
Figure 10. Epoxidation reaction of ethylene catalyzed by Ag nanoparticles	37
Figure 11. 3D structure of lectin Concanavalin A.....	39
Figure 12. Dextran structure.	61
Figure 13: Response surfaces for the variables: (a) dextran and silver nitrate concentrations, (b) dextran and sodium borohydride concentrations and (c) silver nitrate and sodium borohydride concentrations	63
Figure 14. Correlation of absorbance with Ag-NP concentration.	64
Figure 15: UV-Vis spectrum of the optimal point	64
Figure 16: TEM micrograph and size distribution histogram for AgNPs-dextran	65
Figure 17: Dynamic light scattering autocorrelation function (squares) and relaxation-time distribution (solid line) for: (A) Ag-NPs-dextran and (B) dextran.	66
Figure 18. Reduction reaction of p-nitrophenolate to p-aminophenolate by NaBH_4 in presence of AgNPs.....	66
Figure 19: Variation in UV-Visible absorption spectra for the Nip reduction reaction at 25°C in the presence of AgNPs-dextran	67
Figure 20. A: Nip's absorption dependence versus time at 400 nm; B: The linear adjust of Fig. A for a first order kinetic..	67
Figure 21: k_{app} as a function of NaBH_4 concentration.....	68
Figure 22. k_{app} as a function of NaOH concentration	69
Figure 23: k_{app} as a function of Nip concentration.	70
Figure 24: k_{app} as a function of Ag-NP total surface area (S).....	71
Figure 25: General representation of different amphiphiles prepared.....	73
Figure 26: Reaction scheme to obtain the <i>N</i> -(maltosyl)-3-octanamide-1-propyne (MalNOcta) and the <i>N</i> -(maltosyl)-3-octadecylamide-1-propyne (MalNOctD).....	74
Figure 27: Reaction scheme to obtainment of ω -(4-((<i>N</i> -(oligosaccharide)acetamido)methyl)-1H-1,2,3,-triazole-1-yl) carboxylic acids (OliNAC).	76
Figure 28. Expected stabilization mechanism for the different kinds of amphiphile compounds prepared.....	77
Figure 29. Response surface for Mal ₇ NAC ₁₂	80

Figure 30. UV-vis spectra of all optimal conditions for AgNPs preparation.	81
Figure 31. TEM micrographs and size distribution histograms (insets) for (a) Ag-Mal ₇ NAC ₁₂ , (b) Ag-XGONAC ₆ and (c) Ag-XGONAC ₁₂ (d)MalNOctD (e) Ag-MalNAC ₁₂ (f) Ag-LacNAC ₁₂ (g)MalNOcta nanoparticles at the optimal synthesis conditions.	81
Figure 32. SAXS data (squares) and corresponding curve fitting (line) for(a) Ag-Mal ₇ NAC ₁₂ , (b) Ag-XGONAC ₆ and (c) Ag-XGONAC ₁₂ (d)MalNOctD (e) Ag-MalNAC ₁₂ (f) Ag-LacNAC ₁₂ (g) MalNOcta nanoparticles at the optimal synthesis conditions.	84
Figure 33. DLS autocorrelation function (squares) and relaxation-time distribution (solid line) for(a) Ag-Mal ₇ NAC ₁₂ , (b) Ag-XGONAC ₆ and (c) Ag-XGONAC ₁₂ (d)MalNOctD (e) Ag-MalNAC ₁₂ (f) Ag-LacNAC ₁₂ (g)MalNOcta nanoparticles at the optimal synthesis conditions.	85
Figure 34. Light scattering intensity and the hydrodynamic radius (R_h) versus MalNOcta concentration.	86
Figure 35. Plots of the apparent rate constant (k_{app}) as a function of water content in the composition mixtures with ethanol.	87
Figure 36. Plots of initial reaction rate (v_0) as function of $[NaBH_4]$ and $[Nip]$ for Ag-Mal ₇ NAC ₁₂ glyconanoparticles in (a) 75% and (b) 100% of water content in the solvent composition with ethanol.	88
Figure 37. Scheme of the reaction mechanism for monomolecular surface reactions.	88
Figure 38. Apparent rate constant (k_{app}) for Nip reduction reaction by $NaBH_4$, in the presence of Ag-Mal ₇ NAC ₁₂ glyconanoparticles, as a function of surface tension γ in different % water content in the solvent composition with ethanol.	90
Figure 39. Plots of the apparent rate constant (k_{app}) as a function of the surface area of Ag-NPs normalized to the unit volume of the system (S) for 100% and for 75% water in the solvent composition with ethanol.	91
Figure 40. Absorption spectra of Ag-Mal ₇ NAC ₁₂ and digital photography with a = 0; b = 0.0032; c = 0.0063; d = 0.0095; e = 0.0188; f = 0.0366 and g = 0.0701 mg mL ⁻¹ of Con A.	94
Figure 41. UV-vis spectral dependence of Ag-Mal ₇ NAC ₁₂ with time (a) and absorbance at 415 nm vs. time (b). In phosphate buffer.	95
Figure 42. Absorbance Ag-Mal ₇ NAC ₁₂ at 415 nm vs. Con A (■) and PNA (●) concentration.	96
Figure 43. Absorbance Ag-XGONAC ₁₂ at 415 nm vs. Con A (■) and PNA (●) concentration.	97
Figure 44. Absorbance Ag-LacNAC ₁₂ at 415 nm vs. Con A (■) and PNA (●) concentration.	98
Figure 45. ¹ H NMR (top) and ¹³ C NMR (down) of MalNOcta.	108
Figure 46. ¹ H NMR (up) and ¹³ C NMR (down) of MalNOctD.	109
Figure 47. ¹ H NMR (top) and ¹³ C NMR (down) of MalNAC ₆	110
Figure 48. ¹ H NMR (top) and ¹³ C NMR (down) of MalNAC ₁₂	111
Figure 49. ¹ H NMR (top) and ¹³ C NMR (down) of XGONAC ₆	112
Figure 50. ¹ H NMR (top) and ¹³ C NMR (down) of XGONAC ₁₂	113
Figure 51. ¹ H NMR (top) and ¹³ C NMR (down) of Mal ₇ NAC ₆	114
Figure 52. ¹ H NMR (top) and ¹³ C NMR (down) of Mal ₇ NAC ₁₂	115
Figure 53. ¹ H NMR (left) and ¹³ C NMR (right) of LacNAC ₁₂	116
Figure 54. Response surface for MalNOctD.	119
Figure 55. Response surface for MalNAC ₁₂	120
Figure 56. Response surface for XGONAC ₆	120
Figure 57. Response surface for XGONAC ₁₂	121
Figure 58. Response surface for Mal ₇ NAC ₆	121

Figure 59. Response surface for LacNAcC ₁₂	122
---	-----

LIST OF TABLES

Table 1. Factor levels in the AgNPs-dextran experimental design.	46
Table 2. Multivariate experiments combinations for AgNPs-dextran optimization concentrations in each optimization experiment.	47
Table 3. Factor levels in the experimental design.	58
Table 4. Multivariate optimization experimental design.	59
Table 5. Zeta potential (ζ) at different NaOH concentrations of Ag-NP-dextran in water solutions in the presence of NaBH_4	69
Table 6. Comparison between catalytic activities of silver nanoparticles systems in p-nitrophenol reduction.	72
Table 7. Yield obtained in the amphiphiles synthesis.	75
Table 8. Regression coefficients of surface curves, lack of fit and the coefficient determination (R^2).	79
Table 9. Optimal concentrations of stabilizer and NaBH_4 for each system.	80
Table 10 . Diameter of AgNPs obtained by transmission electron microscopy (TEM), small angle X-ray scattering (SAXS) and dynamic light scattering (DLS)	82
Table 11 . Rate constants and adsorption constants of Nip and BH_4^-	89
Table 12. Comparison between catalytic activities of silver nanoparticle systems in p-nitrophenol reduction.	92
Table 13. Detection limits comparison for Con A determination with various lectin biosensing methods.	96
Table 14. Analysis of variance (ANOVA) for AgNPs-Dextran optimization	107
Table 15. Analysis of variance (ANOVA) for AgNPs-MalNOctD optimization.	117
Table 16. Analysis of variance (ANOVA) for AgNPs-MalNAC ₁₂ optimization.	117
Table 17. Analysis of variance (ANOVA) for AgNPs-XGONAC ₆ optimization.	117
Table 18. Analysis of variance (ANOVA) for AgNPs-XGONAC ₁₂ optimization.	118
Table 19. Analysis of variance (ANOVA) for AgNPs-Mal ₇ NAC ₆ optimization.	118
Table 20. Analysis of variance (ANOVA) for AgNPs-Mal ₇ NAC ₁₂ optimization.	118
Table 21. Analysis of variance (ANOVA) for AgNPs-LacNAC ₁₂ optimization.	119

LIST OF ABBREVIATIONS AND ACRONYSM

[]	concentration
¹³ C RMN	nuclear magnetic resonance of carbon
¹ H RMN	nuclear magnetic resonance of hydrogen
AgNPs	silver nanoparticles
AgNPs-dextran	silver nanoparticles stabilized by dextran
A _{max}	maximum absorbance
Amp	<i>p</i> -aminophenol
ANOVA	analysis of variance
Au-GNPs	gold-based glyconanoparticles
AuNPs	gold nanoparticles
CGTase	cyclodextrin glycosyltransferase
Con A	Concanavalin A
CTAB	cetyltrimethylammonium bromide
DCC	<i>N,N'</i> -dicyclohexylcarbodiimide
DLS	dynamic light scattering
D _m	medium diameter
DMF	<i>N,N</i> -dimethylformamide
DS	degree of substitution
FWHH	full width at half-height
Gal	galactose
Glc	glucose
<i>k_{app}</i>	apparent kinetic rate constant
Lac	lactose
LacNAcC ₁₂	(((<i>N</i> -(lactosyl))acetamido)methyl)-1 <i>H</i> -1,2,3-triazol-1yl)dodecanoic acid
Mal ₇	maltoheptaose
Mal ₇ NAcC ₁₂	(((<i>N</i> -(Maltoheptaosyl))acetamido)methyl)-1 <i>H</i> -1,2,3-triazol-1yl)dodecanoic acid
Mal ₇ NAcC ₆	(((<i>N</i> -(Maltoheptaosyl))acetamido)methyl)-1 <i>H</i> -1,2,3-triazol-1yl)hexanoic acid
MalNAcC ₁₂	(((<i>N</i> -(Maltosyl))acetamido)methyl)-1 <i>H</i> -1,2,3-triazol-1yl)dodecanoic acid
MalNAcC ₆	(((<i>N</i> -(Maltosyl))acetamido)methyl)-1 <i>H</i> -1,2,3-triazol-1yl) hexanoic acid
MalNOcta	<i>N</i> -maltosyl-3-octanamide-1-propyne

MalNOctD	<i>N</i> -maltosyl-3-octadecylamide-1-propyne
M-NPs	metal nanoparticles
MS ESI	mass spectrometry with electrospray ionization
MS MALDI-TOF	mass spectrometry with Matrix-Assisted Laser Desorption/Ionisation and time-of-flight
MS	mass spectrometry
Nip	<i>p</i> -nitrophenol
NP	nanoparticle
<i>p</i>	statistic probability
PtNPs	platinum nanoparticles
R ²	determination coefficient
R _g	radius of gyration
R _h	hydrodynamic radius
RSM	response surface methodology
SAXS	small-angle X-ray scattering
SLS	static light scattering
SPR	surface Plasmon resonance band
t.l.c.	thin layer chromatography
TEM	transmission electronic microscopy
THF	tetrahydrofuran
TTAB	tetradecyltrimethylammonium bromide
UV-Vis	ultraviolet-visible spectroscopy
XGO	xyloglucan oligosaccharide
XGONAcC ₁₂	(((<i>N</i> -(XGO))acetamido)methyl)-1 <i>H</i> -1,2,3-triazol-1yl)dodecanoic acid
XGONAcC ₆	(((<i>N</i> -(XGO))acetamido)methyl)-1 <i>H</i> -1,2,3-triazol-1yl)hexanoic acid
Xyl	xylose
λ _{max}	wavelength at A _{max}

ABSTRACT

The main goal of this work is the preparation, characterization and catalytic and lectins detection studies of silver nanoparticles (AgNPs) having sugar-based compounds as stabilizers. To achieve this goal two strategies were used, one using the polysaccharide dextran as stabilizer and other using amphiphile compounds based on oligosaccharides (maltose, lactose, maltoheptaose and xyloglucan). In both strategies the optimization of AgNPs preparation was realized using a multivariate analysis based in informations collected from the surface Plasmon resonance band (SPR) of AgNPs. All stable AgNPs were characterized by ultraviolet-visible spectroscopy (UV-vis), transmission electron microscopy (TEM), small angle X-ray scattering (SAXS) and dynamic light scattering (DLS) techniques. The catalytic activities of AgNPs were determined over the *p*-nitrophenol reduction reaction by NaBH₄, as reducing agent, in water or water-ethanol mixtures.

Two different types of amphiphiles were synthesized, one with an alkyne group in the junction of a sugar block with a hydrophobic block and the other with a carboxylic acid group in the end of hydrophobic part. The amphiphiles were characterized by ¹H and ¹³C NMR and mass spectrometry.

The Nip reduction reaction with NaBH₄ showed the best catalytic activity with AgNPs-dextran and Ag-Mal₇NAC₁₂ nanoparticles with the rate constant normalized to the surface area of the NPs per unit volume of 1.41 and 1.11 s⁻¹ m⁻² L, respectively. These values are among the highest ones found in literature. The solvent effect in this reaction was evaluated by mixtures of water and ethanol. Applying a *pseudo*-monomolecular surface reaction as an experimental artifice, the obtained kinetic data were treated according to the Langmuir model, which combined with water/ethanol surface tension observations revealed that addition of ethanol inhibit the reaction, most probably by competing with BH₄⁻ ions for the nanoparticles surface, with the formation of a solvent monolayer.

Finally, three different systems (Ag-Mal₇NAC₁₂, Ag-XGONAC₁₂ and Ag-LacNAC₁₂) were tested as sensor for lectin detection and Ag-Mal₇NAC₁₂ nanoparticles showed specific interaction with the Concanavalin A.

RÉSUMÉ

L'objectif principal de ce travail est la préparation de nanoparticules d'argent (AgNPs) stabilisées par des oligo-et polysaccharides et leur application en catalyse et pour la détection de lectines. Pour atteindre cet objectif, deux stratégies ont été utilisées, l'une utilisant le polysaccharide dextran comme stabilisant et l'autre utilisant des composés amphiphiles oligosaccharidiques dérivés du maltose, lactose, maltoheptaose et du xyloglucane. Dans les deux stratégies, la préparation des nanoparticules AgNPs a été optimisée en réalisant une analyse multifactorielle basée sur l'étude de la bande de résonance plasmonique de surface (SPR) des nanoparticules. Toutes les suspensions colloïdales stables de nanoparticules ont été caractérisées par spectroscopie ultraviolet-visible (UV-vis), microscopie électronique à transmission (TEM), diffraction des rayons X aux petits angles (SAXS) et par diffusion dynamique de lumière (DLS).

Les activités catalytiques des nanoparticules ont été déterminées pour la réaction de réduction du *p*-nitrophénol (Nip) par NaBH_4 , dans l'eau ou dans des mélanges eau-éthanol. Parmi les différentes nanoparticules préparées, celles stabilisées par du dextran ou par le dérivé de maltoheptaose $\text{Mal}_7\text{NAC}_{12}$ ont montré les meilleures propriétés catalytiques pour la réduction du Nip par NaBH_4 avec des constantes de vitesse respectives de 1,41 et 1,11 $\text{s}^{-1} \text{m}^{-2} \text{L}$. Ces valeurs sont parmi les plus élevées de la littérature. L'effet du solvant et notamment de la présence d'éthanol sur les propriétés catalytiques des nanoparticules a également été évalué. Il a été montré que la présence d'éthanol inhibe l'activité des nanoparticules, probablement par formation d'une couche de solvant à la surface des particules entrant en compétition avec le réducteur.

Enfin, trois systèmes différents (Ag- $\text{Mal}_7\text{NAC}_{12}$, Ag- XGONAC_{12} et Ag- LacNAC_{12}) ont été évalués comme biocapteurs potentiels pour la détection de lectines. Les nanoparticules Ag- $\text{Mal}_7\text{NAC}_{12}$ en particulier ont permis la détection colorimétrique et sans marquage de la Concanavaleine A.

RESUMO

O objetivo principal deste trabalho é a preparação, caracterização e estudos catalítico e de detecção de lectinas por nanopartículas de prata (AgNPs) tendo compostos a base de açúcares como estabilizantes. Para atingir esse objetivo duas estratégias foram utilizadas, uma usando o polissacarídeo dextrana como estabilizante e outra usando compostos anfifílicos baseados em oligossacarídeos (maltose, lactose, maltoheptaose e xiloglucano). Em ambas estratégias, a otimização da preparação das AgNPs foi realizada utilizando-se análise multivariada baseada nas informações coletadas a partir da banda de ressonância de Plasmon de superfície (SPR) das AgNPs. Todas as AgNPs estáveis foram caracterizadas pelas técnicas de espectroscopia de ultravioleta-vísivel, (UV-Vis), microscopia eletrônica de transmissão (TEM), espalhamento de raios X a baixos ângulos (SAXS) e espalhamento de luz dinâmico (DLS). A atividade catalítica das AgNPs foram determinadas frente a reação de redução do *p*-nitrofenol (Nip) por NaBH₄, como agente redutor, em água e misturas de água/etanol.

Dois tipos diferentes de anfifílicos foram sintetizados, um com grupo alquino na junção do bloco de açúcar com o bloco hidrofóbico e outro tipo com um grupo ácido carboxílico no final da parte hidrofóbica. Os anfifílicos foram caracterizados por ¹H e ¹³C NMR e espectrometria de massas.

A reação de redução do Nip por NaBH₄ teve a melhor atividade catalítica com as nanopartículas AgNPs-dextran e Ag-Mal₇NAC₁₂, com constante de velocidade normalizada para a área superficial das NPs por unidade de volume de 1,41 e 1,11 s⁻¹ m⁻² L, respectivamente. Estes valores estão entre os maiores descritos na literatura. O efeito do solvente nesta reação foi avaliado por misturas de água e etanol. Aplicando uma reação superficial *pseudo*-monomolecular como um artifício experimental, os dados cinéticos obtidos foram tratados de acordo com o modelo de Langmuir, que combinados com observações de tensão superficial de misturas de água/etanol, revelaram que a adição de etanol inibe a reação, provavelmente pela competição com os íons BH₄⁻ pela superfície da nanopartícula, com a formação de uma monocamada de solvente.

Finalmente, três sistemas diferentes (Ag-Mal₇NAC₁₂, Ag-XGONAC₁₂ e Ag-LacNAC₁₂) foram testados como sensores para detecção de lectinas e somente Ag-Mal₇NAC₁₂ mostrou interação específica com a Concanavalina A.

1 Introduction

Metal nanoparticles (M-NPs) have been subject of great interest in the academic and industrial research because they have surface area by volume or mass unit greater than bulk metal.¹ This property gives to M-NPs fascinating physico-chemical properties which, in turn, are sharply dependent on their sizes and morphologies.² In particular, metal nanoparticles have been widely explored for their exceptional optical, electrical and magnetic properties² and their potential application in catalysis,³ information storage,⁴ biological classification⁵ and Surface-Enhanced Raman Scattering (SERS).⁶

As the catalysis is a key area in the developing of chemical products, the utilization of M-NPs as catalysts have attracted many attention in last years, due their high selectivity, efficient and recycling possibility; fulfilling the green catalysis requirements.⁷ Recently, Virkutyte and Varma⁸ did an interesting comparison between nanotechnology and green chemistry, declaring that the main objective of both is to obtain processes that resemble cells or ecosystems where benign materials are used at room temperature, chemical reactions are performed in water (instead of using toxic and hazardous solvents), wastes are recycled and energy is efficiently utilized. The development of new M-NPs methodology preparation and its application in new reactions is a broad and unrestricted research field.

In terms of M-NPs preparation, stabilizers utilization is fundamental, since they adsorb on the particle surface forming a protective layer. Otherwise, M-NPs obtained without stabilizers presence (as surfactants, polymers, etc.) are thermodynamically unstable and tend to aggregate. The choice of the functional groups in the structure of the stabilizer is very important because they can help to control the size of M-NPs and the modification of their physical and chemical properties.⁹⁻¹⁰ Specifically regarding catalysis, functionalized stabilizers become attractive since the catalytic activity of M-NPs may be the result of the combined properties of the metallic core and stabilizer.¹⁰⁻

11

As choice of functional groups to stabilize M-NPs for catalysis, groups such as amines, alcohols and carboxylic acids and their salts have been preferred since they show a better relationship between stability and catalytic activity, while groups which interact strongly with M-NPs, such as thiols, can poison the surface of the nanoparticle and decrease its catalytic activity.¹² In this context, the use of polysaccharides, oligosaccharides and their derivatives become extremely interesting by the abundance of hydroxyl groups, the relative simplicity of derivatives preparation and because they are obtained from natural and renewable sources, which is aligned with the green chemistry ideas.¹³

Currently, the works on catalytic M-NPs are dedicated to improve their catalytic properties, to increase their selectivity and to understand catalytic mechanisms.¹¹ In this work, we seek to contribute to the state-of-the-art in the preparation of new M-NPs catalysts based on: (i) the use of multivariate analysis optimization in AgNPs preparation, (ii) the use of stabilizers based on sugar structures, and (iii) the determination of their catalytic properties in the reduction reaction of *p*-nitrophenol (Nip). Additionally, some of these sugars based AgNPs were tested as sensor for lectin recognition.

2 Bibliographic revision

The prefix nano means, by the International System of Measures, 10^{-9} i.e. 1/1000000000. So small, in fact, that a nanosized structure must be expanded more than 10 million times to be able to observe details in its structure. Nanotechnology refers to technologies in which matter is manipulated at atomic and molecular scale to create new materials and processes with different functional characteristics of common materials. It is not only the study of nano-sized materials, but also the practical application of this knowledge in the development of new materials.

2.1 Metal nanoparticles (M-NPs)

The metal nanoparticles preparation and utilization have attracted interest from various knowledge areas due to its exceptional characteristics (electrical, magnetic, optical and catalytic), which differ greatly from the properties presented by these metals when in bulk phase.¹⁴⁻¹⁶ Thus, they can be employed as catalyst, sensor and biosensors.¹⁷⁻²¹ Also, by having a large surface area per volume or mass unit, M-NPs have great catalytic potential and industrial interest.¹

In contrast with bulk phase metals, M-NPs have high percentage of their atoms in the surface (Figure 1). As the volume of an object ($V \propto r^3$) decreases more rapidly than its surface area ($S \propto r^2$) as its size decreases, the decrease in the M-NPs radius results in the increasing of the atoms' number of in nanoparticles surface, leading (in extreme cases) to particles with atoms majority at the interface. So, the M-NPs can reach sizes where their physical and chemical properties depend only of atoms at the surface.²² The atoms on the surface of an M-NP experience an environment different from that inside the cluster, and thus, have different free energy, electronic states, reactivity and mobility.²³






Full-Shell "Magic Number" Clusters					
Number of shells	1	2	3	4	5
Number of atoms in cluster	M ₁₃	M ₅₅	M ₁₄₇	M ₃₀₉	M ₅₆₁
Percentage surface atoms	92%	76%	63%	52%	45%

Figure 1. Illustration of surface atoms percentage with the particle size increase (from ref.¹⁶).

Large metal masses have their properties driven by energy bands, but deviate from the ideal behaviour when their size is reduced, so the electrons mean free pathway exceeds the particle size.

In this case the electrons can be excited by visible light.²⁴ The interaction with electromagnetic radiation causes a collective oscillation of the conduction electrons, inducing the formation of dipole moments by the surface charging (Figure 2). A restoring force in the nanoparticles attempts to compensate this effect, resulting in only one resonant wavelength, generating a band of surface Plasmon resonance.

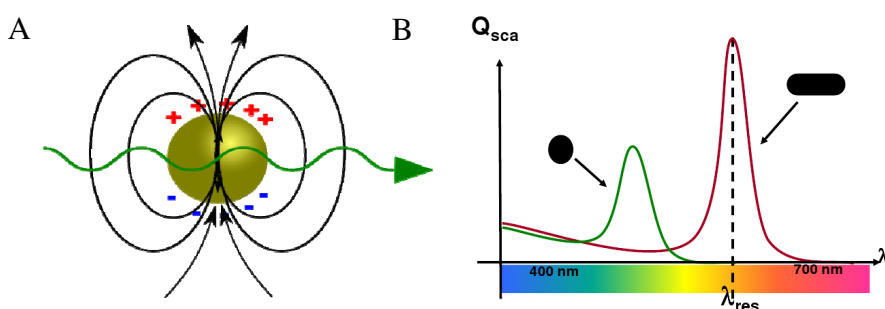


Figure 2. A – In noble metal nanoparticles light induces collective oscillations of electrons ("Plasmon"). B – The scattering efficiency Q_{sca} , and the resonance wavelength are dependent on the exact particle shape, particle size and on the surrounding medium.²⁵

Not all metals show Plasmon resonance, due to the necessity of the presence of free conduction electrons, like gold, silver and copper, for example. The oscillation wavelength depends on several factors such as particle's size and shape, as well as the medium in which it is located (dielectric constant) and the distance between the particles.²⁶

2.2 M-NPs preparation and stabilization

Many preparation strategies, adopting chemical and physical methods have been reported for the M-NPs preparation.²⁷⁻³¹ In general, the material structure formation provides favourable energy for the particle growth, but removal of this activation energy (by decreasing the temperature of the system, for example) results in an "interrupted" growth and thus, it is possible to kinetically control the particle size.³⁰

The methodologies of M-NPs preparation can be divided in physical and chemical methods (Figure 3). One physical method of particle preparation is the evaporation of a metal by heating or irradiating with laser. A disadvantage of this method is that the metal nanoparticles are generated without coating, having a high surface energy, leading to the immediate aggregation in the polycrystalline powder form, thermodynamically favoured by the metal-metal bonds formation.²⁷

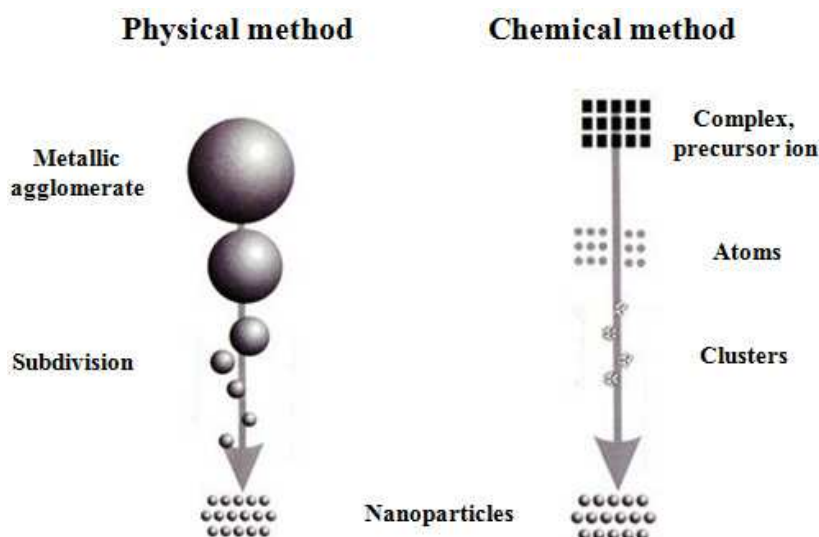


Figure 3. Illustration of preparation methodologies for metal nanoparticles.

On the other hand, the chemical method is based in a metal salt reduction in the presence of a stabilizer in solution.^{29, 32} Faraday, in 1857, was the first to publish the chemical reduction of a metal salt to form metal colloids in water.³³ However, it was just a century later that Turkevich described the first standard procedure to prepare colloidal gold reduced and stabilized by citrate.³⁴

Although different reducing agents can be used, such as hydroquinone,¹⁰ NaBH_4 ³⁵ and sugars,³⁶ the suitable reducer choice is very important, since their reductive ability determines the kinetics formation of M-NPs. The driving force in the metal reduction reaction is the redox potential difference, ΔE . The ΔE magnitude determines the equilibrium constant value for the reaction (K_e), according to the Nerst equation for a chemical equilibrium:

$$\text{Equation 1. } \ln K_e = \frac{nF\Delta E}{RT}$$

where n is the number of electrons transfer, F is the Faraday constant, R is general gas constant and T is temperature.

The reduction is thermodynamically possible only when $\Delta E > 0$, determining that the reducing agent potential redox is smaller than that of the metal species involved, and this redox potential difference must be higher than 0,3-0,4 V.³⁷ Thus strong reducing agents such as borohydride, tend to form M-NPs rapidly and with small size, while weak reducers, such as alcohols, reduce the metal precursor slowly producing M-NPs with larger sizes.

Stabilizers are molecules used to thermodynamically stabilize metal nanoparticles, forming a coat, generally a monolayer, self-organized on its surface preventing the growth and coalescence (Figure 4). In addition to controlling the size and shape of the nanoparticles, such stabilizers (such

as surfactants) may "functionalize" them, changing their chemical behaviour, for example, altering its solubility by varying the nature of the stabilizing layer. Examples of organic molecules used contain functional groups such as quaternary ammonium salts, amines, isothiocyanates, alcohols and thiols.³⁸

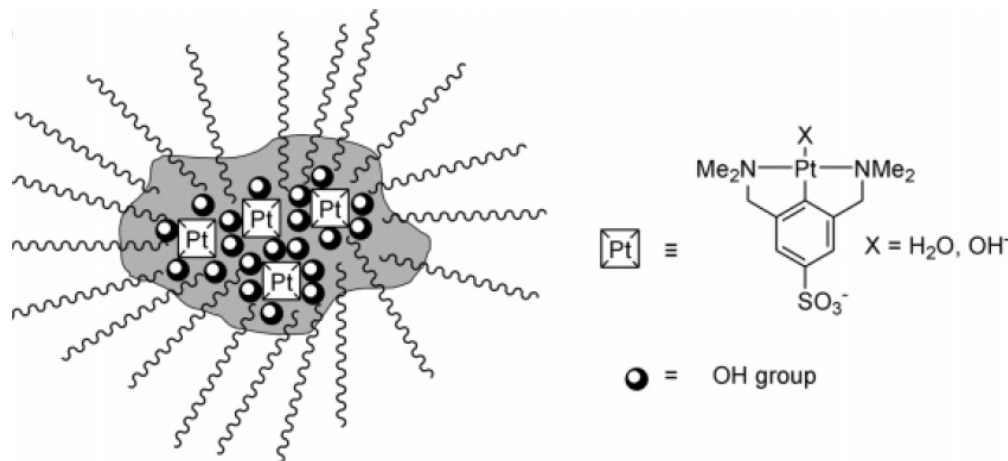


Figure 4. Stabilization of platinum nanoparticles by a hyperbranched polyglycerol.³⁹

Proper choices of stabilizing agent is of great importance, in addition to stabilize the M-NPs, it has an essential role in the growth control of M-NPs.⁴⁰ For example, if the stabilizer is weakly associated with M-NPs, the protection offered is very low or absent and, consequently, the M-NPs formed continue to grow resulting in large crystals, or will aggregate and it may precipitate. However, if the stabilizer interacts strongly with M-NPs it can limit or stop the growth process or even hamper its use for certain applications.^{12, 41}

In the colloids stabilization, as M-NPs, two distinct mechanisms are normally used: steric and electrostatic stabilization (Figure 5). In the first mechanism the stabilization is caused by a thermodynamic barrier, indicated by a positive variation in the Gibbs energy, as result of conformation entropy decrease of the chains, with size a , when two drops are approaching a distance equal to or less than $2a$.⁴² The electrostatic stabilization is based in the resulting repulsion from the beginning of overlap of the electrical diffuse double layers around the M-NPs. The ionic stabilizers, when present on the interface, induce the appearance of electrical charges in the region. Next to interface is formed an electrical potential which causes preferential accumulation of ions of opposite charge to the interface (counter ions), which in turn attract charged ions equal to the interface (co-ions). This set of ions forming a concentration gradient, which dissipates as it moves away from the interface, and it is known as the diffuse double layer and is responsible for electrostatic repulsion.⁴²

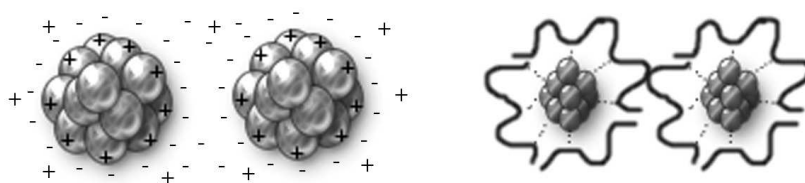


Figure 5. Scheme of stabilization: electrostatic (left) and steric (right).

The combination of the two mechanisms, steric and electrostatic, in the M-NPs stabilization is also much used. The electrosteric stabilization, it is generally achieved by the use of polyelectrolytes or ionic surfactants (Figure 6).⁴²

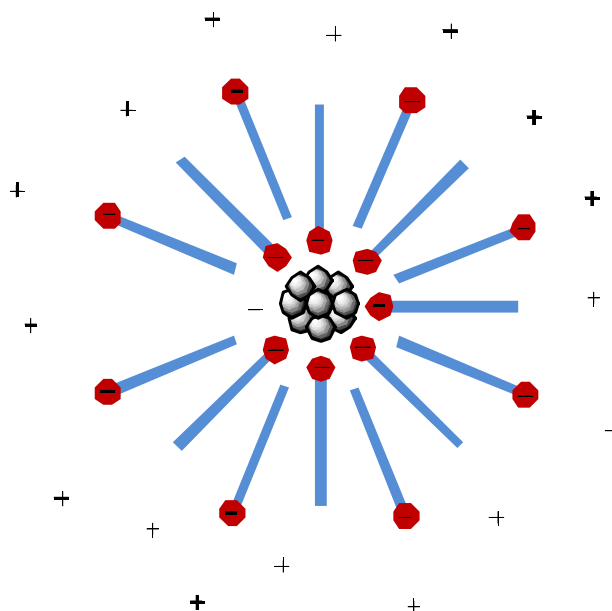


Figure 6. Electrosteric stabilization.

2.3 Carbohydrates in the metal nanoparticles preparation

Each year, plants synthesise about 4×10^{11} tons of carbohydrates.⁴³ Oligosaccharides and polysaccharides are carbohydrate based compounds, where each sugar unit is linked to the next by glycosidic bonds. Oligosaccharides and polysaccharides have many different functional groups including hydroxyl and a hemiacetal reducing end, which is capable of reducing precursor salts.

The Tollens reaction is widely known and used in reducing sugars determination. This reaction consists in the oxidation of an aldehyde in basic medium to reduce silver ions into the corresponding metal that is deposited in the flask bottom forming a silver mirror. This reaction has

been used in the preparation of silver nanoparticles with size and shape controlled by the stoichiometry of complexing agent (ammonia) and silver ions.^{36, 44-45} Panacek and col. demonstrated that in addition to reduce silver ions, monosaccharides and disaccharides as glucose, maltose lactose and galactose can act as stabilizers.³⁶

In the last years, the interest in M-NPs conjugated with ligands or biomolecules of biological importance has grown due to promising applications in biomedicine and bioanalytical, surfaces transformations and biocompatibility.⁴⁶ In this context, the glyconanoparticles (Figure 7), which are metal nanoparticles decorated with sugars, are of particular interest because they allow new tools in the recognition study of carbohydrates by enzymes and proteins.⁴⁶

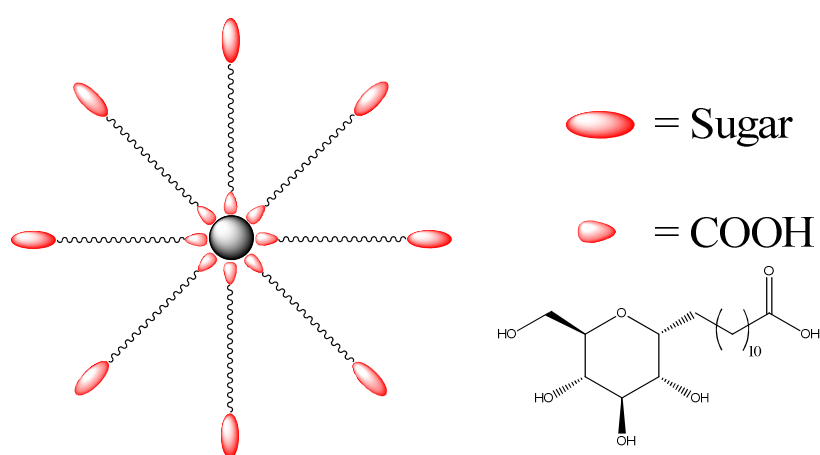


Figure 7: Example of metal glyconanoparticle.⁴⁶

Recently, amphiphiles based on lipids and sugars have attracted attention for their distinctive characteristics. The glycolipids, as they have been called, are able, for example, to reduce certain metal salts in basic pH conditions without the aid of an external reducer.⁴⁶⁻⁴⁸ The reduction mechanism, however, is still not entirely clear, although a mechanism very close to the polyol is most probable.⁴⁷

Polysaccharides are natural polymers formed by carbohydrates with dozens, hundreds or even thousands of monosaccharides units joined by glycoside bonds. They are found in all living organisms, constituting the most abundant and important group of compounds in the biosphere. As examples of polysaccharides are cellulose and starch in plants and glycogen and chitin in animals.⁴⁹

When in solution, polysaccharides can show different conformations, as for example single-helix, double-helix, triple-helix, random coil and aggregates.⁵⁰⁻⁵¹ Modifications in the medium properties, as temperature, ionic strength, pH and others, can promote morphologic transitions in polysaccharide chain conformation.

Due to these characteristics, different polysaccharides have been employed in M-NPs preparation and stabilization. The most used are chitosan and cellulose and its derivatives due to

their easy availability and relative abundance.⁵²⁻⁵⁶ However, studies that use less abundant polysaccharides but have branches in its structure are gaining force in the literature. Li and col.⁵⁷ for example, studied the behaviour of silver nanoparticles (AgNPs) stabilized by lentinan in aqueous media. They prepared AgNPs about 12 nm of diameter, with NaBH₄ as reducer and stabilized by lentinan in triple-helix form. This system is stable for nine months at room temperature; however, NaOH addition causes structural changes in the lentinan, which passes to random coil form without affect size and shape of the AgNPs. On the other hand, this lentinan structural change can be followed by the AgNPs SPR band alterations, making it an excellent method to monitor aggregation in these systems.

2.4 M-NPs catalytic activity

Nanostructured metal colloids hydrophilic or lipophilic, in organosol or hydrosols form, can act as catalysts in organic or aqueous solutions, respectively. These systems can be used as catalyst precursors applicable in homogeneous phase as well as heterogeneous phase.¹¹

Metallic nanoparticles are usually used at low temperatures, as in homogeneous catalysis. In this regard, metal nanoparticles are similar to enzymes and are considered in many cases artificial enzymes. From the green chemistry viewpoint (less energy, less by-products, higher efficiency, higher selectivity, etc.), enzymes are good models for industrial catalysts.¹

The application of catalytic M-NPs stabilized by polymers has attracted interest due to possible interactions with the substrate molecules, increasing the reaction rate and / or selectivity by choosing a particular substrate. For example, acids polymers (or basic) can concentrate basic substrates (or acid) near the metal nanoparticles, which can lead to an increase in reaction rate. Those promoting molecular recognition, as well as those having hydrophobic sites are also of great interest.^{1, 58}

Although nanocatalysts can be selective and efficient and have potential to be recycled (i.e. meet the prerequisites for green catalysis), determining the nanocatalyst nature in solution is not trivial, since the interfacial region of nanoparticle surface is not well understood.^{7, 59} Colloidal M-NPs exhibit solutions properties, such as mobility, and solid phase properties, such as liquid-solid interface. If the catalysis occurs on the nanoparticle surface it is defined as heterogeneous; if the nanoparticle provides a complex to the solution that, subsequently, will lead to catalysis, away from the nanoparticle surface, then it is classified as homogeneous catalysis.⁵⁹ However, some authors have called the catalysis by M-NPs as semi-heterogeneous⁶⁰ or quasi-homogeneous.^{11, 59}

The two major models to describe heterogeneous catalysis are the Langmuir-Hinshelwood and the Eley-Rideal models. The first assumes that the reactants (A and B) must be adsorbed on the catalyst surface before reacting, as seen in Figure 8a. The reaction occurs in the active site and the product C is desorbed from catalyst surface and returns to the solution. It is interesting to note that it is a good description of many (but not all) homogeneous catalysis and also biocatalysis reactions. What happens is the reactant or substrate first coordinates to the metal complex or enzyme and then the reaction occurs, finally the product dissociates from the catalyst and diffuses back into solution.⁶¹ In another mechanism, the Eley-Rideal (Figure 8b), the reactant A is adsorbed in the catalyst surface and B reacts directly with A, without adsorbing, to form C. The first mechanism cited, the Langmuir-Hinshelwood, is much more common, partially because many reactants are activated by the adsorption in the catalyst surface.⁶¹

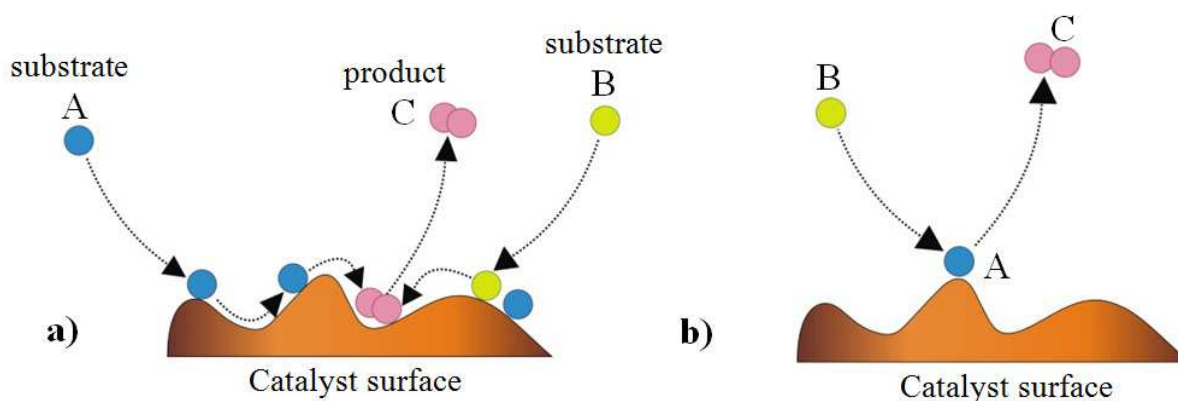


Figure 8. The two major mechanisms in heterogeneous catalysis: a) Langmuir-Hinshelwood; b) Eley-Rideal.

Colloidal nanocatalysts combine the advantages of homogeneous and heterogeneous catalysis, and contour many of its individual drawbacks. The drawbacks of homogeneous catalysis include the low potential for recycling and contamination of the products by the catalyst (which often means the catalyst loss). The heterogeneous catalysis in solution alleviates these drawbacks, however, the turnover frequency (TOF) of these catalysts are much lower when compared with their homogeneous catalyst counterparts. This lower catalytic ability of heterogeneous catalysts is attributed to the low number of active sites per volume of catalytic material, because only the surface atoms participate directly in catalysis. The use of M-NPs colloidal softens this dimensional limitation because these catalysts have high ratios surface / volume compared to those presented by heterogeneous supporters.⁵⁹

There are two kinds of reactions that demonstrate the main results involving M-NPs in catalysis: redox reactions and carbon-carbon bond formation reactions.⁵⁹ Among the redox

reactions, the more studied are the catalytic reduction-oxidation of organic compounds⁵⁹ (for example: nitroaryls, as *p*-nitrophenol,⁶² alcohols, as *p*-hydroxybenzyl alcohol⁶³ and hydrogenation reactions⁶⁴). These reactions are of great importance since the nitro compounds are reduced to their less toxic amino equivalents,⁶⁵ the methanol electro-oxidation is used in fuel cells⁶⁶ and the olefins hydrogenation is very important in the petrochemical industry.⁶⁷⁻⁶⁸ Many metals are used in redox reactions catalysis; the most common studied are platinum, gold and silver.⁵⁹

2.4.1 *p*-Nitrophenol (Nip) reduction

In the nitro-compounds class, the *p*-nitrophenol (Nip) reduction to *p*-aminophenol (Amp) has been used as model reaction to demonstrate the M-NPs catalytic activity.⁶⁹⁻⁷⁰ The presence of nitrophenols in wastewaters is an important concern due to their high toxicity and they are in the priority list of the Environmental Protection Agency (EPA) of the United States (USA).⁷¹ Nitrophenol derivatives are mainly used to prepare drugs, fungicides, dyes, darkening leathers, etc. Nip, however, is associated with some undesirable properties like irritation of the eyes, skin, and respiratory tract and may cause inflammation of those parts.⁷¹ In the other hand, Amp is an important intermediate in drugs synthesis, as acetaminophenol and phenacetin; a strong reducing agent and is used as a photographic developer; it is also used as a corrosion inhibitor in paints and anticorrosion-lubricating agent in fuels for two-cycle engines, and in the dye industry, Amp is used as a wood stain, imparting a rose-like colour to timber, and as a dyeing agent for fur and feathers.⁷²⁻⁷³ Due to the Amp importance, there is demand for direct catalytic hydrogenation of this compound,⁷² and it is important to point that NaBH₄ can not reduce Nip without presence of a catalyst.⁶⁵

Recently, our research group has used the Nip reduction by NaBH₄ as reaction model to evaluate the catalytic activity of silver nanoparticles (AgNPs) stabilized by polymers.^{10, 74-75} Besides the aforementioned economic relevance, this reaction was chosen due to the facility to follow it by UV-Vis spectrometry. There are several studies that tried to elucidate the Nip reduction reaction mechanism using M-NPs as catalysts.⁷⁶⁻⁸⁰ Wunder and col.,⁸¹ for example, studied in details this reaction in presence of gold and platinum nanoparticles and they did a complete set of experiments, varying the reducer, substrate and M-NPs individually, keeping the other reactants at constant concentration. They demonstrated that the reaction is dependent of the nanoparticles surface, and can be analyzed in terms of Langmuir-Hinshelwood mechanism, i.e. both reactants, Nip and NaBH₄, need to adsorb on the catalyst surface, as illustrated at Figure 9.

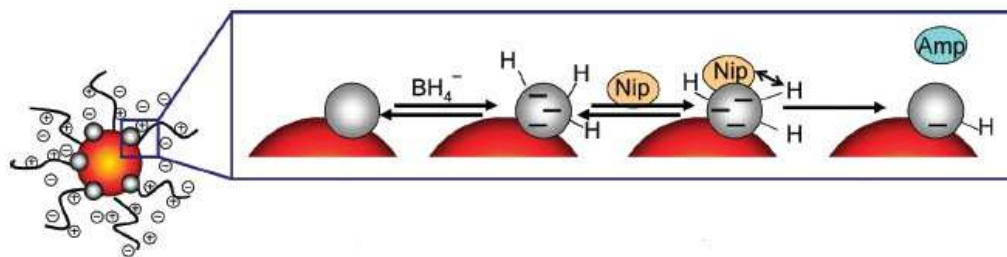


Figure 9. Mechanistic model (Langmuir-Hinshelwood mechanism) of the reduction of Nip by borohydride in the presence of metallic nanoparticles (gray spheres). The nanoparticles are bound to spherical polyelectrolyte brush (SPB) particles that consist of a polystyrene core and a shell of cationic polyelectrolyte chains. The catalytic reduction proceeds on the surface of the metal nanoparticles: The nanoparticles react with the borohydride ions to form the metal hydride. Concomitantly, nitrophenol adsorbs onto the metal surface. The adsorption/desorption of both reagents on the surface is fast and can be modelled in terms of a Langmuir isotherm. The rate-determining step is the reduction of the adsorbed Nip to Amp, which desorbs afterward.⁸¹

2.4.2 Silver nanoparticles (AgNPs)

Among the many different metals used in nanoparticles preparation, there is a great interest in transition metals, especially for their catalytic activity.⁸² The silver is one of the most studied in the literature, principally in the development of new preparation methodologies of nanoparticles and also due it is an important technological material.⁸² Silver shows unique properties normally attributed to noble metals (excellent conductivity, chemical stability and catalytic activity) and others characteristics that can be controlled by the nanoparticles' size, size distribution and their shape, with an acceptable production cost. Consequently, there is a great interesting in process advance to obtain AgNPs dispersions in large scale.⁸²

Silver has been known for antibacterial activity since the times of ancient Greece. Recently, AgNPs⁸³⁻⁸⁴ exhibiting antimicrobial activity have been synthesized and these silver-containing materials can be used, for example, in medicine to reduce infections in burn treatment⁸⁵ and arthroplasty,⁸⁶ as well as to prevent bacteria colonization on prostheses,⁸⁷ catheters,⁸⁸⁻⁸⁹ stainless steel materials,⁹⁰ and human skin.⁹¹ Silver-containing materials can be employed to eliminate microorganisms on textile fabrics,⁹² or they can be used for water treatment.⁹³ AgNPs also exhibit a potent cytoprotective activity toward HIV infected cells.⁹⁴

AgNPs are mainly used in oxidation/dehydrogenation reactions. Silver catalyzed epoxidation reaction is well known and widely applied in ethylene oxide production. Soluble

AgNPs in ethanol/water mixture are superior catalysts relative to a conventional heterogeneous Ag catalyst (Figure 10).⁹⁵⁻⁹⁶ It is also interesting to note that silver has been studied as a potential substitute for platinum as cathode in oxygen reduction reaction in alkaline medium, because of its reasonably high activity and low cost.⁹⁷ Moreover, silver cathodes have been reported as being more stable than platinum cathodes in long-term.⁹⁸

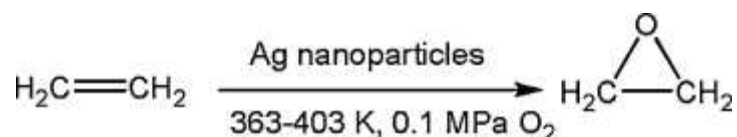


Figure 10. Epoxidation reaction of ethylene catalyzed by silver nanoparticles.⁹⁵⁻⁹⁶

2.4.3 Solvent effects

In chemistry, solvent effects are the group of effects that a solvent has on chemical reactivity. Solvents can have effect on solubility, stability and reaction rates, and the choice of the appropriate solvent allows the thermodynamic and kinetic control over a chemical reaction.⁹⁹

The first observation to show that an inert solvent could affect the rate of an organic reaction was made 150 years ago.¹⁰⁰ From that time there have been a number of attempts to understand the role of the solvent with methods including multiple linear regression analysis, factor analysis and principal component analysis all being used in an attempt to develop some level of understanding and predictability of these effects. Such analysis tends to rely on various free energy relationships, and despite the complicated nature of solvents and solutions, they have shown that they can provide some insight into many chemical processes.

As for many homogeneous catalysed reactions, many heterogeneous catalysed processes are carried out in a solvent for the simple purpose of dissolving the reactants and keeping the products in solution. Here too, solvents are known to influence both rate and selectivity, although in such systems the multi-phase nature of these reactions increases their complexity. Therefore, in addition to factors such as solvent polarity, dielectric constant and acid/base properties of the reaction medium, factors such as the solvation of reactants and products, gas solubility and other mass transfer effects need to be considered as these can all significantly influence reaction rates and product selectivity.¹⁰¹

Many works have been dedicated to understand the solvents effects to control the reactivity and selectivity of reactions, but only a few works are dedicated to M-NPs catalyzed reactions. Mukherjee and Vannice,¹⁰² for example, reported solvent effects during the liquid-phase

hydrogenation of citral using Pt/SiO₂ and eight nonreactive solvents. They observed that the rates were affected by the choice of solvent; however, differences in the product distribution were not significant. In this case, it was found that the variation in specific activity did not correlate with either the solvent dielectric constant or the dipole moment. Similarly, Gómez-Quero *et al.*¹⁰³ studied solvent effects during the liquid-phase hydrodehalogenation of haloarenes in methanol, THF, water/methanol and water/THF mixtures using a Pd/Al₂O₃ catalyst. Within this work they noted that higher initial rates were observed with increasing water content in the solvent mixture and attributed this to an increase in the dielectric constant of the medium. Such observations were consistent with an electrophilic mechanism in which the solvent helped to stabilise the arenium intermediate. An overall dependence of rate on solvent for this reaction could then be established with approximately 80% of the contribution being due to the dielectric constant with molar volume being a secondary factor. Mixed alcohol/water solvents have also been investigated. For example, a minimum in the rate of 2-butene-1,4-diol hydrogenation (the second step in the hydrogenation of 2-butyne-1,4-diol over Pd/Al₂O₃) occurred at 80–90 mol_{H₂O}% in a 2-propanol/water solvent.¹⁰⁴ Elsewhere, an enhancement in the rate of reaction in mixed alcohol/water solvents, compared to the pure alcohol, has been observed in the 2-butanone hydrogenation over Ru-SiO₂ catalysts,¹⁰⁵ acetophenone hydrogenation over Raney-Ni catalyst,¹⁰⁶ and *o*-nitrotoluene hydrogenation over Pd/C.¹⁰⁷ In the latter example, an increase of almost 50% in the reaction rate was reported upon changing solvent from pure methanol to a mixed methanol/water solvent containing 18% of water.

2.5 Biosensors for lectins recognition

Biosensors are small dispositives that use biological reactions or interactions to detect a specific analyte. Such dispositives combine a biological component, which interacts with the target substrate, to a physical transducer, that translates the biorecognition event into a useful measurable signal.¹⁰⁸

In the era of nanotechnology, noble M-NPs have played an important role in the development of new biosensors and/or in the enhancement of existing biosensing techniques to fulfil the demand for more specific and highly sensitive biomolecular diagnostics. The unique physicochemical properties of such metals at the nanoscale have led to the development of a wide variety of biosensors, such as: (i) nanobiosensors for point of care disease diagnosis, (ii) nanoprobe for in vivo sensing/imaging, cell tracking and monitoring disease pathogenesis or therapy monitoring and (iii) other nanotechnology-based tools that benefit scientific research on fundamental biology.¹⁰⁹

Lectins (Figure 11) represent a structurally heterogeneous group of multivalent proteins which bind specifically and recognize mono/oligosaccharides with high selectivity, even when these sugars are bound to proteins, lipids and functionalized amphiphiles.¹¹⁰⁻¹¹¹ Lectins attracted great interest because they bind specifically and reversibly to mono and oligosaccharides and act as mediators of cellular recognition in a variety of systems.¹¹² Lectins generally exist in multimeric forms and present the ability to interact simultaneously with multiple carbohydrate ligands i.e. in a multivalent way. Therefore, when they react with cells, for example erythrocytes, they will not only combine with the sugars on their surfaces, but will also cause cross-linking of the cells and their subsequent precipitation, a phenomenon referred to as cell agglutination. The erythrocyte agglutinating, or hemagglutinating, activity of lectins is a major attribute of these proteins and is used routinely for their detection and characterization. Lectins also form cross-links between oligosaccharide or glycoprotein molecules in solution and induce their precipitation. Both the agglutination and precipitation reactions of lectins are inhibited by the sugar ligands for which the lectins are specific.¹¹³

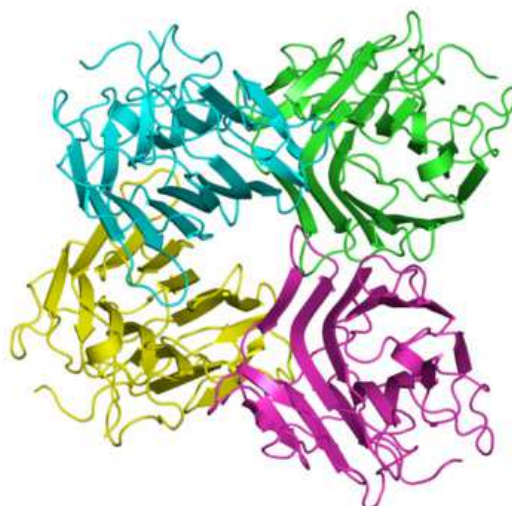


Figure 11. 3D structure of lectin Concanavalin A.¹¹⁴

As various lectins and glycoconjugates such as glycoproteins and glycolipids are found on the cell surface, the lectin–glycoconjugate interaction is associated with various life events including cell–cell interactions, pathogen (virus) infection and tumor metastasis.^{113, 115} Therefore, the selective detection of lectins and glycoconjugates is important to disclose the complex biological processes mediated by lectins.¹¹⁶

Metal nanoparticles conjugated with mono/oligosaccharide derivatives have been reported as attractive tool for lectins detection. For example, Wang and *et al.*¹¹⁷ developed a fluorescence-based competition assay to determine the apparent dissociation constants of gold-based glyconanoparticles (Au-GNPs) with the lectin Concanavalin A (Con A), and this assay was used to

determine the dissociation constants (K_D) values and to evaluate the binding affinity of Au-GNPs. They performed systematic studies in nanoparticles size, spacer length, ligand size and density to understand how these factors influence on the Au-GNPs binding affinity and the results demonstrated that the lectin binding to ligands on Au-GNPs is profoundly affected by how the ligands are displayed on the nanoparticle's surface. Min *et al.*²¹ reported a highly selective method for lectins determination based in electrochemical measures using carbohydrate-stabilized gold nanoparticles and silver-enhancement technique. These lectin biosensor gave a linear response ($R^2 = 0.999$) for Con A concentration from $0.084 \mu\text{g mL}^{-1}$ to $50.0 \mu\text{g mL}^{-1}$ with a remarkable detection limit of $0.070 \mu\text{g/mL}$, which is much lower compared to those obtained with the reported microgravimetric and colorimetric detection methods. Schofield *et al.*¹¹⁸ prepared gold and silver glyconanoparticles and showed that both metals can be used to develop aggregation-based colorimetric bioassays. The silver system demonstrated a better linear dynamic range and faster reaction kinetics for the target lectin, but the gold system provides a most sensitive bioassay.

3 Objective

The main objective of this work is the development of silver nanoparticles stabilized by dextran, a natural polysaccharide, and amphiphile compounds prepared from oligosaccharides (maltose, maltoheptaose, lactose and xyloglucan), and the study of these systems as catalysts in the *p*-nitrophenol reduction reaction and as lectins sensors. In this way, the following goals were established:

- Preparation and characterization of AgNPs stabilized by dextran, using multivariate analysis to determine the best condition for their preparation.
- Catalytic activity determination in the *p*-nitrophenol reduction to *p*-aminophenol.
- Synthesis and characterization of different oligosaccharide-based amphiphiles.
- Preparation and characterization of AgNPs stabilized by the different amphiphile compounds, previously synthesized, using multivariate analysis and their catalytic activity in the *p*-nitrophenol reduction to *p*-aminophenol.
- Study the water/ethanol mixtures effect in the *p*-nitrophenol reduction to *p*-aminophenol.
- Use the AgNPs stabilized by the amphiphile compounds as sensors for lectin proteins.

4 Experimental section

In this section are described materials, techniques, compounds synthesis and other methodologies employed in this work, developed in collaboration between the Laboratório de Catálise Biomimética (Florianópolis/ Universidade Federal de Santa Catarina) and the Centre de Recherches sur les Macromolécules Végétales (Grenoble/ CNRS - Université de Grenoble).

4.1 Reactants and solvents

Sodium borohydride (Sigma-Aldrich, 98%), silver nitrate (Cennabras, 98%), *p*-nitrophenol (Riedel, 99%) dextran T500 (Pharmacia), propargylamine (Sigma-Aldrich, 98%), L-(+)-ascorbic acid sodium salt (Fluka, 98%), copper (II) sulphate pentahydrate (Fluka, 98%), sodium azide (Alfa Cesar, 99%), 12-bromo-dodecanoic acid (Sigma-Aldrich, 99%), ethyl 6-bromo-hexanoate (Sigma-Aldrich, 99%), β -cyclodextrin (Sigma-Aldrich, 97%) *Arachis hypogaea* (peanut) lectin (PNA) (EY Laboratories, Inc.), *Canavalia ensiformis* (Jack bean) Concanavalin A (Con A) (Sigma) and tamarind seed xyloglucan (XG, purity 95.0%) from Dainippon Pharmaceutical Co., Ltd. (Osaka, Japan) were used as received without any further purification. Maltoheptaose was prepared according to the literature.¹¹⁹

Ultrapure water (resistivity of 18.2 m Ω cm), degassed by ultrasonic treatment, was used in all experiments. All glassware was washed with concentrated nitric acid and rinsed copiously with deionised water prior use.

4.2 Materials, equipments and techniques

The ^1H and ^{13}C nuclear magnetic resonance (NMR) were obtained with a 400 MHz Bruker Avance DRX400 spectrometer (400 and 100 MHz, respectively), using appropriate deuterated solvents for each case. The chemical shifts are expressed in parts per million (ppm) relative to tetramethylsilane (TMS) at 0.00 ppm and the coupling constants (J) given in Hertz (Hz).

Electrospray mass spectrometry analysis were recorded in positive mode on a ZabSpec TOF (Micromass, UK) with 3500 V of capilar voltage and cone voltage of 60 V. The MALDI-TOF were done on a Bruker Daltonics Autoflex apparatus, in positive mode, 2,5-DHB matrix, reflector mode, voltage acceleration of 24000 and 256 laser irradiations. High-resolution mass spectrometry measurements were performed on a Micromass ZABSpec-ToF spectrometer at the Centre Regional de Mesures Physiques de l'Ouest CRMPO (Rennes, France).

Transmission electron microscopy (TEM) images were recorded on a Kodak SO163 film using a CM200 Philips microscope operating at 18kV. A typical method for preparing TEM samples is as follows: one drop of reaction mixture was deposited on a 200-mesh Formvar/carbon coated copper grid, and excess solution was removed by wicking with filter paper to avoid particle aggregation. The particle size analysis was conducted by analyzing at least 150 particles and was determined from the particles' diameter.

Dynamic light scattering (DLS) measurements were performed using an ALV laser goniometer, which consists of 22mW HeNe linear polarized laser operating at a wavelength of 632.8 nm, an ALV-5004 multiple τ digital correlator with 125 ns initial sampling time, and a temperature controller. The measurements were made at 90°. The aqueous solutions of AgNPs were filtered directly into the glass cells through 0.22 μ m MILLIPORE Millex PES hydrophilic. Data were collected using digital ALV Correlator Control software. By the autocorrelation function, with CONTIN analysis, the relaxation times distributions were determined. Diffusion coefficients D were calculated from the Equation 2:

$$\text{Equation 2. } \lim_{q \rightarrow 0} \frac{\Gamma}{q^2} = D$$

where Γ is relaxation frequency ($\Gamma = \tau^{-1}$) q is the wave vector defined as follow:

$$\text{Equation 3. } q = \frac{4n\pi}{\lambda} \sin\left(\frac{\theta}{2}\right)$$

and λ is the wavelength of the incident laser beam, θ is the scattering angle and n is the refractive index of the media. The hydrodynamic radius (R_h) was calculated from the Stokes-Einstein relation:

$$\text{Equation 4. } R_h = \frac{k_B T}{6\pi\eta\Gamma} q^2 = \frac{k_B T}{6\pi\eta D}$$

The hydrodynamics diameters were calculated multiply R_h by 2.

The zeta potentials (ζ) measurements were performed in a Malvern Zetasizer ZS (Malvern Instruments, UK) with He-Ne laser at wavelength 633 nm, detection angle at 173° and 25.0 °C. The nanoparticles' medium zeta potential was determined by measuring their electrophoretic mobility (U_E) and values were converted a zeta potential (mV) by Henry equation (Equation 5):

Equation 5.
$$\zeta = \frac{3\eta U_E}{2\varepsilon f(ka)}$$

where ε is the dielectric constant, $f(ka)$ is the Henry function, which was calculated to be as 1.5 using the Smoluchowski approximation.

Small angle X-ray scattering (SAXS) experiments were performed on the BM02 beamline of the European Synchrotron Radiation Facility (Grenoble, France) and on the D11A-SAXS beamline of the Brazilian Synchrotron Light Laboratory (LNLS – Campinas, SP, Brazil). On the BM02 beamline, the AgNPs samples were put into glass capillaries of 5.0 mm diameter. The samples were disposed in sample holders equipped with an integrated heating system keep at 25.0 °C. The experiments were performed using 18 keV ($\lambda = 0.089$ nm) X-rays. Scattering intensities were recorded during 200 s exposures on a CCD detector placed about 78 cm behind the sample. These data were all collect at ambient pressure. The azimuthal integration was done with the Bm2img software developed on BM02, see reference ¹²⁰ for more details. On the D11A-SAXS beamline, the samples were loaded in a temperature controlled vacuum flow-through cell composed of two mica windows separated by 1 mm, normal to the beam. ¹²¹ The collimated beam crossed the samples through an evacuated flight tube and was scattered to a 2D CCD marCCD detector with active area of 16 cm². The 2D scattering patterns were collected after an exposure time of 600 s and the sample-to-detector distance was set to 150 cm. The 2D pictures were corrected for dark current, distortions of detector and normalized to the transmission and beam's intensity. Furthermore, the resulting $I(q)$ vs. q scattering curves were corrected by the subtraction of the scattering of the pure solvent and the $I(q)$ vs. q scattering profile of the Ag-NP could be fitted by using the form factor of homogeneous spheres. The fitting procedures were done by using the SASfit software which makes use the least-squares fitting approach for minimizing the squared chi (χ^2) parameter. The SASfit software package was developed by J. Kohlbrecher and it is available free of charge. ¹²²

4.3 Multivariate analysis optimization in the preparation of silver nanoparticles stabilized by dextran (AgNPs-dextran)

The optimization step of the variables (i.e. concentrations of dextran, silver nitrate and sodium borohydride) in the formation of AgNPs was carried out using a two-level full factorial design. This design involved fourteen basic experiments plus four central points. The values,

corresponding to the high (+), low (–) and central (0) points for each factor, are shown in Table 1 and the experimental designs in Table 2. The evaluation of the results of the factorial design was carried out using analysis of variance at the 95% confidence level. These experiments were carried out in transparent 96-well plates (NUNC) and acquiring in situ the UV-Vis spectra at 300 to 800 nm with a microtiter plate reader (Molecular Devices Spectramax Plus 384). Typically, to 180.0 μL of an aqueous dextran solution, 10.0 μL of AgNO_3 were added and the solution incubated for 10 min before the addition of the reducing agent (10.0 μL of NaBH_4), to give a total volume of 200 μL . The final concentrations of dextran, AgNO_3 and NaBH_4 for each multivariate experiment are shown in Table 2. All of the experiments were carried out at least in duplicate. Experimental data was processed using the Statistica 8.0 computer program.

Table 1. Factor levels in the AgNPs-dextran experimental design.

Level	[Dextran] 10^3 mol L^{-1}	[AgNO_3] 10^3 mol L^{-1}	[NaBH_4] 10^3 mol L^{-1}
-2	1.0	0.08	1.4
-1	75.8	0.18	2.3
0	150.5	0.29	3.2
+1	225.2	0.39	4.1
+2	300.0	0.5	5.0

Table 2. Multivariate experiments combinations for AgNPs-dextran optimization concentrations in each optimization experiment.

Experiment	Dextran	AgNO ₃	NaBH ₄	[Dextran] 10 ³ mol L ⁻¹	[AgNO ₃] 10 ³ mol L ⁻¹	[NaBH ₄] 10 ³ mol L ⁻¹
1	-1	-1	-1	75.8	0.18	2.3
2	-1	-1	+1	75.8	0.18	4.1
3	-1	+1	-1	75.8	0.39	2.3
4	-1	+1	+1	75.8	0.39	4.1
5	+1	-1	-1	225.2	0.18	2.3
6	+1	-1	+1	225.2	0.18	4.1
7	+1	+1	-1	225.2	0.39	2.3
8	+1	+1	+1	225.2	0.39	4.1
9	-2	0	0	1.0	0.29	3.2
10	+2	0	0	300.0	0.29	3.2
11	0	-2	0	150.5	0.08	3.2
12	0	+2	0	150.5	0.50	3.2
13	0	0	-2	150.5	0.29	1.4
14	0	0	+2	150.5	0.29	5.0
15	0	0	0	150.5	0.29	3.2
16	0	0	0	150.5	0.29	3.2
17	0	0	0	150.5	0.29	3.2
18	0	0	0	150.5	0.29	3.2

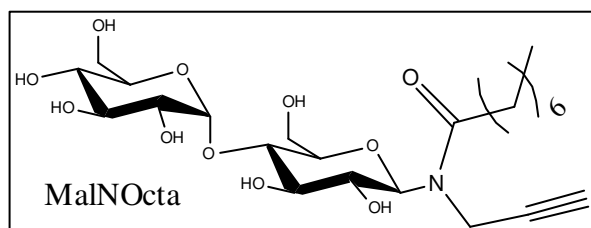
4.4 AgNPS-dextran catalytic activity

The catalytic activities of Ag-NPs-dextran composites were evaluated in the reduction reaction of *p*-nitrophenol (Nip) to *p*-aminophenol (Amp) in 96-well plates (Nunc) with a final volume of 200 μ L at 25°C. Firstly, the reducing agent concentration (NaBH₄) was varied from 8.8×10^{-3} to 0.264 mol L^{-1} , while keeping the Nip and Ag-NPs (based on amount of silver atoms) concentrations at $8.8 \times 10^{-5} \text{ mol L}^{-1}$ and $2.5 \times 10^{-6} \text{ mol L}^{-1}$, respectively. Secondly, the catalyst concentration (Ag-NPs) was varied from 2.5×10^{-6} to $20 \times 10^{-6} \text{ mol L}^{-1}$ keeping the Nip and NaBH₄ concentrations at $8.8 \times 10^{-5} \text{ mol L}^{-1}$ and 0.176 mol L^{-1} , respectively. Reactions were started with the addition of Nip and the kinetics monitored through the decrease in absorbance at 400 nm on a microtiter plate reader (Molecular Devices Spectramax Plus 384). All experimental procedures were

carried out in triplicate and reproducibly gave catalysts with kinetic properties within 15% of the values described.

4.5 Oligosaccharide based amphiphiles synthesis

Synthesis of N-maltosyl-3-octanamide-1-propyne (MalNOcta)

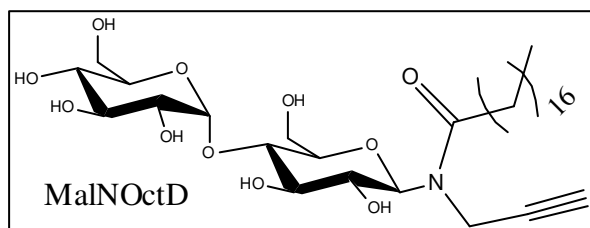


For the *N*-maltosyl-3-octanamide-1-propyne synthesis, firstly octanoic anhydride was prepared. To a solution of octanoic acid (4.528 g, 32.0 mmol) in dry dichloromethane (90 mL) was added *N,N'*-

dicyclohexylcarbodiimide (DCC) (3.6 g, 16.0 mmol) and the reaction mixture was stirred for 2 hours at room temperature. The formed dicyclohexylurea (DCU) was filtered and the octanoic anhydride was concentrated under reduced pressure. No further purification was performed.

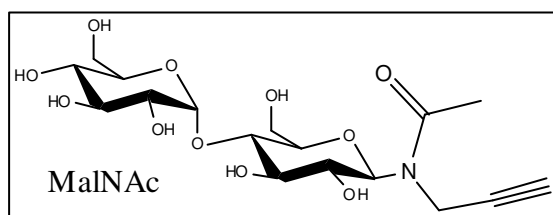
Then suspension of maltose (1.5 g, 4.38 mmol) in neat propargylamine (6.2 mL, 90.8 mmol) was stirred vigorously at room temperature for 72 hours. Upon complete conversion of starting material, checked by t.l.c. ($\text{CH}_3\text{CN}/\text{H}_2\text{O}$ - 8:2), excess of propargylamine was removed under reduced pressure, at a temperature below 40.0 °C and then co-evaporated using a mixture of toluene and methanol (9:1, v/v). The residual yellow solid was dissolved in methanol and precipitated with dichloromethane. The solid was filtered and washed with a mixture of methanol and dichloromethane (1:4, v/v). The solid was dissolved in methanol (180 mL) and octanoic anhydride (5.921 g, 21.9 mmol) was added. After 24 hours sodium methoxide was added to reaction (until pH~9) to hydrolyze random ester formed as side product. The reaction was neutralized with IR120 resin and evaporated under reduced pressure in the presence of silica, and crude solid was purified by flash chromatography (eluent $\text{CH}_3\text{CN}/\text{H}_2\text{O}$ 9:1). *N*-maltosyl-3-octanamide-1-propyne was isolated as a pure white solid (1.35 g, 61%) after lyophilization.

^1H NMR (MeOH, 298 K) δ 5.55 and 4.95 (d, 1H, rotamers, $J = 9.0$ Hz, and $J = 8.0$ Hz, H-1^{GlcI}), 5.20 (d, 1H, $J = 3.5$ Hz, $\text{H-1}^{\text{GlcII}}$), 4.28 – 4.10 (m, 2H, NCH_2), 3.89 – 3.44 (m, 12H, $\text{H-2,3,4,5,6a,6b}^{\text{GlcI and GlcII}}$), 3.28 and 3.25 (2x s, rotamers, $\text{C}\equiv\text{CH}$), 2.60 – 2.49 (m, 2H), 1.64 (d, $J = 6.0$ Hz, 2H), 1.33 (d, 8H), 0.91 (t, 3H, CH_3). ^{13}C NMR (MeOH, 298 K) δ 176.26, 102.88, 87.57, 83.39, 80.62, 78.81, 75.06, 74.81, 74.16, 71.80, 71.50, 62.74, 62.22, 34.38, 32.92, 30.66, 30.25, 26.21, 23.69, 14.42 HRMS (ESI) calculated for $\text{C}_{23}\text{H}_{39}\text{NO}_{11}\text{Na}$ $[\text{M}+\text{Na}]^+$: 528.24153; found 528.2415.

Synthesis of N-maltosyl-3-octadecylamide-1-propyne (MalNOctD)

A suspension of maltose (1.0 g, 2.63 mmol) in neat propargylamine (4 mL, 58.6 mmol) was stirred vigorously at room temperature for 72 hours. Upon complete conversion of starting material, checked by t.l.c. ($\text{CH}_3\text{CN}/\text{H}_2\text{O}$ - 8:2), excess of propargylamine was removed under reduced pressure, at a temperature below 40.0 °C and then co-evaporated using a mixture of toluene and methanol (9:1, v/v). The residual yellow solid was dissolved in methanol and precipitated with dichloromethane. The solid was filtered and washed with a mixture of methanol and dichloromethane (1:4, v/v). The solid was dissolved in DMF and lutidine (0.920 mL, 8.0 mmol). Stearoyl chloride (1.6 mL, 7.3 mmol) was slowly added to reaction mixture at 0.0 °C and then stirred at room for 2 hours. The DMF was evaporated and crude solid was redispersed in methanol and sodium methoxide was added to mixture (until pH~9) to deacilated random ester formed as side product. The reaction was neutralized with IR120 resin and evaporated under reduced pressure in the presence of silica, and crude solid purified by flash chromatography (eluent $\text{CH}_2\text{Cl}_2/\text{CH}_3\text{OH}$ - 9:1 and 85-15). *N*-maltosyl-3-octadecylamide-1-propyne was isolated as a pure white solid (0.697 g, 37%) after lyophilization.

^1H NMR (DMSO - $d_6/\text{D}_2\text{O}$, 298 K) δ 5.35 and 4.82 (2x d, 1H, rotamers, $J = 9.1$ and $J = 8.7$ Hz, H-1 GlcI), 5.02 (d, $J = 3.6$ Hz, H-1 GlcII), 4.11 - 3.95 (m, 2H, NCH_2), 3.71 - 3.05 (m, 12H, H-2,3,4,5,6a,6b GlcI and GlcII), 2.87 (s, 1H, $\text{C}\equiv\text{CH}$), 2.40 - 2.36 (t, 2H, CH_2CO), 1.48 (m, 2H, CH_2), 1.23 (m, 28H, CH_2), 0.83 (t, 3H, CH_3). ^{13}C NMR (DMSO, 298 K) δ 173.96, 101.59, 86.32, 82.19, 80.08, 78.77, 77.93, 74.22, 73.90, 73.10, 72.92, 70.52, 61.48, 33.39, 32.11, 29.81, 25.42, 22.92, 14.79. HRMS (ESI) calculated for $\text{C}_{33}\text{H}_{59}\text{NO}_{11}\text{Na}$ $[\text{M}+\text{Na}]^+$: 668.39803; found 668.3982.

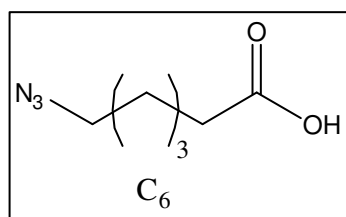
Synthesis of (N-maltosyl)-3-acetamido-1-propyne (MalNAc)

For MalNAcC_6 and MalNAcC_{12} synthesis, the MalNAc was firstly prepared. A suspension of maltose (1.0 g, 2.63 mmol) in neat propargylamine (4 mL, 58.6 mmol) was stirred vigorously at room temperature for 72 hours. Upon complete conversion of starting material, checked by t.l.c. ($\text{CH}_3\text{CN}/\text{H}_2\text{O}$ - 8:2), excess of propargylamine was removed under reduced pressure, at a temperature below 40.0 °C and then co-evaporated using a mixture of toluene and methanol (9:1, v/v). The residual yellow solid was dissolved in methanol and precipitated with dichloromethane. The solid was filtered and

washed with a mixture of methanol and dichloromethane (1:4, v/v). The solid was dissolved in methanol (85 mL) and acetic anhydride (17 mL) was added. The reaction mixture was stirred for 16 hours at room temperature, then the solvent was evaporated and traces of acetic anhydride were removed by co-evaporation with a mixture of toluene and methanol (1:1). *N*-maltosyl-3-acetamide-1-propyne was isolated as pure white solid (0.971 g, 83%) after lyophilization.

^1H NMR (D_2O , 298 K) δ 5.57 and 5.12 (2x d, 1H, rotamers, $J = 9.3$ and $J = 8.9$ Hz, H-1^{GlcI}), 5.47 (d, $J = 4.5$ Hz, H-1^{GlcII}), 4.35 – 4.14 (m, 2H, NCH_2), 3.94 – 3.43 (m, 12H, H- 2,3,4,5,6a,6b^{GlcI} and ^{GlcII}), 2.78 and 2.62 (2x s, rotamers, $\text{C}\equiv\text{CH}$), 2.35 and 2.28 (2x s, 3H, rotamers, CH_3 (Ac.)). ^{13}C NMR (D_2O , 298 K) δ 173.33, 172.16, 97.11, 97.06, 83.95, 79.19, 77.39, 74.70, 74.41, 74.05, 73.27, 70.88, 70.38, 69.21, 67.76, 67.26, 66.85, 58.10, 58.00, 30.40, 27.64, 19.19, 18.73. MS ESI: calculated for $\text{C}_{23}\text{H}_{39}\text{NO}_{11}\text{Na}$ $[\text{M}+\text{Na}]^+$: 444.3; found 444.1.

Synthesis of 6-azido-hexanoic acid (C_6)

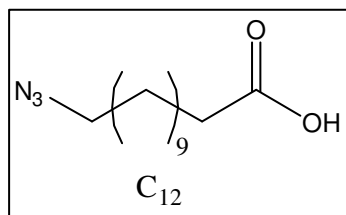


For hexanoic acid amphiphiles derivatives synthesis, the 6-azido-hexanoic acid (C_6) was prepared as follows: a mixture of ethyl 6-bromo-hexanoate (2.487 g, 11.2 mmol), sodium azide (1.456 g, 22.4 mmol) in DMF (20 mL) was stirred vigorously at 90.0 °C for 20 hours.

The reaction mixture was diluted in water and the product extracted from aqueous phase with diethyl ether (2x). The organic layer was dried on Na_2SO_4 and evaporated to dryness to give ethyl 6-azido-hexanoate as yellowish oil (1.842 g, 90%). ^1H NMR (CDCl_3 , 298 K) δ 4.09 (q, $J = 7.1$ Hz, 2H, OCH_2), 3.24 (t, $J = 6.9$ Hz, 2H, CH_2N_3), 2.28 (t, $J = 7.4$ Hz, 2H, CH_2COO), 1.67 – 1.56 (m, 4H, CH_2CH_2), 1.43 – 1.34 (m, 2H, CH_2), 1.22 (t, $J = 7.1$ Hz, 3H, CH_3). ^{13}C NMR (CDCl_3 , 298 K) δ 173.59, 60.41, 51.33, 34.21, 28.66, 26.33, 24.56, 14.35.

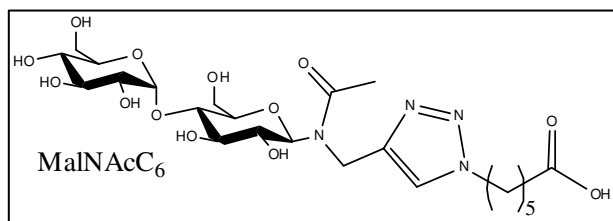
The 6-azido-hexanoic acid was obtained by hydrolysis of ethyl 6-azido-hexanoate (2.047 g, 11.2 mmol) in a suspension of $\text{Ba}(\text{OH})_2$ (1 g, 1 mol) in methanol stirred for 3 hours at room temperature, up to complete disappearance of the starting material, followed by t.l.c. (petroleum ether/ethyl ether - 9:1). The reaction mixture was acidified with HCl (2 mol L^{-1}) until $\text{pH} = 1$ and product extracted with CH_2Cl_2 (3x). The organic layer was dried on Na_2SO_4 and evaporated to dryness to give ethyl 6-azido-hexanoic acid as yellowish oil (1.443 g, 82% - global yield).

^1H NMR (CDCl_3 , 298 K) δ 10.48 (s, 1H, COOH), 3.25 (t, $J = 6.4$, 2H, CH_2N_3), 2.34 (t, $J = 7.4$, 2H, CH_2COOH), 1.68 – 1.54 (m, 4H, CH_2CH_2), 1.46 – 1.36 (m, 2H, CH_2). ^{13}C NMR (CDCl_3 , 298 K) δ 179.76, 51.27, 33.94, 28.62, 26.24, 24.25.

Synthesis of 12-azido-dodecanoic acid (C₁₂)

For dodecanoic acid amphiphiles derivatives synthesis, the 12-azido-dodecanoic acid (C₁₂) was prepared as follows: A mixture of 12-bromo-dodecanoic acid (2.491 g, 8.96 mmol) and sodium azide (1.165 g, 17.92 mmol) in DMF (15 mL) was stirred vigorously at 90.0 °C for 20 hours. The reaction mixture was diluted in water and the product extracted from aqueous phase with ethyl acetate (2x). The organic layer was dried on Na₂SO₄ and evaporated to dryness to give ethyl 12-azido-dodecanoic acid as yellowish oil (1.669 g, 93%).

¹H NMR (CDCl₃, 298 K) δ 3.23(t, *J* = 7.0 Hz, 2H, CH₂N₃), 2.32 (t, *J* = 7.5 Hz, 2H, CH₂COOH), 1.64 – 1.54 (m, 4H, CH₂CH₂), 1.34 – 1.26 (m, 14H, CH₂). ¹³C NMR (CDCl₃, 298 K) δ 179.82, 51.39, 34.04, 29.35, 29.13, 26.62, 24.62.

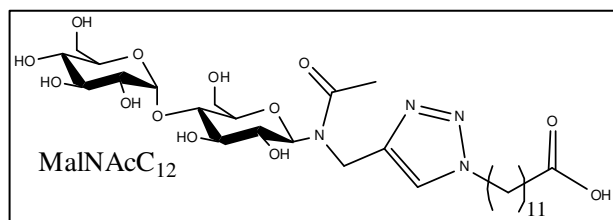
Synthesis of (((N-maltosyl)acetamido)methyl)-1H-1,2,3-triazol-1-yl)hexanoic acid (MalNAcC₆)

N-maltosyl-3-acetamido-1-propyne (0.500 g, 0.86 mmol) and 6-azido-hexanoic acid (0.200 g, 1.3 mmol) were dissolved in a mixture of isopropanol (7.5 mL) and water (6.5 mL) and heated to 40°C. Then CuSO₄·5H₂O (0.144 g, 0.86 mmol, 1mL of water) and sodium ascorbate (0.1238 g, 1.03 mmol) were added to reaction mixture and stirred for 3 hours, up to the complete disappearance of starting material, followed by t.l.c. (CH₃CN/H₂O - 9:3). The reaction was evaporated in the presence of silica under reduced pressure, and crude solid purified by flash chromatography (eluent CH₃CN/H₂O – 9:2). The residual copper salt was removed through adsorption of the product on active carbon, washing with water and desorption of the product with ethanol/water (1:1). The evaporation under reduced pressure followed by freeze-drying afforded (((*N*-maltosyl)acetamido)methyl)-1H-1,2,3-triazol-1-yl)hexanoic acid as white solid (0.5829 g, 85%).

¹H NMR (D₂O, 298 K) δ 8.04 and 7.95 (2x s, H-5^{triazole}), 5.62 and 5.16 (2x d, 1H, rotamers, *J* = 9.1 Hz and *J* = 8.8 Hz, H-1^{GlcI}), 5.44 (d, *J* = 3.6 Hz, H-1^{GlcII}), 4.67 - 3.41 (m, 16H, NCH₂ (2x), H-2,3,4,5,6a,6b^{GlcI and GlcII}), 2.37 – 2.33(t, 2H, CH₂COOH), 2.27 and 2.14 (2x s, 3H, rotamers, CH₃ (Ac.)), 1.94 - 1.89 (m, 2H, CH₂), 1.63 - 1.56 (m, 2H, CH₂), 1.30 - 1.23 (m, 2H, CH₂). ¹³C NMR (DMSO - d₆, 298 K) δ 175.29, 171.89, 145.90, 124.13, 101.66, 87.66, 82.52, 80.10, 78.09, 77.72, 77.30, 77.07, 74.27, 73.94, 73.13, 70.84, 61.51, 50.26, 36.79, 34.32, 30.20, 26.20, 24.71, 23.11,

22.61. MS ESI: calculated for $C_{23}H_{38}N_4O_{13}Na$ $[M+Na]^+$: 601.6; found 601.2. HRMS calculated for $C_{23}H_{37}N_4O_{13}$ $[M-H]^-$ = 577.23626; found 577.2364.

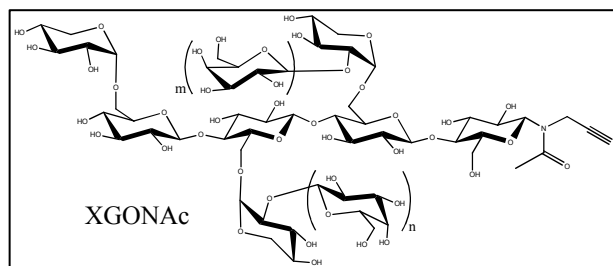
Synthesis of (((N-maltosyl)acetamido)methyl)-1H-1,2,3-triazol-1-yl)dodecanoic acid (MalNAcC₁₂)



N-maltosyl-3-acetamido-1-propyne (1.208 g, 1.8 mmol) and 12-azido-dodecanoic acid (1.034 g, 2.7 mmol) were dissolved in a mixture of isopropanol (90 mL) and water (85 mL) and heated to 40.0 °C. Then CuSO₄·5H₂O (0.6888 g, 1.8 mmol, 5 mL of water) and sodium ascorbate (0.594 g, 2.16 mmol) were added to reaction mixture and stirred for 20 hours, up to the complete disappearance of starting material, followed by t.l.c. (CH₃CN/H₂O - 8:2). The reaction was evaporated under reduced pressure, redispersed in water, filtered on cotton and purified in C18 reversed phase, followed by freeze-drying to afford (((*N*-maltosyl)acetamido)methyl)-1*H*-1,2,3-triazol-1-yl)dodecanoic acid as white solid (0.750 g, 40%).

¹H NMR (MeOH, 298 K) δ 8.00 and 7.85 (2x s, H-5^{triazole}), 5.58 and 4.92 (2x d, 1H, rotamers, *J* = 9.1 Hz and *J* = 8.8 Hz, H-1^{GlcI}), 5.13(d, *J* = 3.6 Hz, H-1^{GlcII}), 4.63 - 3.41 m, 16H, NCH₂ (2x), H-2,3,4,5,6a,6b^{GlcI and GlcII}), 2.29 - 2.09 (m, 5H, (2H, CH₂COOH and 3H, rotamers, CH₃ (Ac.)), 1.81 (m, 2H, CH₂), 1.53 (m, 2H, CH₂), 1.22(m, 14 H, CH₂). ¹³C NMR (DMSO - d₆, 353 K) δ 170.46, 144.81, 122.85, 100.36, 86.79, 78.88, 76.91, 76.30, 73.10, 73.07, 72.23, 69.97, 60.39, 49.05, 29.08, 28.35, 28.18, 28.12, 27.88, 25.44, 21.30. MS ESI: calculated for $C_{29}H_{50}N_4O_{13}Na$ $[M+Na]^+$: 685.7; found 685.3. HRMS calculated for $C_{29}H_{49}N_4O_{13}$ $[M-H]^-$ = 661.33016; found 661.3301.

Synthesis of (N-(xyloglucan oligosaccharide))-3-acetamido-1-propyne (XGONAc)

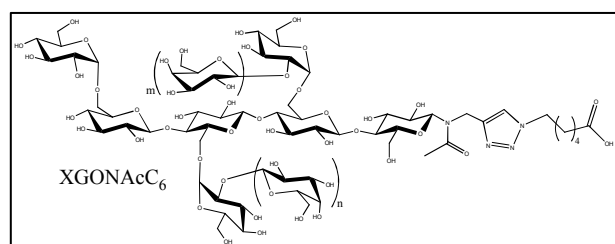


For the xyloglucan derivatives, firstly the (*N*-(XGO))-3-acetamido-1-propyne (XGONAc) was prepared. A suspension of XGOs (made up of a mixture of hepta-, octa-, and nona-saccharides in the ratio 0.15:0.35:0.50, respectively) (20 g, 12.1 mmol) in propargylamine (20 mL, 240.3 mmol) and 30 mL of methanol was stirred vigorously at room temperature for 3 days. Upon complete conversion of starting material, checked by t.l.c. (CH₃CN/H₂O - 7:3), excess of propargylamine was removed under reduced pressure, at a temperature below 40.0 °C and then co-evaporated using a mixture of

toluene and methanol (9:1, v/v). The residual yellow solid was dissolved in methanol and the precipitated with dichloromethane. The solid was filtered and washed with a mixture of methanol and dichloromethane (1:4, v/v). The solid was N-acetylated by adding a solution of acetic anhydride in methanol (1:20, v/v). The reaction mixture was stirred for 16 h at room temperature, then the solvent was evaporated, and coevaporated with a mixture of toluene and methanol (1:1, v/v) to remove traces of acetic anhydride. The residue was dissolved in water and freeze-dried to afford (*N*-(XGO))-3-acetamido-1-propyne as a pure white solid (20 g, 94%).

^1H NMR (D_2O , 298 K) δ 5.44 (d, $J_{1-2} = 8.61$ Hz, $\text{H}-1^{\text{GlcI}}$), 5.18 and 5.02 (d, $\text{H}-1^{\text{Xyl}}$), 4.90–4.60 (m, $\text{H}-1^{\text{Glc and Gal}}$), 4.50–3.20 (m, $\text{H}-2,3,4,5,6^{\text{Glc, Gal and Xyl}}$ and NCH_2), 2.68 and 2.51 (2x s, rotamers, $\text{C}\equiv\text{CH}$), 2.22 and 2.15 (2x s, rotamers, CH_3 (Ac.)). MS MALDI-TOF: m/z [$\text{M}+\text{Na}$] 1164.36 (hepta-), [$\text{M}+\text{Na}$] 1326.41 (octa-), [$\text{M}+\text{Na}$] 1488.46 (nona-saccharides).

Synthesis of (((N-(xyloglucan oligosaccharide))acetamido)methyl)-1H-1,2,3-triazol-1-yl)hexanoic acid (XGONAcC₆)

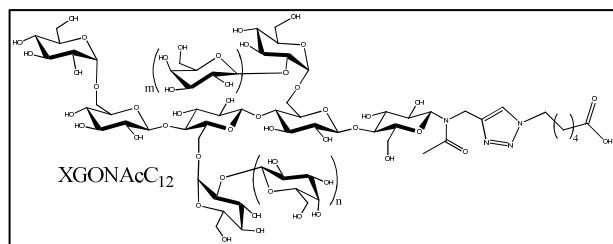


(*N*-(XGO))-3-acetamido-1-propyne (0.100 g, 0.075 mmol) and 6-azido-hexanoic acid (0.0181 g, 0.11 mmol) were dissolved in a mixture of isopropanol (1.5 mL) and water (0.5 mL) and heated to 40°C. Then $\text{CuSO}_4 \cdot 5\text{H}_2\text{O}$ (0.0191 g,

0.075 mmol, in 1 mL of water) and sodium ascorbate (0.0182g, 0.09 mmol) were added to reaction mixture and stirred for 24 hours. The reaction was evaporated under reduced pressure, redispersed in water, filtered on cotton and purified in C18 reversed phase, followed by freeze-drying to afford (((*N*-(XGO))acetamido)methyl)-1H-1,2,3-triazol-1-yl)hexanoic acid as white solid (0.091 g, 82%).

^1H NMR (D_2O , 298 K) δ 8.07 and 8.01 (2x s, $\text{H}-5^{\text{triazole}}$), 5.65 (d, 1H, $J = 5.63$ Hz $\text{H}-1^{\text{GlcI}}$), 5.22 - 5.19 (m, $\text{H}-1^{\text{Xyl}}$), 4.98 - 4.57 (m, $\text{H}-1^{\text{Glc and Gal}}$), 4.45 - 3.36 (m, $\text{H}-2,3,4,5,6^{\text{Glc, Gal, Xyl}}$ and 2x NCH_2), 2.29 - 2.16 (m, 5H, (2H, CH_2COOH and 3H, rotamers, CH_3 (Ac.)), 1.92 (m, 2H, CH_2), 1.60 (m, 2H, CH_2), 1.28 (m, 2H, CH_2). ^{13}C NMR ($\text{DMSO}-d_6$, 298 K) δ 172.35, 171.68, 145.98, 124.26, 106.58, 104.32, 99.56, 87.34, 82.51, 81.62, 77.43, 77.22, 76.13, 75.51, 75.28, 73.87, 73.50, 72.97, 72.37, 72.16, 71.86, 71.03, 70.89, 70.59, 69.05, 67.57, 62.75, 62.49, 61.32, 50.04, 31.55, 30.25, 26.34, 24.83, 22.72. MS MALDI-TOF: m/z [$\text{M}+\text{Na}$] 1321.45 (hepta-), [$\text{M}+\text{Na}$] 1483.51 (octa-), [$\text{M}+\text{Na}$] 1645.57 (nona-saccharides).

Synthesis of (((N-(Xyloglucan oligosaccharide))acetamido)methyl)-1H-1,2,3-triazol-1-yl)dodecanoic acid (XGONAcC₁₂)

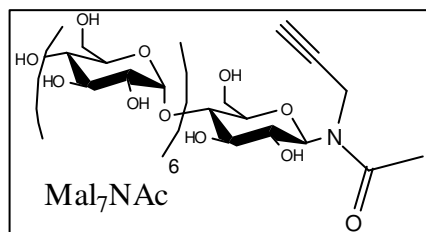


(*N*-(XGO))-3-acetamido-1-propyne (0.100 g, 0.075 mmol) and 12-azido-dodecanoic acid (0.0277 g, 0.11 mmol) were dissolved in a mixture of isopropanol (1.5 mL) and water (0.5 mL) and heated to 40.0 °C. Then CuSO₄·5H₂O (0.0191 g,

0.075 mmol, in 1 mL of water) and sodium ascorbate (0.0182 g, 0.09 mmol) were added to reaction mixture and stirred for 24 hours. The reaction was evaporated under reduced pressure, redispersed in water, filtered on cotton and purified in C18 reversed phase, followed by freeze-drying to afford (((*N*-(XGO))acetamido)methyl)-1H-1,2,3-triazol-1-yl)dodecanoic acid as white solid (0.095 g, 80%).

¹H NMR (D₂O, 298 K) δ 8.08 and 7.99 (2x s, H-5^{triazole}), 5.64 (d, H-1^{Glc}), 5.21 – 5.19 (m, H-1^{Xyl}), 4.99 - 4.41 (m, H-1^{Glc and Gal}), 4.10 - 3.34 (m, H-2,3,4,5,6^{Glc, Gal, Xyl} and 2x NCH₂), 2.33 - 2.17 (m, 5H, (2H, CH₂COOH and 3H, rotamers, CH₃ (Ac.)), 1.90 (m, 2H, CH₂), 1.59 (m, 2H, CH₂), 1.26 (m, 14H, CH₂). ¹³C NMR (DMSO - d₆, 298 K) δ 175.41, 172.59, 171.88, 145.95, 124.29, 106.41, 104.24 - 102.99, 99.98 - 99.31, 87.32, 82.43 - 80.63, 77.70, 76.96, 75.32, 73.87 - 72.00, 71.69, 70.86 - 70.38, 68.92, 67.48, 62.71 - 62.38, 61.33 - 61.00, 50.22, 34.44, 30.55 - 29.16, 26.69, 25.31, 22.68. MS MALDI-TOF: *m/z* [M+Na] 1475.45 (hepta-), [M+Na] 1567.45 (octa-), [M+Na] 1729.57 (nona-saccharides). HRMS calculated for C₆₂H₁₀₃N₄O₄₀ [M-H]⁻ = 1543.6154; found 1543.6163.

Synthesis of N-maltoheptaosyl-3-acetamido-1-propyne (Mal₇NAC)



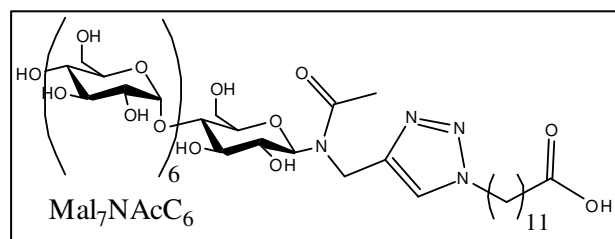
For the maltoheptaose derivatives, firstly the (*N*-(maltoheptaosyl))-3-acetamido-1-propyne (Mal₇NAC) was prepared. A suspension of maltoheptaose (10.0 g, 8.67 mmol) in neat propargylamine (11.9 mL, 174 mmol) was stirred vigorously at room temperature until complete conversion of the starting

material (72 h), checked by t.l.c. (eluent: BuOH/EtOH/H₂O = 1/3/1). After complete disappearance of the starting material, the reacting mixture was dissolved in methanol (100 mL) and then precipitated in CH₂Cl₂ (300 mL). The solid was filtrated and washed with a mixture of MeOH and CH₂Cl₂ (MeOH: CH₂Cl₂ = 1:3, v/v, 300 mL). The solid was added to solution of acetic anhydride in MeOH (acetic anhydride: MeOH = 1:20, v/v, 1 L) and stirred overnight at room temperature. After complete disappearance of the starting material checked by t.l.c. (eluent: CH₃CN/H₂O = 13/7), the

solvent of the mixture was evaporated, and the traces of acetic anhydride were removed by coevaporation with a mixture of toluene and methanol (1:1, v/v). The resulting solid was dissolved in water and freeze dried to afford N-Maltoheptaosyl-3-acetamido-1-propyne as white solid. (8.75 g, 78%).

^1H NMR (D_2O , 298 K): δ 5.46 and 5.00 (2 \times d, 1H, rotamers, $J_{1-2} = 9.20$ Hz and $J_{1-2} = 8.87$ Hz, $\text{H}-1^{\text{GlcI}}$), 5.36–5.31 (m, 6H, $\text{H}-1^{\text{GlcII-GlcVII}}$), 4.24–3.30 (m, 44H, H-2, 3, 4, 5, 6a, 6b $^{\text{GlcI-GlcVII}}$, and NCH_2), 2.66 and 2.50 (2 \times s, 1H, rotamers, $\text{C}\equiv\text{CH}$), 2.24 and 2.16 (2 \times s, 3H, rotamers, NCOCH_3). ^{13}C NMR (D_2O , 298 K): δ 176.22, 175.04, 100.09 – 99.76, 86.80, 82.03, 80.26, 79.64, 77.47, 77.20–76.85, 76.38, 76.23, 73.68, 73.23, 73.08, 72.10, 72.06, 71.90, 71.85, 71.54, 70.58, 70.08, 69.69, 60.84, 60.78, 33.19, 30.44, 21.98, 21.51. HRMS ESI-TOF (m/z) Calcd for $[\text{M} + \text{Na}]^+$: 1254.4123. Found: 1254.4122.

Synthesis of (((N-(maltoheptaosyl))acetamido)methyl)-1H-1,2,3-triazol-1-yl)hexanoic acid ($\text{Mal}_7\text{NacC}_6$)

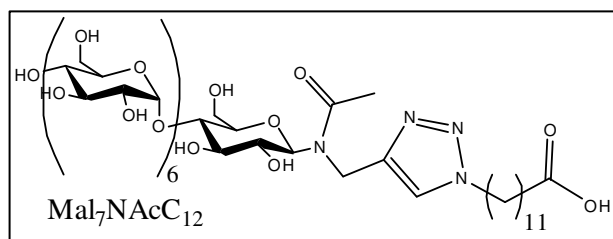


(N-(maltoheptaosyl))-3-acetamido-1-propyne (0.500 g, 0.4 mmol) and 6-azido-hexanoic acid (0.0956 g, 0.6 mmol) were dissolved in a mixture of isopropanol (7.5 mL) and water (6.5 mL) and heated to 40.0 °C. Then $\text{CuSO}_4 \cdot 5\text{H}_2\text{O}$ (0.1013 g,

0.4 mmol, 1mL of water) and sodium ascorbate (0.0965 g, 0.48 mmol) were added to reaction mixture and stirred for 24 hours. The reaction was evaporated under reduced pressure, redispersed in water, filtered on cotton and purified in C18 reversed phase, followed by freeze-drying to afford (((N-(maltoheptaosyl))acetamido)methyl)-1H-1,2,3-triazol-1-yl)hexanoic acid as white solid (0.528 g, 95%).

^1H NMR (D_2O , 298 K) δ 8.06 and 7.94 (2x s, $\text{H}-5^{\text{triazole}}$), 5.64 and 5.16 (2x d, 1H, rotamers, $J = 9.0$ Hz and $J = 8.9$ Hz, $\text{H}-1^{\text{GlcI}}$), 5.47 - 5.42 (m, 6H, $\text{H}-1^{\text{GlcII-GlcVII}}$), 4.47- 3.42 (m, 46H, NCH_2 (2x), H-2,3,4,5,6a,6b $^{\text{GlcI-GlcVII}}$), 2.34 - 2.17 (m, 5H, (2H, CH_2COOH and 3H, rotamers, CH_3 (Ac.)), 1.93 - 1.90 (m, 2H, CH_2), 1.60 - 1.57(m, 2H, CH_2), 1.32 - 1.23 (m, 2H, CH_2). ^{13}C NMR ($\text{DMSO}-d_6$, 298 K) δ 171.92, 145.75, 123.81, 101.16, 100.91, 79.93, 79.68, 77.28, 77.06, 73.75, 73.51, 72.78, 72.22, 72.08, 70.17, 61.17, 60.70, 49.74, 31.16, 29.83, 26.03, 25.47, 22.74, 22.28. MS MALDI-TOF: m/z $[\text{M}+\text{Na}]$ 1411.50. HRMS calculated for $\text{C}_{53}\text{H}_{87}\text{N}_4\text{O}_{38}$ $[\text{M}-\text{H}]^- = 1543.6154$; found 1543.6163.

Synthesis of (((N-(maltoheptaosyl))acetamido)methyl)-1H-1,2,3-triazol-1-yl)dodecanoic acid (Mal₇NacC₁₂)

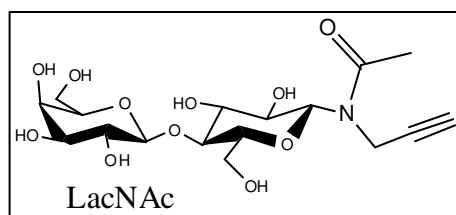


(*N*-(maltoheptaosyl))-3-acetamido-1-propyne (0.500 g, 0.4 mmol) and 12-azido-dodecanoic acid (0.1467 g, 0.6 mmol) were dissolved in a mixture of isopropanol (7.5 mL) and water (6.5 mL) and heated to 40.0 °C. Then CuSO₄·5H₂O (0.1013 g,

0.4 mmol, 1.0 mL of water) and sodium ascorbate (0.0965 g, 0.48 mmol) were added to reaction mixture and stirred for 24 hours. The reaction was evaporated under reduced pressure, redispersed in water, filtered on cotton and purified in C18 reversed phase, followed by freeze-dry to afford (((*N*-(maltoheptaosyl))acetamido)methyl)-1H-1,2,3-triazol-1-yl)dodecanoic acid as white solid (0.478 g, 80%).

¹H NMR (D₂O, 298 K) δ 8.06 and 7.94 (2x s, H-5^{triazole}), 5.64 and 5.16 (2x d, 1H, rotamers, *J* = 9.0 Hz and *J* = 8.9 Hz, H-1^{GlcI}), 5.47 - 5.42 (m, 6H, H-1^{GlcII-GlcVII}), 4.47- 3.42 (m, 46H, NCH₂ (2x), H-2,3,4,5,6a,6b^{GlcI-GlcVII}), 2.34 - 2.17 (m, 5H, (2H, CH₂COOH and 3H, rotamers, CH₃ (Ac.)), 1.93 - 1.90 (m, 2H, CH₂), 1.60 - 1.57(m, 2H, CH₂), 1.32 - 1.23 (m, 14H, CH₂). ¹³C NMR (DMSO - d₆, 298 K) δ 174.50, 170.86, 145.02, 123.26, 100.42, 86.86, 79.41, 73.31, 72.53, 72.04, 71.72, 69.92, 60.30, 49.35, 33.66, 29.67, 28.87, 28.55, 25.87, 24.49, 21.80. MS MALDI-TOF: *m/z* [M+Na] 1495.58. HRMS calculated for C₅₉H₉₉N₄O₃₈ [M-H]⁻ = 1471.59428; found 1471.5934.

Synthesis of N-Lactosyl-3-acetamido-1-propyne (LacNac)



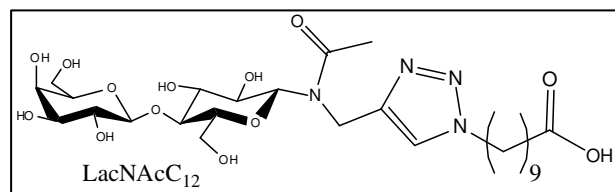
For the lactose derivative, firstly the *N*-lactosyl-3-acetamido-1-propyne (LacNac) was prepared. A solution of lactose (1.2 g, 3.3 mmol) in neat propargylamine (3.7 mL, 67 mmol) was stirred for 48 hours at room temperature. After

evaporation under reduced pressure, the residue was taken up in MeOH (24 mL) and acetic anhydride (3.8 mL, 40 mmol) was added. The solution was stirred overnight, concentrated and coevaporated three times with toluene. Purification by column chromatography (CH₃CN/H₂O, 9:1) followed by freeze-drying afforded LacNac as an amorphous solid (1.28 g, 91%).

¹H NMR (D₂O, 298 K) δ 5.58 and 5.12 (2x d, 1H, rotamers, *J* = 8.5 Hz and *J* = 8.6 Hz, H-1^{Glc}), 4.50 (d, 1H, *J* = 7.8 Hz, H-1^{Gal}), 4.35 - 3.55 (m, 14H, NCH₂, H-2,3,4,5,6a,6b^{Glc and Gal}) 2.78, 2.62 (2x s, rotamers, C≡CH), 2.35 and 2.27 (2x s, 3H, rotamers, CH₃ (Ac.)). ¹³C NMR (D₂O, 298 K) δ 173.36, 172.16, 100.41, 84.00, 79.25, 77.41, 76.79, 74.92, 74.46, 74.35, 72.98, 72.80, 72.51, 70.07,

69.26, 68.53, 67.62, 66.16, 58.70, 57.45, 30.44, 27.67, 19.22, 18.75. MS ESI: calculated for $C_{23}H_{39}NO_{11}Na$ $[M+Na]^+$: 444.3; found 444.1

Synthesis of (((N-(lactosyl))acetamido)methyl)-1H-1,2,3-triazol-1-yl)dodecanoic acid (LacNAcC₁₂)



N-lactosyl-3-acetamido-1-propyne (0.100 g, 0.24 mmol) and 12-azido-dodecanoic acid (0.0856 g, 0.36 mmol) were dissolved in a mixture of THF (7.5 mL) and water (6.5 mL) and heated to

40.0 °C. Then CuSO₄·5H₂O (0.0570 g, 0.24, in 1 mL of water) and sodium ascorbate (0.0492 g, 0.288 mmol) were added to reaction mixture and stirred for 2 hours, up to the complete disappearance of starting material, followed by t.l.c. (CH₃CN/H₂O - 8:2). The reaction was evaporated under reduced pressure, redispersed in water, filtered and purified in C18 reversed phase, followed by freeze-drying to afford (((*N*-lactosyl)acetamido)methyl)-1*H*-1,2,3-triazol-1-yl)dodecanoic acid as white solid (0.105 g, 64 %).

¹H NMR (MeOH, 298 K) δ 7.98 and 7.79 (2x s, H-5^{triazole}), 5.61 and 4.94 (2x d, 1H, rotamers, *J* = 8.5 Hz and *J* = 8.6 Hz, H-1^{Glc}), 4.65 - 4.27 (m, 5H, (1H, *J* = 7.8 Hz, H-1^{Gal}) and NCH₂ (2x)), 3.87 - 3.42 (m, 12H, , H- 2,3,4,5,6a,6b^{Glc and Gal}), 2.20 - 2.00 (m, 5H, (2H, CH₂COOH and 3H, rotamers, CH₃ (Ac.)) , 1.83 (m, 2H, CH₂), 1.53 (m, 2H, CH₂), 1.24 (m, 14 H, CH₂). ¹³C NMR (DMSO - d₆, 298 K) δ 177.81, 172.98, 145.22, 123.42, 103.79, 87.56, 78.62, 77.49, 75.87, 73.56, 71.25, 70.61, 69.05, 61.22, 60.56, 50.10, 36.17, 30.01, 29.30, 28.83, 26.23, 25.31, 20.73. MS ESI: calculated for C₂₉H₅₀N₄O₁₃Na $[M+Na]^+$: 685.7; found 685.3. HRMS calculated for C₂₉H₄₉N₄O₁₃ $[M-H]^-$ = 661.33016; found 661.3301.

4.6 Multivariate analysis optimization in the preparation of silver nanoparticles stabilized by amphiphiles compounds synthesized (AgNPs-amphiphiles)

The optimization step of the variables (*i.e.* concentrations of stabilizer and sodium borohydride) in the formation of silver nanoparticles was carried out using a two-level full factorial design with axial points. This design involved eight basic experiments plus four central points. The values, corresponding to the high (+1), low (−1), central (0) and axial points for each factor, are shown in Table 3 and the experimental designs in Table 4. The silver nitrate concentration was kept constant in all experiments (0.35 × 10^{−3} mol L^{−1}), this was decided after some previous experiments that demonstrated instrumental limitations in the absorbance at λ_{max} observation. The evaluation of

the results of the factorial design was carried out using analysis of variance at the 95% confidence level.

Table 3. Factor levels in the experimental design.

Factor	-2	-1	0	1	2
[NaBH ₄] 10 ³ mol L ⁻¹	0.50	2.88	5.25	7.62	10.0
[MalNOcta] mg mL ⁻¹	0.051	12.66	25.28	37.89	50.50
[MalNOctD] mg mL ⁻¹	0.016	0.036	0.056	0.078	0.097
[MalNAcC ₆] mg mL ⁻¹	0.58	15.32	14.74	21.83	28.91
[MalNAcC ₁₂] mg mL ⁻¹	1.70	3.98	6.25	8.52	10.80
[XGONAcC ₆] mg mL ⁻¹	0.01	1.26	2.50	3.75	5.00
[XGONAcC ₁₂] mg mL ⁻¹	0.01	0.26	0.50	0.75	1.00
[Mal ₇ NAcC ₆] mg mL ⁻¹	1.0	3.25	5.50	7.75	10.00
[Mal ₇ NAcC ₁₂] mg mL ⁻¹	0.01	1.26	2.50	3.75	5.00

Table 4. Multivariate optimization experimental design.

Experiment	Stabilizer	NaBH ₄
1	-1	-1
2	-1	1
3	1	-1
4	1	1
5	-2	0
6	2	0
7	0	-2
8	0	2
9	0	0
10	0	0
11	0	0
12	0	0

4.7 AgNPs-amphiphiles catalytic activity

The catalytic activities of Ag-glyconanoparticles were evaluated in the reduction reaction of *p*-nitrophenol (Nip) to *p*-aminophenol (Amp) in quartz cell with optic length of 10 mm with a final volume of 2.0 mL at 25°C. Reactions were started with the addition of Nip and the kinetics monitored through the decrease in absorbance at 400 nm. All experimental procedures were carried out in triplicate and reproducibly gave catalysts with kinetic properties within 15% of the values described.

4.8 AgNPs-amphiphiles evaluation as lectins sensors

The experiments with lectins were all performed in phosphate saline buffer (0.01 mol L⁻¹ pH = 7.2) containing 0.150 mol L⁻¹ of NaCl, 0.1 x 10⁻³ mol L⁻¹ of CaCl₂ and MnCl₂ 0.1 x 10⁻³ mol L⁻¹). The solution's pH was checked after the AgNPs addition to assure the good conditions for the lectins solubilisation.

The first assays were realized in a cuvette (optical length of 10 mm) scale. In a typical set of experiments, 100 µL of Ag-Mal₇NAC₁₂ nanoparticles were added to 900 µL of buffer with different concentrations of Con A and the UV-vis spectra of Ag-Mal₇NAC₁₂ were registrated at different times.

After the time optimization to stabilize the lectin nanoparticles interaction, it was opted to carry out the follow experiments in microplate scale. For these experiments, it was carried out as follows: In a preparative 96-well 1mL polypropylene plate, 0 to 7 μL of a stock solution of Con A (1.2 mg mL^{-1} in buffer) and PNA (1.0 mg mL^{-1} in buffer) were placed in different wells and diluted to 1mL with buffer. Then in a UV-vis transparent microplate, 100 μL of Ag-Mal₇NAcC₁₂ or Ag-XGONAcC₁₂ or Ag-LacNAcC₁₂ were placed in eight wells. Then, with multichannel micropipette, 200 μL of the different lectins solutions were added to wells and the absorbance was read at 415 nm after 1 hour. These experiments were realized in triplicate.

5 Results and discussion

In this chapter are presented the results obtained in this work. This chapter is divided in two main sections, according with the type of stabilizer used (polysaccharide or oligosaccharide-based amphiphiles).

5.1 Silver nanoparticles stabilized by dextran polysaccharide

5.1.1 Silver nanoparticles preparation and characterization (AgNPs-dextran)

The dextran (Figure 12) is a branched aqueous soluble polysaccharide formed by glucose units linked by α -1,6 glycosidic bonds (main structure) and α -1,3 (ramifications). Dextran molar masses range from 1000 to 2000000 g mol⁻¹ (and normally dextrans have a low dispersity degree).¹²³ It was chosen as stabilizer because it is a water soluble and branched polysaccharide which forms in solution hydrophilic and hydrophobic domains that can stabilize the silver nanoparticles and attract some substrates near the AgNP. The AgNO₃ was chosen as metal precursor and NaBH₄ as reducing agent because a strong reducing agent leads to lower M-NPs sizes.³⁷

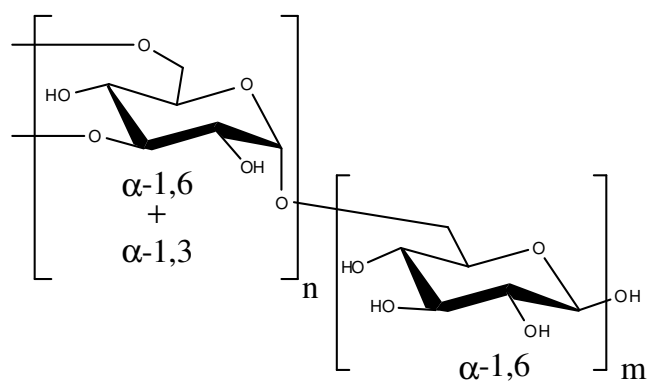


Figure 12. Dextran structure.

Despite the large number of papers dedicated to the preparation of metal colloid nanoparticles through wet chemical synthesis with the reduction of a metal salt in the presence of a stabilizer, it is not absolutely clear how the variables of the system (stabilizer, metal and reducing agent) influence the structure of the final material. However, it is clear that each component has an important role in the formation of metal nanoparticles and the synergism between them is quite important.^{12, 124} The methodologies used to optimize the M-NP preparation described in the

literature generally employ univariate methods, which do not take into account possible synergism between the variables. To address this issue, in this study we used a multivariate approach.

The quantitative optimization design chosen for this work was the so-called response surface model: a two-level factorial design expanded further to a central composite design with axial points. When the number of independent variables is small, then overlying the response surfaces and choosing the optimum conditions constitutes a simple and, in most cases, highly effective method. The analytical response (ψ) used for the plot of the response surfaces was estimated from Equation 6. :

$$\text{Equation 6. } \psi = \frac{A_{\max}}{\lambda_{\max} \text{FWHH}}$$

which combines the maximum absorbance (A_{\max}), which reflects the yield of the Ag-NPs formed,^{30, 125} the wavelength at A_{\max} (λ_{\max}), which is related to the size of the Ag-NPs,¹²⁵⁻¹²⁶ and the full width at half-height (FWHH), which is associated with the size dispersity of the Ag-NPs.^{30, 125} In this equation, the best response (ψ) would be obtained when the A_{\max} value is maximized and the λ_{\max} and FWHH values are minimized, indicating the formation of small narrow Ag-NPs.

The variables' optimization (concentrations of dextran, silver nitrate and sodium borohydride) in the AgNPs formation were performed using the experimental design cited above. It consisted in fifteen different experiments with more three repetitions of the central point, totalizing eighteen experiments. The values corresponding to each level and the central point are listed in Table 1, and in the Table 2 are listed all experimental combinations realized in the optimization.

The analysis of variance (ANOVA) is a statistical analysis that checks if there is a significantly difference between the averages and if the factors have influence in some dependent variable. Considering a confidence level of 95%, the results considering the analysis of variance (ANOVA, Table 14 of appendix 8.1) demonstrate that all three factors and the interactions [dextran] x [AgNO₃] and [dextran] x [NaBH₄] are statistically significant.

The Equation 7, indicating regression coefficients and their standard errors, illustrates the relationship of the three variables (x_1 , x_2 and x_3) and the analytical response (ψ):

$$\text{Equation 7. } \psi = -6.3(\pm 1.0) + 18.5(\pm 4.0)x_1 - 4.1(\pm 6.3)x_1^2 + 32.4(\pm 3.0)x_2 - 11.8(\pm 3.2)x_2^2 + 1.6(\pm 0.4)x_3 - 0.08(\pm 0.04)x_3^2 - 47.3(\pm 7.5)x_1x_2 - 2.8(\pm 0.9)x_1x_3 - 1.3(\pm 0.6)x_2x_3$$

where x_1 , x_2 and x_3 are dextran, AgNO₃ and NaBH₄ concentrations, respectively. This equation has a mean square lack of fit to mean square pure error ratio of 6.22, smaller than the 95% significant

$F_{5,3,95\%}$ value of 9.01 and a determination coefficient (R^2) of 0.98, indicating that the results obtained are reliable and the model does not suffer from lack of fit.

The response surfaces governed by this equation are shown in Figure 13. Each 3-D graph shows the normalized response as a function of two variables and the shape reflects the interactions and curvatures (or not) for the variables. From Figure 13a one can observe a maximum point at high silver nitrate concentration and low dextran concentrations. On the other hand, the maximum response is observed in Figure 13b when the dextran concentration is varied, but no effect in the response is observed with the variation in sodium borohydride concentration. However, in Figure 13c a strong effect of silver nitrate concentration was observed with a weak effect of sodium borohydride concentration, but no maximum was observed in this experiment, which may be related with the detection limit of the spectrophotometer. To verify that the response is linear and follows the Lambert-Beer law under the experimental conditions, an absorbance correlation with the Ag-NP concentrations was performed (Figure 14).

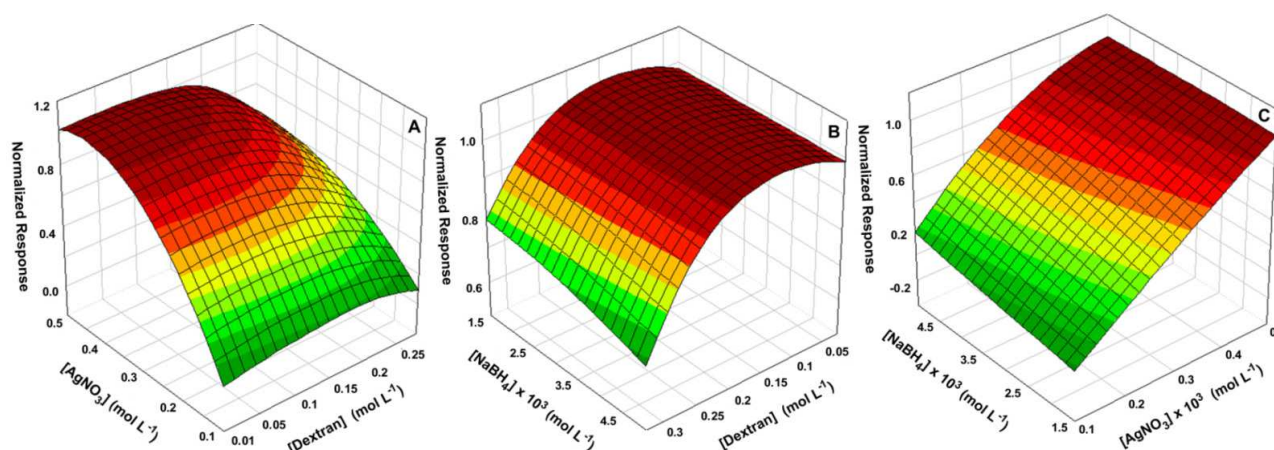


Figure 13: Response surfaces for the variables: (a) dextran and silver nitrate concentrations (indicate sodium borohydride level), (b) dextran and sodium borohydride concentrations (indicate silver nitrate level) and (c) silver nitrate and sodium borohydride concentrations (indicate dextran level).

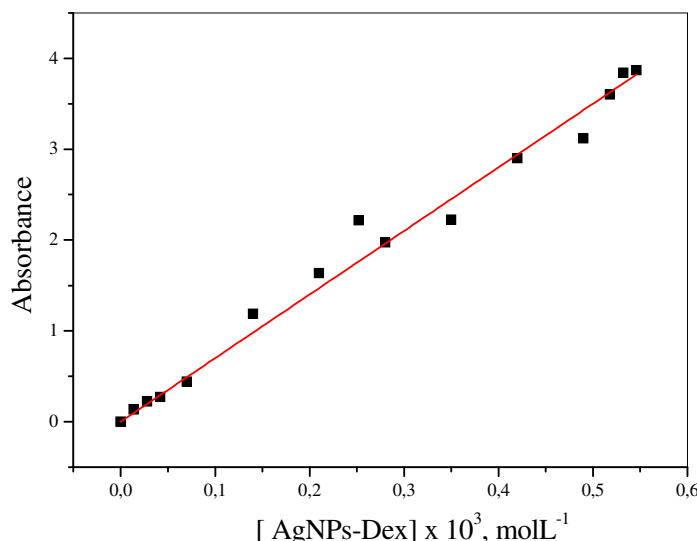


Figure 14. Correlation of absorbance with Ag-NP concentration.

The best conditions for the AgNP formation (called the optimal point), taking into account the combined analysis of the three graphs, were 6.3×10^{-3} , 0.5×10^{-3} and $3.0 \times 10^{-3} \text{ mol L}^{-1}$ of dextran, silver nitrate and sodium borohydride, respectively. The UV-Vis spectrum of this experimental condition is shown in Figure 15. The TEM analysis of this optimal point, presented in Figure 16, revealed nanoparticles with spherical geometry and low dispersity (small FWHH), as expected from Ag-NPs with a sharp UV-Vis band and λ_{max} around 400 nm,¹²⁵ validating the analytical response represented in Equation 6. . Through the Gaussian fits of the size distribution histogram, nanoparticles with mean diameters of $6.1 \pm 1.3 \text{ nm}$ were estimated. The theoretical specific surface area of the Ag-NPs was estimated from the TEM analysis and the density of bulk silver ($\rho = 10.5 \text{ gcm}^{-3}$).

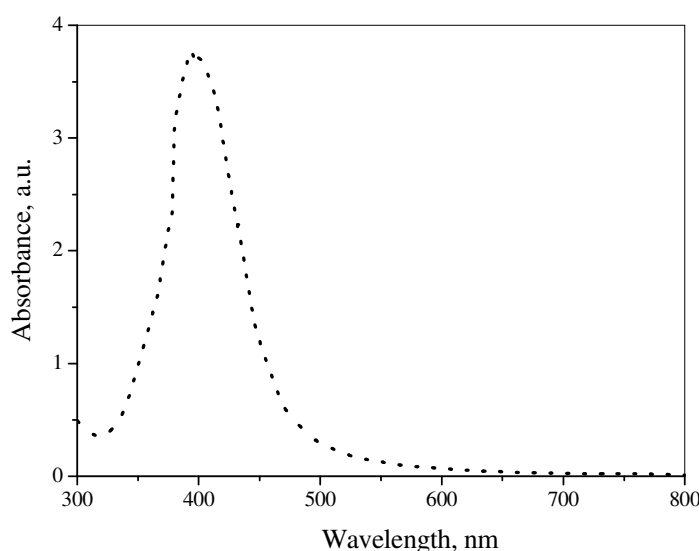


Figure 15: UV-Vis spectrum of the optimal point. $[\text{dextran}] = 6.3 \times 10^{-3} \text{ mol L}^{-1}$, $[\text{AgNO}_3] = 0.5 \times 10^{-3} \text{ mol L}^{-1}$ and $[\text{NaBH}_4] = 3.0 \times 10^{-3} \text{ mol L}^{-1}$.

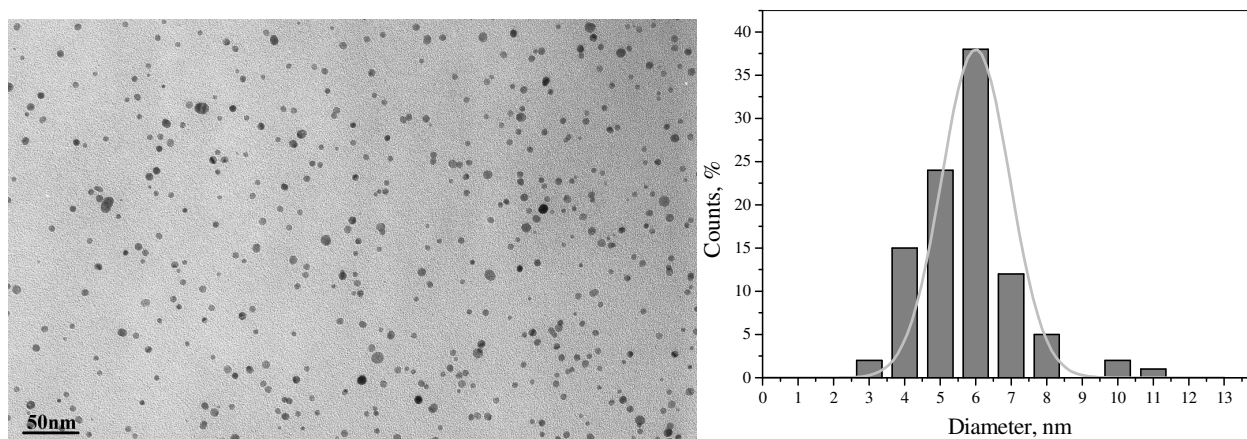


Figure 16: TEM micrograph and size distribution histogram for AgNPs-dextran. $[dextran] = 6.3 \times 10^{-3} \text{ mol L}^{-1}$, $[AgNO_3] = 0.5 \times 10^{-3} \text{ mol L}^{-1}$ and $[NaBH_4] = 3.0 \times 10^{-3} \text{ mol L}^{-1}$.

Additionally, the Ag-NPs-dextran composite was characterized by dynamic light scattering (DLS) as shown in Figure 17a. Three populations of particles can be observed with average sizes of $2R_h = 4.9 \text{ nm}$, 27.3 nm and 95.0 nm respectively. The smallest particles can be reasonably attributed to Ag-NPs since their size is consistent with the TEM observations. The particles with an average diameter of 27.3 nm may result from the presence of free dextran chains given that a similar relaxation-time distribution can be observed in Figure 17b for a solution of dextran alone. The third population can be attributed to aggregates containing AgNPs embedded in a dextran matrix. It should be noted here that the distribution presented Figure 17 is, by nature, a mass-weighted distribution. Consequently, although the peaks corresponding to the large-scale structures are the most intense, the number of aggregates is very low, as confirmed by their negligible presence in the TEM image.

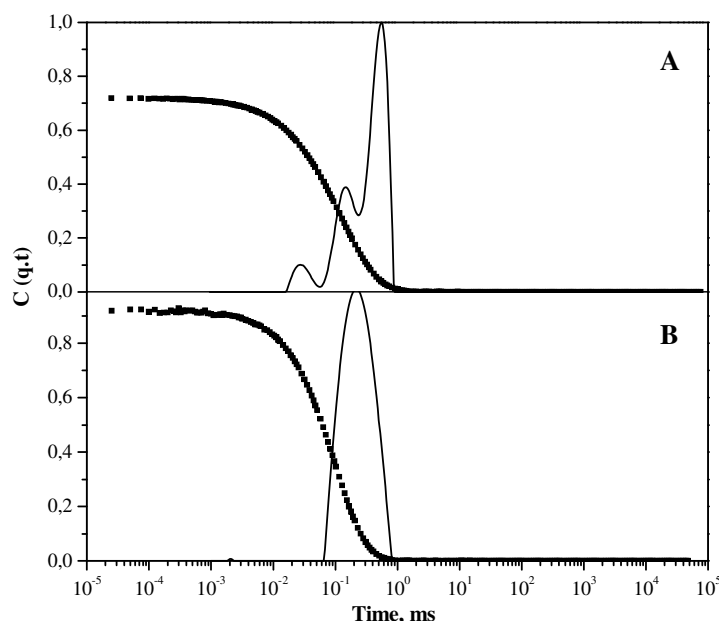


Figure 17: Dynamic light scattering autocorrelation function (squares) and relaxation-time distribution (solid line) for: (A) Ag-NPs-dextran at $[dextran] = 6.3 \times 10^{-3} \text{ mol L}^{-1}$, $[AgNO_3] = 0.5 \times 10^{-3} \text{ mol L}^{-1}$ and $[NaBH_4] = 3.0 \times 10^{-3} \text{ mol L}^{-1}$ and (B) dextran at $6.3 \times 10^{-3} \text{ mol L}^{-1}$.

5.1.2 Catalytic activity of AgNPs-dextran

The reduction reaction of *p*-nitrophenol (Nip) to *p*-aminophenol by sodium borohydrate (Figure 18) was used as model reaction to evaluate the catalytic activity of AgNPs-dextran. This reaction was monitored spectrophotometrically by measuring the disappearance of Nip (Figure 19), which shows a distinct spectral profile with an absorption maximum at 317 nm in water, but with a shift to 400 nm in the presence of $NaBH_4$ due to the formation of the *p*-nitrophenolate ion.^{58, 127} In order to obtain a full set of kinetic data, the influence of all reagents (Nip, AgNPs-dextran and $NaBH_4$) on the reaction were verified. In a typical set of experiments the concentrations of Nip and catalyst were kept constant and the $NaBH_4$ concentration was varied. At least a 100-fold excess of $NaBH_4$ over the concentration of Nip was used assuring *pseudo*-first-order conditions as it can be observed by the linear adjust of $\ln(A/A_0)$ (where A is the Nip absorbance) with time in the Figure 20.

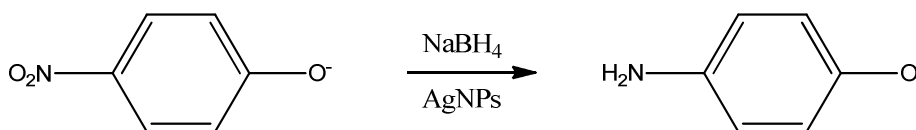


Figure 18. Reduction reaction of *p*-nitrophenolate to *p*-aminophenolate by $NaBH_4$ in presence of AgNPs.

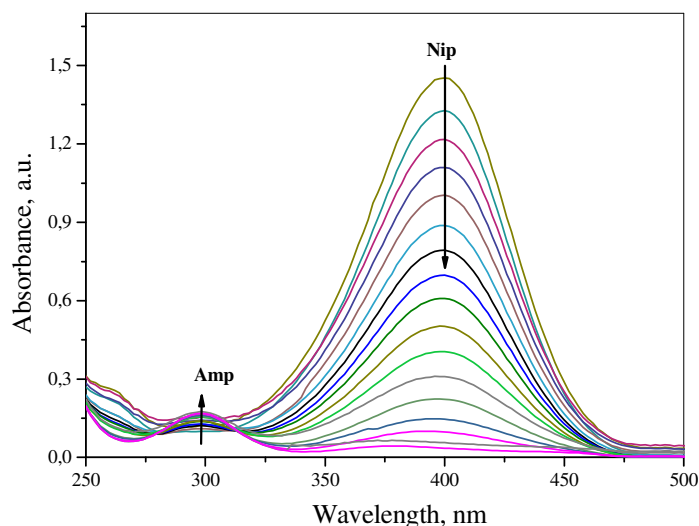


Figure 19: Variation in UV-Visible absorption spectra for the Nip reduction reaction in the presence of AgNPs-dextran ($[Nip] = 6.0 \times 10^{-5} \text{ mol L}^{-1}$, $[AgNPs] = 2.5 \times 10^{-6} \text{ mol L}^{-1}$, $[NaBH_4] = 6.0 \times 10^{-5} \text{ mol L}^{-1}$ and 25.0°C).

The induction time observed in the kinetic experiment showed in the Figure 20, have been reported in many works, in different catalytic systems, and it is normally interpreted as the required time to the reactants diffuse for the particles surface.⁸¹ For Zeng *et al.*,¹²⁸ the Nip adsorption rate on the catalyst surface is predominant factor in the induction time. However, Saha *et al.*⁷⁹ affirmed that induction time is normally associated with oxygen gas dissolved in the water, which reacts faster with borohydride anion than the Nip. In this work the second possibility can be excluded, because the solvents used to prepare all solutions were copiously degassed before use. Furthermore, the induction time presence is also related with an initial step involving the reactants' transport to M-NPs surface (Figure 9).⁸¹

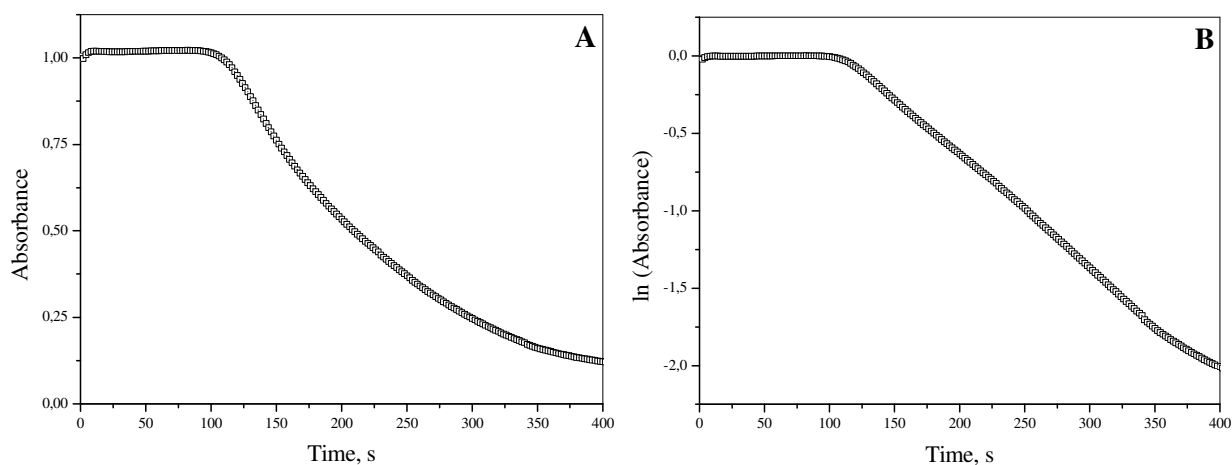


Figure 20. A: Nip's absorbance dependence vs time at 400 nm; B: The linear adjust of Fig. A for a first order kinetic. At $[Nip] = 8.8 \times 10^{-5}$, $[NaBH_4] = 8.8 \times 10^{-2}$, $[AgNPs] = 9.0 \times 10^{-7} \text{ mol L}^{-1}$.

Figure 21 shows that k_{app} increases with an increase in NaBH_4 concentration until it levels off, indicating that after a certain value the reaction proceeds independently of the NaBH_4 concentration, *i.e.* it becomes zero-order.

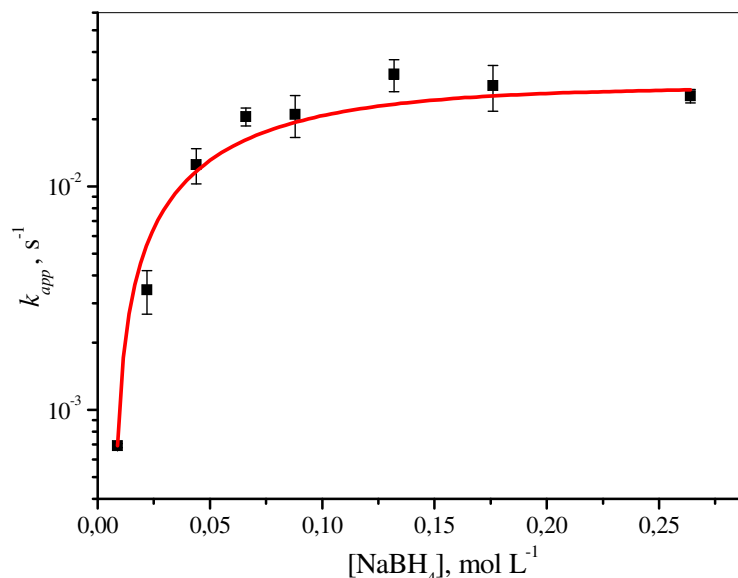


Figure 21: k_{app} as a function of NaBH_4 concentration at $[\text{Nip}] = 8.8 \times 10^{-5} \text{ mol L}^{-1}$, $[\text{Ag-NPs}] = 2.5 \times 10^{-6} \text{ mol L}^{-1}$ and 25.0°C . The solid line is a guide for the eyes.

During these experiments, we verified that the sodium hydroxide, used to improve the stabilization of borohydride, had a major influence on the apparent rate constant. Many studies reported in the literature use sodium hydroxide to adjust the NaBH_4 stock solution pH to between 10 and 11 in order to improve its stability in water.^{35, 129} However, none of them verified the influence of NaOH on the results of the kinetic experiments (*i.e.* over k_{app}), which is to be expected considering possible competition between HO^- and BH_4^- for the nanoparticle surfaces. Although not very prominent, NaOH indeed shows an intrinsic influence over k_{app} , as shown in Figure 22. At low NaOH concentrations, k_{app} increases reaching a maximum at $1 \times 10^{-3} \text{ mol L}^{-1}$ ($\text{pH} \approx 10$). After this point, k_{app} decreases quickly until it levels off at around $5 \times 10^{-3} \text{ mol L}^{-1}$ of NaOH .

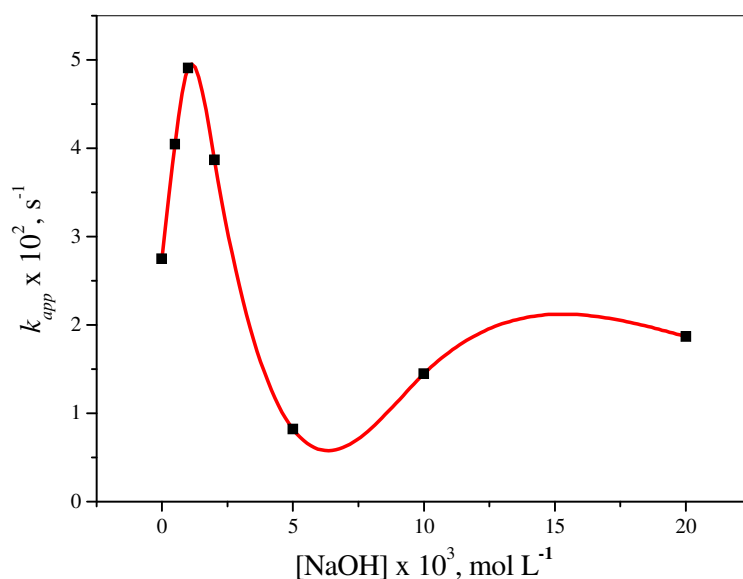


Figure 22. k_{app} as a function of NaOH concentration, at $[Nip] = 8.8 \times 10^{-5} \text{ mol L}^{-1}$, $[NaBH_4] = 8.8 \times 10^{-2} \text{ mol L}^{-1}$, $[Ag-NPs] = 2.5 \times 10^{-6} \text{ mol L}^{-1}$ at 25.0°C . The solid line is a guide for the eyes.

Competition for Ag-NP surfaces has previously been noted by Bell *et al.*,¹³⁰ who demonstrated that many different anions can bind to the Ag-NP surface, in many cases by displacement of other anions. In order to gather more information on the influence of NaOH, it was performed Zeta potential (ζ) measurements of Ag-NP-dextran in water solutions in the presence of $NaBH_4$ and at different NaOH concentrations (Table 5). The results show that the magnitude of the ζ is highest at $2 \times 10^{-3} \text{ mol L}^{-1}$ of NaOH, which coincides with a maximum in the apparent rate constant as shown in Figure 22. Higher concentrations of NaOH (10×10^{-3} and $20 \times 10^{-3} \text{ mol L}^{-1}$) lead to a sharp decrease in the ζ magnitude, probably by decreasing the system stability and also by lowering the ion mobility due to the increase in the ionic strength. Based on these results it was decided to use the stock solution of $NaBH_4$ in water (free of NaOH).

Table 5. Zeta potential (ζ) at different NaOH concentrations of Ag-NP-dextran in water solutions in the presence of $NaBH_4$.

[NaOH] x 10 ³ , mol L ⁻¹	0	2	10	20
ζ , mV	-7.21	-18.4	-14.2	-5.05
[NaBH ₄] = $8.8 \times 10^{-2} \text{ mol L}^{-1}$, [Ag-NPs] = $2.5 \times 10^{-6} \text{ mol L}^{-1}$ at 25°C .				

In the following experiments the $NaBH_4$ concentration was kept at a specific value where the reaction is guaranteed to be zero-order with respect to $NaBH_4$. The Nip influence over k_{app} is shown in Figure 23. In this profile, a decrease in k_{app} was observed with an increase in the Nip concentration. This can be attributed to competition between the two reactants for the reactive sites

of the Ag-NP surface. The increase in Nip concentration would induce extensive coverage of the Ag-NP surface, which in turn should decrease the electron supply at the metal surface by NaBH_4 . This behaviour was explained by Wunder *et al.* in terms of the Langmuir-Hinshelwood model, which assumes the adsorption of both reactants on the surface of the catalyst (Figure 9) in a reversible manner.⁸¹ The rate-determining step would consist of the reduction of Nip by the surface hydrogen species.

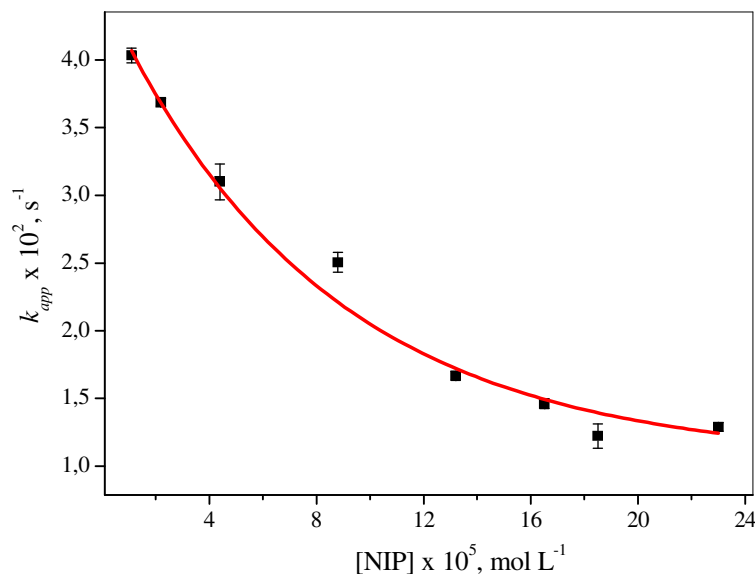


Figure 23: k_{app} as a function of Nip concentration at $[\text{NaBH}_4] = 8.8 \times 10^{-2} \text{ mol L}^{-1}$, $[\text{Ag-NPs}] = 2.5 \times 10^{-6} \text{ mol L}^{-1}$ and 25.0°C . The solid line is a guide for the eyes.

Since under micro-heterogeneous conditions it is well accepted that the apparent kinetic rate constant is proportional to the total surface area of all metal nanoparticles,^{16, 35, 62, 65, 131} the rate of the reduction reaction of Nip can be expressed as

$$\text{Equation 8. } -\frac{d[\text{Nip}]}{dt} = k_1 S[\text{Nip}][\text{NaBH}_4]$$

where S is the surface area of the metal nanoparticles normalized to the unit volume of the reaction system and k_l is the rate constant normalized to S . Associated with the fact that at certain conditions the reaction is zero-order with respect to NaBH_4 , the Equation 8 can be write as

$$\text{Equation 9. } -\frac{d[\text{Nip}]}{dt} = k_1 S[\text{Nip}] = k_{app}[\text{Nip}]$$

This expression assumes a *quasi*-homogeneous catalysis conditions,¹³² and a zero order dependence of NaBH_4 in the reaction. The plot of k_{app} as a function of the surface area S is shown in Figure 24. It can be observed that the rate constant k_{app} is indeed proportional to the total surface area of the nanoparticles in the system; hence, it can be concluded that catalysis takes place on the surface of the nanoparticles.

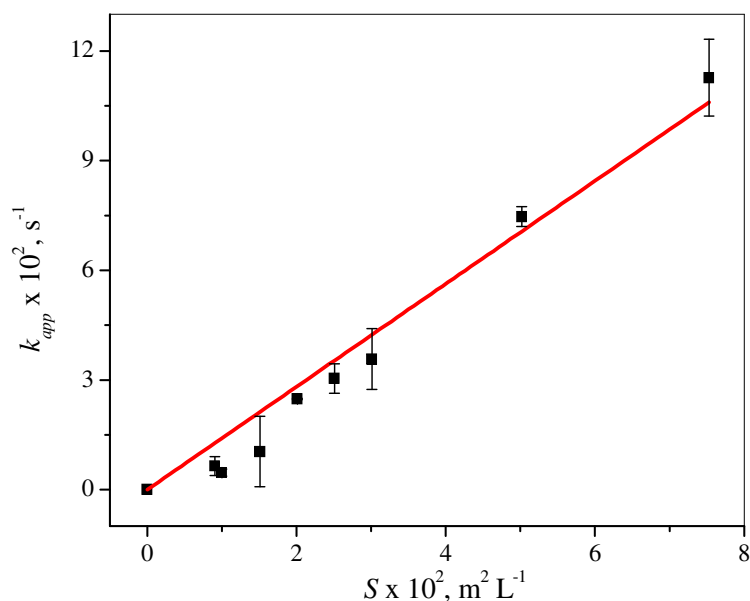


Figure 24: k_{app} as a function of Ag-NP total surface area (S), at $[\text{NaBH}_4] = 8.8 \times 10^{-2} \text{ mol L}^{-1}$, $[\text{Nip}] = 8.8 \times 10^{-5} \text{ mol L}^{-1}$ and 25.0°C .

From the angular coefficient for the plot in Figure 24, the rate constant k_1 was determined to be $1.41 \pm 0.07 \text{ s}^{-1} \text{ m}^{-2} \text{ L}$, an extraordinarily high catalytic efficiency when compared with other silver nanoparticle catalysts reported in the literature (Table 6). In all cases, AgNPs were used for the reduction of Nip with a large excess of NaBH_4 .

The comparison and rationalization of the values listed in Table 6 is rather difficult, and attribution of these catalytic effects to other reason than due the high surface area presented by metal nanoparticles is speculation. Indeed, many variables are believed to also play an important role in the catalytic activity of such systems, particularly the nature of the stabilizer.^{12, 131, 133-134} When the interaction between the M-NP and stabilizer backbones, normally presenting sulphur or nitrogen atoms, is too strong, the size of the NPs became smaller while the catalytic activity is diminished. In the case of AgNPs-dextran (Entry 1, Table 6), the moderate interaction between AgNPs and oxygen atoms in dextran backbones might allow an efficient equilibrium between NPs stabilization and catalysis. Moreover, dextran as a polysaccharide, presents both hydrophobic and hydrophilic regions, which can form multiple intermolecular interactions in aqueous systems.¹³⁵ These hydrophobic domains in the polymer backbone may increment the hydrophobicity

surrounding the reaction microenvironment, which would be responsible to draw in substrates from aqueous medium increasing the local substrate concentration, and consequently, accelerating the reaction rate. These results suggest that the catalytic performance of AgNPs depends on both the surface functional groups and the structures of the stabilizer/support.

Table 6. Comparison between catalytic activities of silver nanoparticles systems in p-nitrophenol reduction.

Entry	Stabilizer	Temperature	D _m , nm ^b	k ₁ , (s ⁻¹ m ⁻² L) ^c
1	F1-LPEI ⁷⁵	15.0°C	34 ± 9	1.66
2	Dextran T500 ^a	25.0°C	6.1 ± 1.3	1.41
3	TiO ₂ ⁷⁷	21.0°C	3	0.78
4	Derivatized PEI ¹⁰	25.0°C	24.5 ± 4.1	0.57
5	F12-LPEI ⁷⁵	25.0°C	30 ± 10	0.37
6	Carboxymethyl chitosan microgel ¹³⁶	25.0°C	3.45 ± 0.65	0.196
7	Aminosilicate ¹³⁷	25.0°C	~3.6	0.188
8	Quitosan ⁵⁸	25.0°C	~3	0.15
9	Carboxymethyl chitosan microgel ¹³⁶	25.0°C	2.81 ± 0.62	0.124
10	Anionic polyelectrolyte brush ¹³⁸	25.0°C	3.0 ± 1.2	0.078

^a This work. ^b Diameter of metal nanoparticles. ^c Rate constant normalized to surface area of metal nanoparticles per volume unit.

5.2 Silver nanoparticles stabilized by oligosaccharides-based amphiphiles

5.2.1 Synthesis of oligosaccharides-based amphiphiles

Since the emergence of so-called green chemistry,¹³ materials and compounds from renewable resources have gained space. Despite the increase in the utilization of polysaccharides as stabilizers/supports^{20, 55, 58, 74, 139} and mono and disaccharides^{36, 140} as reducing agents in metal nanoparticles formation, few works are dedicated to oligosaccharides modification and their utilization as stabilizers⁴⁶ of M-NPs.

In order to prepare new stabilizers based on oligosaccharides with a chemical function susceptible to allow further chemical modifications, two kinds of oligosaccharides-based amphiphiles were designed (Figure 25): one with a functional group at the end of hydrophobic

block (A) and the other with a functional group in the junction of hydrophilic and hydrophobic blocks (B). These groups were designed for further chemical modifications introducing new chemical groups to improve the nanoparticles stabilization, for example, or improve their size and morphology or bind the amphiphiles to resins, reducing agents, etc. For hydrophobic blocks were used fatty acids or their derivatives and for hydrophilic blocks were chosen different oligosaccharides (maltose (Mal), lactose (Lac), maltoheptaose (Mal₇) and xyloglucan-oligosaccharide (XGO)). The choice of these oligosaccharides was made by their low cost of production. Maltose, for example, is one of the products of starch hydrolysis by α -amylase and several million tons of lactose are produced annually as a by-product of the dairy industry. Maltoheptaose and xyloglucan oligosaccharides were selected because of their ease of preparation and controlled narrow size-polydispersity. The maltoheptaose was obtained from β -cyclodextrin,¹¹⁹ which is a by-product of starch hydrolysis by α -amylase combined with cyclodextrin glycosyltransferase (CGTase) and xyloglucan-oligosaccharide is obtained from abundant hemicellulose which can be depolymerized in controlled way by cellulases.¹⁴¹

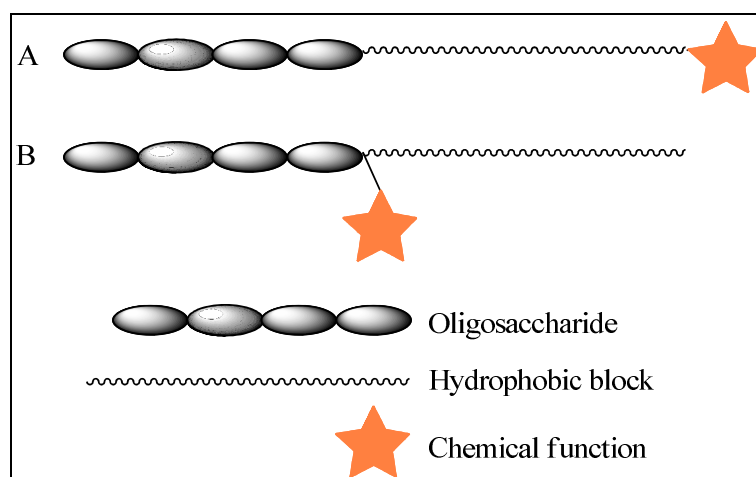


Figure 25: General representation of different amphiphiles prepared.

For the amphiphiles with a functional group in the junction of hydrophilic and hydrophobic blocks, it was opted to use a terminal alkyne group, because it is a good functional group to promote click chemistry¹⁴² reactions with good yields and selectivity. The propargylamine, a primary amine with three carbons and a terminal alkyne, was chosen as the reactant. Its choice was based in its facility to react with a reducing sugar. This derivative, however, is easily hydrolyzed in presence of water, which can be avoided by: performing a reductive amination or a second reaction after the amination, which may be an alkylation or an acylation. It was opted for an acylation, which can be performed selectively, keeping the first oligosaccharide ring intact.

Only two derivatives were prepared with the alkyne group, Figure 26 shows the general reaction scheme for their obtention. In the first step, the disaccharide maltose is dissolved in a great excess of propargylamine ($\sim 21\times$) and stirred for 72 hours, then the propargylamine excess is evaporated and the crude glycosylamine is selectively *N*-acylated. For the synthesis of the octanoic derivative (MalNOcta), octanoic anhydride was used as acylating agent; it was prepared (some hours before its utilization) by reacting octanoic acid and *N,N'*-dicyclohexylcarbodiimide (DCC), the product yield was 65% (Table 7, entry 1). For the octadecanoic derivative (MalNOctD), after several attempts seeking for the best reaction condition, we chose to use stearoyl chloride as acylating agent and 2,6-lutidine as base. The yield obtained for this derivative was lower, 37%, due the formation of side products and difficulties in the purification.

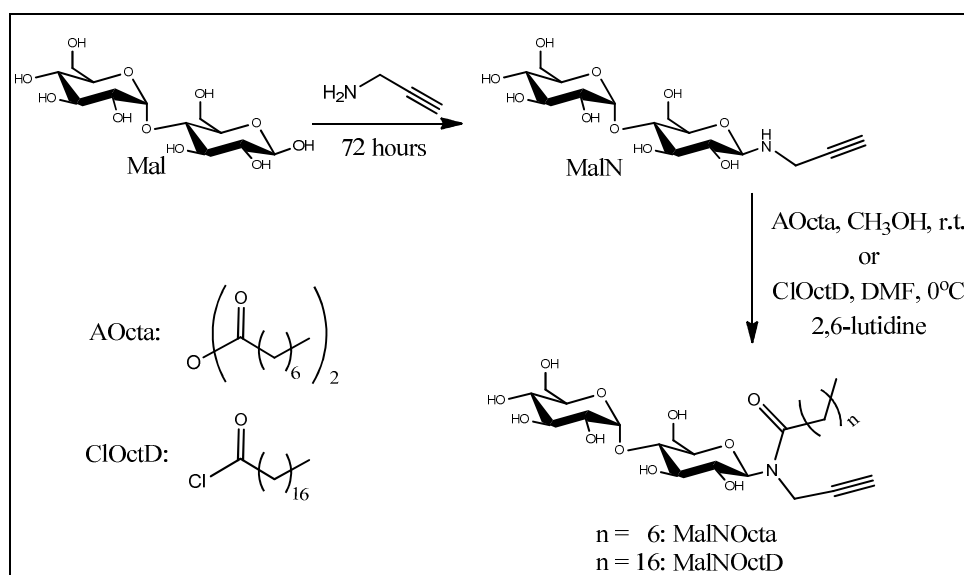


Figure 26: Reaction scheme to obtain the *N*-(maltosyl)-3-octanamide-1-propyne (MalNOcta) and the *N*-(maltosyl)-3-octadecylamide-1-propyne (MalNOctD).

The MalNOcta and MalNOctD structures were confirmed by mass spectrometry with electrospray ionization (MS ESI) and by ^1H and ^{13}C NMR. Some attempts to prepare this kind of amphiphile with bigger oligosaccharide, as maltoheptaose for example, were realized. Unfortunately, only traces of the target compounds were detected in the synthesis and it was not possible to improve their preparation.

For the second amphiphile kind, with a chemical function at the end of hydrophobic block, it was opted to insert a carboxylic acid group. Two carboxylic acids with long linear chain (six and twelve carbons) with an azide functional group in its omega carbon (last carbon in the alkylic chain from the acid group) were chosen. The azide derivatives were prepared from their respective omega-bromo acids, reacting them with sodium azide in DMF for twenty hours at 90.0 °C. They

were purified by liquid-liquid extraction with high yields and their formation confirmed by NMR (triplet at $\delta \sim 3.25$ in ^1H NMR and peak at $\delta \sim 51$ in ^{13}C NMR, relatives to CH_2N_3). To link it with the oligosaccharides, the sugars were modified with propargylamine in their reducing end and *N*-acetylated, and linked to the carboxylic fatty acids by Huisgen cycloaddition (between the terminal alkyne and the azide) (Figure 27). This approach was chosen due to the selectivity and good yields that it provides (Table 7).

Table 7. Yield obtained in the amphiphiles synthesis.

Entry	Compound	Yield (%)
1	MalNOcta	65
2	MalNOctD	37
3	MalNAcC ₆	85
4	MalNAcC ₁₂	40
5	XGONAcC ₆	82
6	XGONAcC ₁₂	80
7	Mal ₇ NAcC ₆	95
8	Mal ₇ NAcC ₁₂	80
9	LacNAcC ₁₂	64

Seven different amphiphile compounds (entries 3 to 9) were synthesized by the Huisgen cycloaddition using four different oligosaccharides (maltose (Mal), xyloglucan oligosaccharide (XGO), maltoheptaose (Mal₇) and lactose (Lac)) and the two acid derivatives (Figure 27). To form the catalytic specie in the reaction medium (Cu^+), it was chosen the mixture CuSO_4 and sodium ascorbate and mixtures of water/THF or water/isopropanol as solvent to solubilise all reactants. At room temperature only traces of the expected products were observed, so the reaction temperature was optimized at 40.0°C . The yield for each compound varied between 40 and 95% (Table 6) and all compounds were characterized by ^1H and ^{13}C NMR and mass spectrometry.

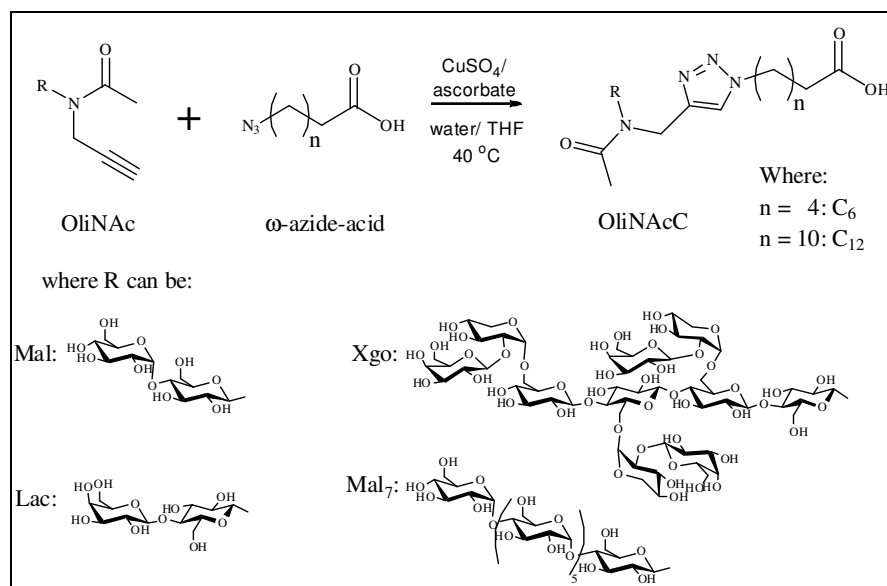


Figure 27: Reaction scheme to obtainment of ω -(4-((N-(oligosaccharide)acetamido)methyl)-1H-1,2,3,-triazole-1-yl) carboxylic acids (OliNAcC).

Analyzing the yields listed in the Table 7, it is observed a tendency of increase in the yield of products obtained when the hydrophilic / hydrophobic balance is shifted to the hydrophilic side. The reason of this tendency is not clear, but the formation of aggregates in the reaction medium may be an explanation for this experimental observation, however, without conducting additional experiments this possibility is just speculation and it is not in the aim of this work.

These two amphiphile structures were chosen due the different organization that they can provide in the metal nanoparticle surface (Figure 28). For example, in basic conditions as shown in the Figure 28, the acid group in the amphiphile compounds (A) is ionized acting as a second hydrophilic group. In this configuration it can stabilize AgNPs forming a monolayer at the nanoparticle surface. In the other hand, the amphiphile compounds with alkyne group behave as a classical surfactant and form a bilayer in the nanoparticle surface. These differences in the stabilization will probably affect the nanoparticles properties, giving distinct properties to the different systems.

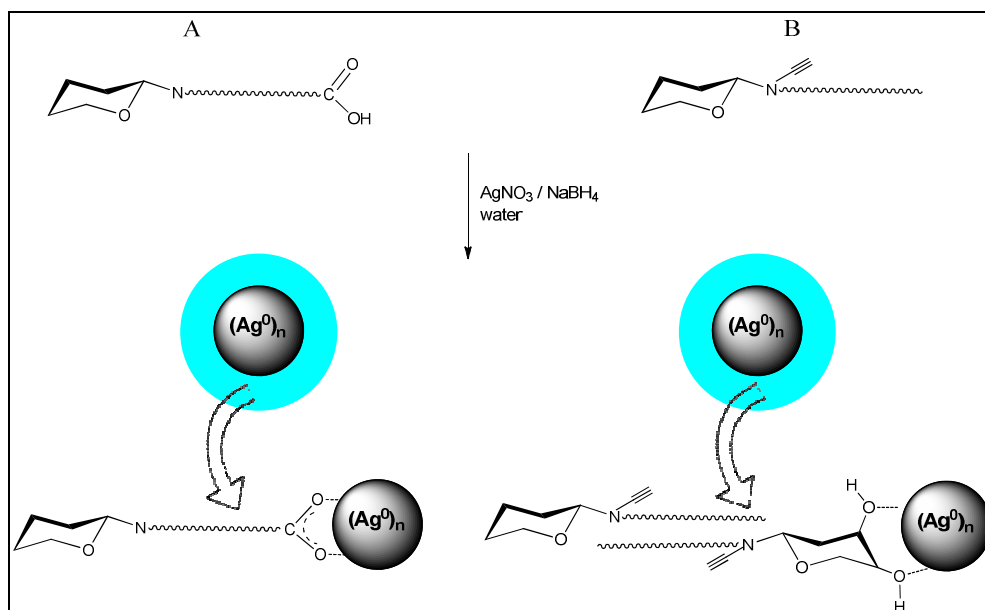


Figure 28. Expected stabilization mechanism for the different kinds of amphiphile compounds prepared.

5.2.2 Preparation and characterization silver nanoparticles stabilized by oligosaccharides-based amphiphiles

As for the optimization of AgNPs-dextran, it was opted for the utilization of a multivariate analysis to optimize the preparation conditions of the AgNPs stabilized by the different amphiphile compounds synthesized. The same methodology described for AgNPs-dextran optimization were used, but with a little modification: in the optimizations with the amphiphiles, the AgNO_3 concentration was fixed. This decision was taken based in the informations obtained from Figure 13 A and B. It was observed that when AgNO_3 concentration was increased the response increases steadily. Normally in this case a new optimization should be done seeking for the curve's maximal region, however in this case it was not possible due to experimental limitation of the spectrophotometric technique. So after some preliminary experiments, we chose to fix the AgNO_3 concentration as largest as possible within the reading limits of the spectrophotometer. Besides reducing the number of experiments, another advantage of fixing AgNO_3 concentration is to decrease the number of variables and data to be analyzed, which increases the method's reliability.

143

For the optimization of the preparation conditions of the AgNPs stabilized by the different amphiphile compounds, it was chosen a 2^2 experimental design with central composite and axial points to optimize the amphiphile compounds concentration and NaBH_4 concentration in the

AgNPs preparation. As for AgNPs-dextran, the analytical response (ψ) used to evaluate the AgNPs formation was Equation 6.

The normalized response was evaluated at a confidence level of 95%, the results considering the analysis of variance for each system (ANOVA, Appendix 8.3) demonstrate that all factors and the interactions [stabilizer] x [NaBH₄] are statistically significant for MalNAcC₁₂, LacNAcC₁₂, Mal₇NAcC₁₂ and XGONAcC₆ while for Mal₇NAcC₆ and XGONAcC₁₂ the interaction [stabilizer] x [NaBH₄] is not statistical significant and for MalNOctD just NaBH₄ concentration is statistically significant. Equation 10 illustrates the relationship of the two variables (x_1 and x_2 , stabilizer and NaBH₄ concentration respectively) and the normalized analytical response (ψ). The coefficients and their standard errors (for the statistical relevant factors), lack of fit and determination coefficient (R^2) for all systems are listed in the Table 8.

$$\text{Equation 10. } \psi = a + bx_1 + cx_1^2 + dx_2 + ex_2^2 + fx_1x_2$$

The equation for each system has a mean square lack of fit to mean square pure error ratio smaller than the 95% significant $F_{2,2,95\%}$ value of 19.00 and a determination coefficient (R^2) at least of 0.85, indicating that the results obtained are reliable and the model does not suffer from lack of fit.

Table 8. Regression coefficients of surface curves, lack of fit and the coefficient determination (R^2).

Amphiphile	a	b	c	d	e	f	Lack of Fit	R^2
MalNOcta ^a	-	-	-	-	-	-	-	-
MalNOctD	0.024 ± 0.16	- ^c	- ^c	0.16 ± 0.029	-0.012 ± 0.002	- ^c	12.6	0.87
MalNAC ₆ ^b	-	-	-	-	-	-	-	-
MalNAC ₁₂	0.39 ± 0.034	0.071 ± 0.016	-0.011 ± 0.0013	0.080 ± 0.016	-0.009 ± 0.0015	0.018 ± 0.0014	18.6	0.85
XGONAC ₆	-0.12 ± 0.03	0.46 ± 0.01	-0.058 ± 0.002	-0.052 ± 0.007	0.016 ± 0.0004	-0.028 ± 0.002	13.5	0.99
XGONAC ₁₂	-0.14 ± 0.04	2.50 ± 0.09	-1.81 ± 0.05	0.053 ± 0.009	-0.005 ± 0.0006	- ^c	18.0	0.98
Mal ₇ NAC ₆	1.56 ± 0.22	0.37 ± 0.05	-0.009 ± 0.003	-0.17 ± 0.04	- ^c	- ^c	3.78	0.99
Mal ₇ NAC ₁₂	0.77 ± 0.07	0.73 ± 0.03	-0.15 ± 0.0004	-0.048 ± 0.016	-0.011 ± 0.001	0.049 ± 0.004	17.7	0.98
LacNAC ₁₂	-0.128 ± 0.077	0.466 ± 0.0935	-0.196 ± 0.032	0.126 ± 0.017	-0.015 ± 0.0011	0.075 ± 0.014	18.1	0.94

^a Only one condition has AgNPs stable. ^b No stable AgNPs were formed. ^c Not statistical significant.

The response surface governed by the Equation 10 for the Mal₇NAC₁₂ system is shown in Figure 29 (the surface response for the others systems are in the appendix 8.4). The 3-D graph shows the normalized response as a function the two variables and the shape reflects the interactions and curvatures (or not) for the variables. A maximum response is observed when the Mal₇NAC₁₂ concentration is varied, but a small effect in the response is observed with the variation in sodium borohydride concentration.

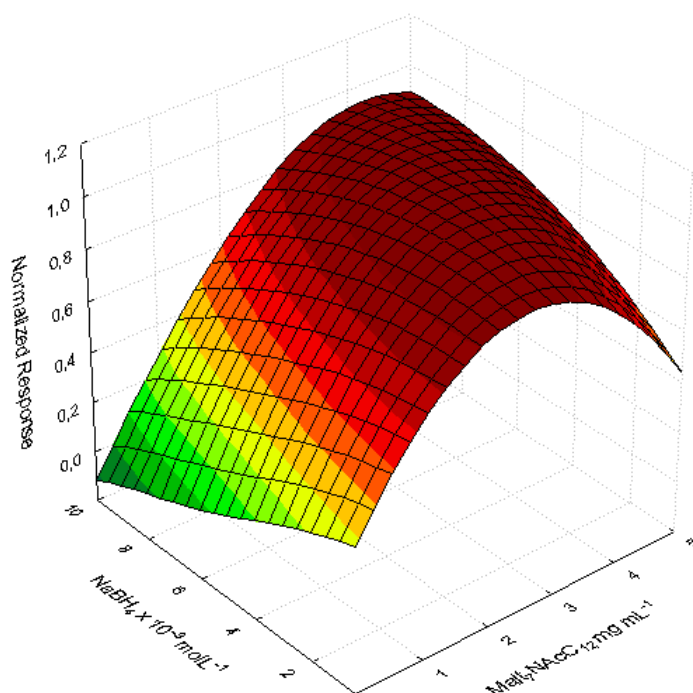


Figure 29. Response surface for $\text{Mal}_7\text{NAC}_{12}$.

The best conditions for the AgNPs formation (optimal points) for each stabilizer, taking into account the analysis of each surface response, are listed in Table 9. The UV-Vis spectra of the AgNPs at these experimental conditions are shown in Figure 30. These spectra show sharp UV-Vis bands with a λ_{max} around 400 nm, typical profiles for silver nanoparticles with spherical geometry and low dispersity,¹²⁵ validating the analytical response represented by Equation 6. .

Table 9. Optimal concentrations of stabilizer and NaBH_4 for each system.

Compound	[Stabilizer] mg mL^{-1}	[NaBH_4] mmol L^{-1}
MalNOcta	50.5	9.0
MalNOctD	0.07	9.0
MalNAC ₆ ^a	-	-
MalNAC ₁₂	7.9	7.0
XGONAC ₆	1.5	10.0
XGONAC ₁₂	0.75	7.0
Mal ₇ NAC ₆	10.0	0.5
Mal ₇ NAC ₁₂	3.0	5.0
LacNAC ₁₂	2.0	8.0

^a No stable AgNPs was formed for this compound.

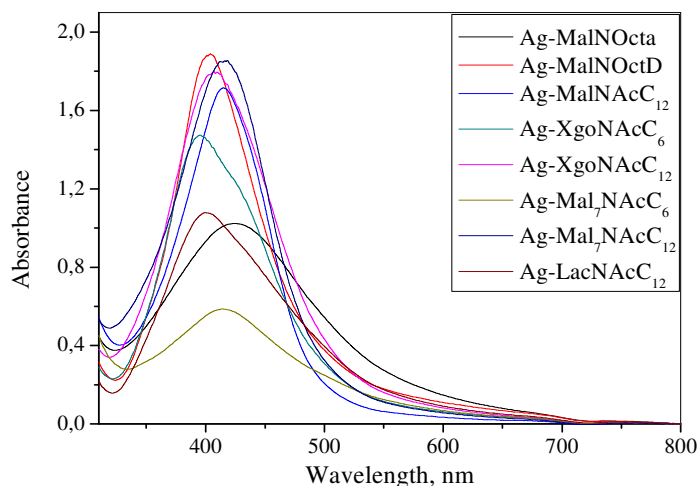


Figure 30. UV-vis spectra of all optimal conditions for AgNPs preparation.

The TEM analysis of AgNPs stabilized by the different amphiphile compounds at the optimal points are shown in Figure 31, except for Ag-Mal₇NAC₆ nanoparticles, which did not show temporal stability, so no further characterization was performed for this system. The mean diameters of the nanoparticles were estimated by transmission electron microscopy (TEM), small angle X-ray scattering (SAXS) and dynamic light scattering (DLS) (Table 10).

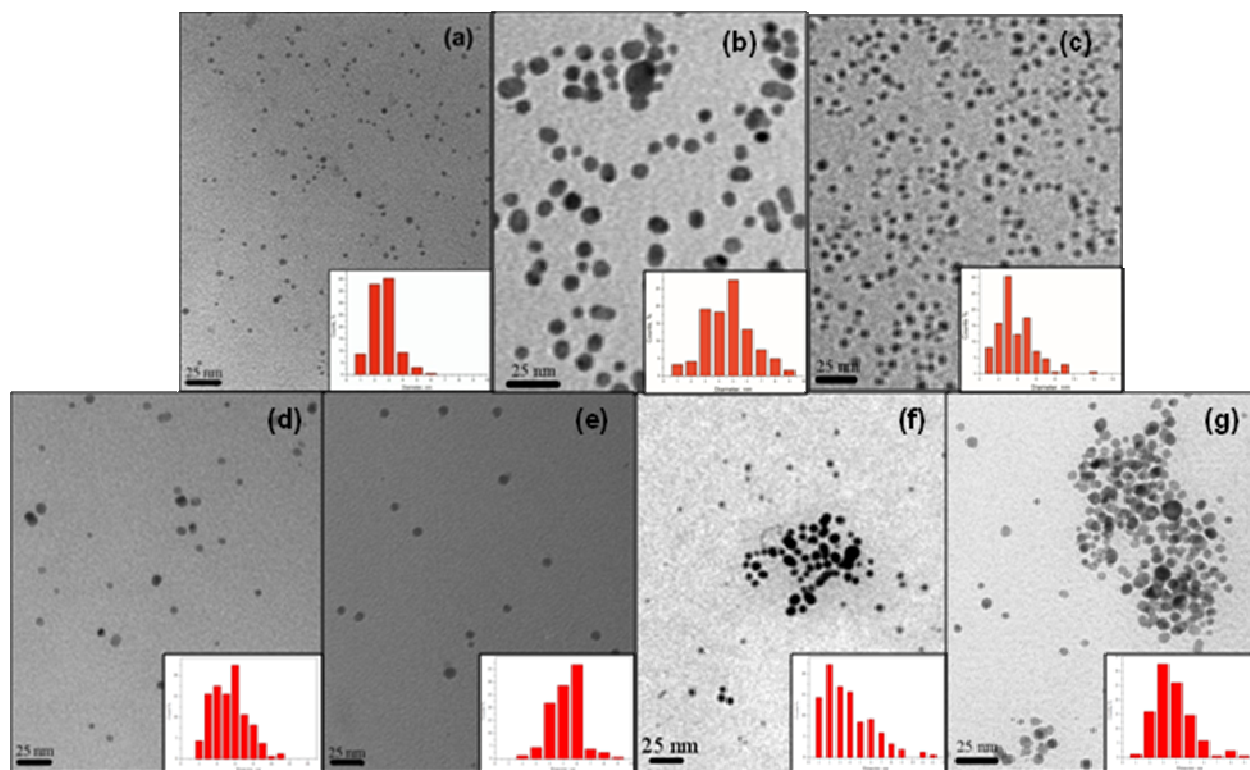


Figure 31. TEM micrographs and size distribution histograms (insets) for (a) Ag-Mal₇NAC₁₂, (b) Ag-XGONAC₆ and (c) Ag-XGONAC₁₂ (d) MalNOctD (e) Ag-MalNAC₁₂ (f) Ag-LacNAC₁₂ (g) MalNOcta nanoparticles at the optimal synthesis conditions (Table 9).

Table 10 . Diameter of AgNPs obtained by transmission electron microscopy (TEM), small angle X-ray scattering (SAXS) and dynamic light scattering (DLS)

Compound	D _m ^a by TEM, nm	D _m by SAXS, nm	D _m by DLS (2x R _h), nm
MalNOcta	4.18 ± 1.32	4.14 ± 0.27	3.66
MalNOctD	5.83 ± 1.88	8.27 ± 0.24	2.75
MalNAcC ₁₂	5.73 ± 1.08	5.20 ± 0.27	9.10
XGONAcC ₆	6.52 ± 6.32	7.08 ± 0.32	7.04
XGONAcC ₁₂	4.24 ± 1.92	4.49 ± 0.18	14.4
Mal ₇ NAcC ₆ ^b	-	-	-
Mal ₇ NAcC ₁₂	3.16 ± 0.84	4.22 ± 0.57	7.04
LacNAcC ₁₂	4.28 ± 2.11	5.54 ± 0.37	6.61

^a Metal nanoparticles diameter. ^b No stable nanoparticles were formed.

SAXS measurements were also performed in order to probe the size, shape, and dispersity of the scattering particles. Figure 32 shows the SAXS profiles of Mal₇NAcC₁₂ growth under the same conditions used to obtain the TEM images.

The SAXS scattering intensity $I(q)$ of an isotropic solution of particles embedded in a matrix with a constant electron density, after normalization considering the background scattering of the solvent, is given by

$$\text{Equation 11. } I(q) = NP(q)S(q)$$

where N is the number of particles per unit volume, $P(q)$ is the form factor of an individual particle, and $S(q)$ is related to the particle interference factor, which arises from long-range correlations between scattering centers. For widely separated systems (as in the current case), $S(q) \sim 1$ and $I(q)$ is due to the form factor $P(q)$ of the scattering objects, which is linked to their size and shape. Herein, $P(q)$ values of the Ag-NPs were modelled geometrically as homogeneous spheres:

$$\text{Equation 12. } I(q) = V_p^2 \Delta \sigma^2 P(q, R) = \left(\frac{4}{3} \pi R^3 \Delta \sigma \right)^2 \left(\frac{3 [\sin(qR) - qR \cos(qR)]}{(qR)^3} \right)^2$$

The sample dispersity was taken into account by using the log-normal distribution, for which the probability density function is given by

$$\text{Equation 13. } f(R, \mu, \sigma) = \frac{1}{\sqrt{2\pi}\sigma R} \exp - \frac{\ln(R/\mu)^2}{2\sigma^2}$$

where R is the average radius and the parameters μ and σ are the mean and standard deviation of the distribution, respectively. The parameter σ gives quantitative information about the particle dispersity. This fitting approach describes the experimental results reasonably well and led to values listed in Table 10. These values obtained by SAXS are very close to that determined by TEM.

The Ag-amphiphiles nanoparticles systems were characterized by DLS measurements, the hydrodynamic radius (D_h) are show in Table 10 and the correlation curves in Figure 33. For all systems, more than one population was detected, but no correlation curves were detected for the amphiphiles compounds in the absence of metal nanoparticles, except for MalNOcta system, in this case a population with the same relaxation-time of the larger population in Ag-MalNOcta. This population is due the to formation of MalNOcta micelles which is evidenced by the SAXS broad shoulder (Figure 32g) at 2 nm.¹⁴⁴ For the others systems as there are not SAXS evidence of micellization and the size distribution presented in Figure 33 is, by nature, a mass-weighted distribution, the peaks corresponding to the large-scale structures are the most intense, however, the number of aggregates is very low and can be neglected. The sizes obtained by DLS were approximately the same values determined by SAXS and TEM.

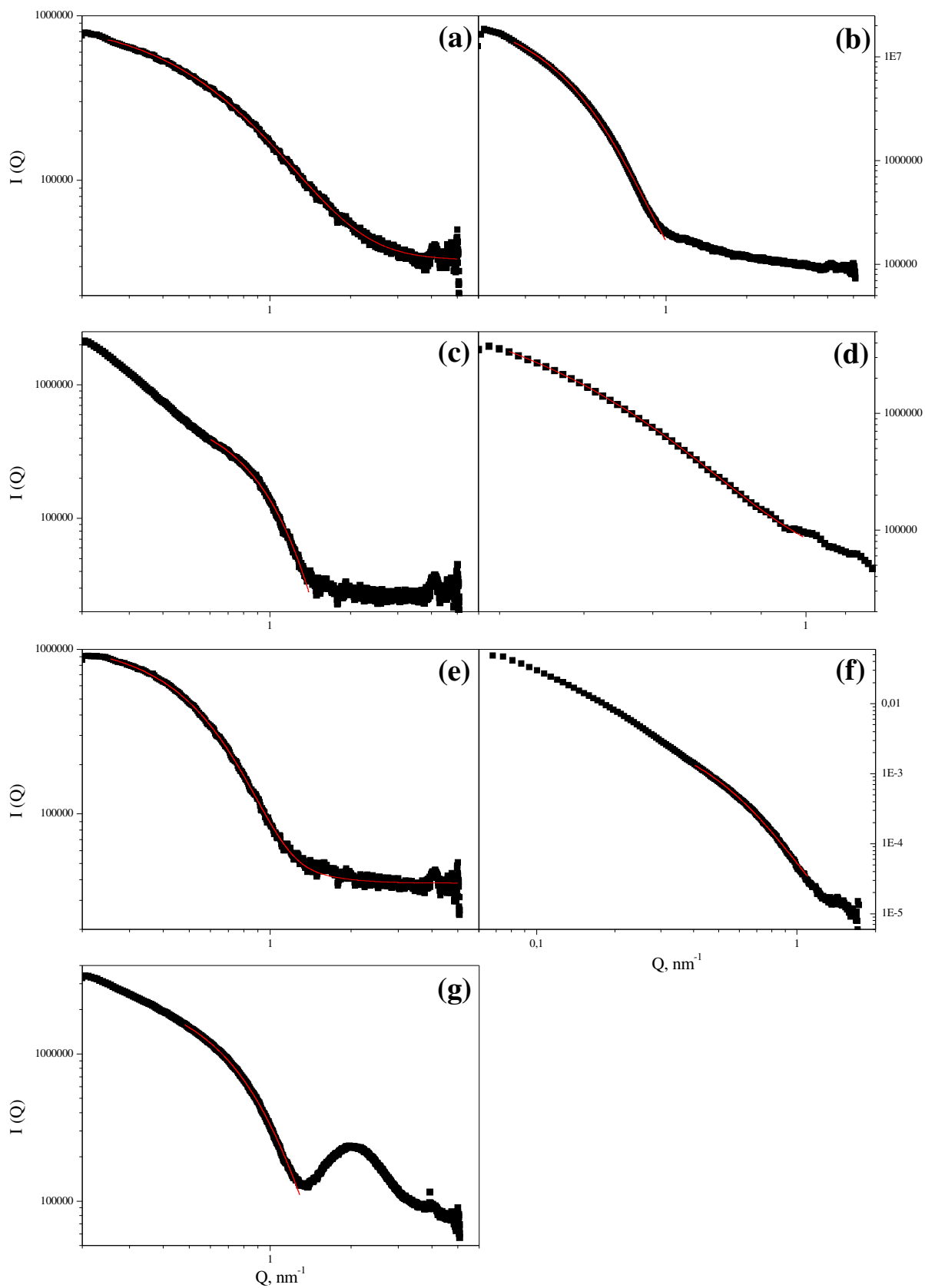


Figure 32. SAXS data (squares) and corresponding curve fitting (line) for (a) Ag-Mal₇NAC₁₂, (b) Ag-XGONAcC₆ and (c) Ag-XGONAc₁₂ (d) MalNOctD (e) Ag-MalNAC₁₂ (f) Ag-LacNAC₁₂ (g) MalNOcta nanoparticles at the optimal synthesis conditions (Table 9).

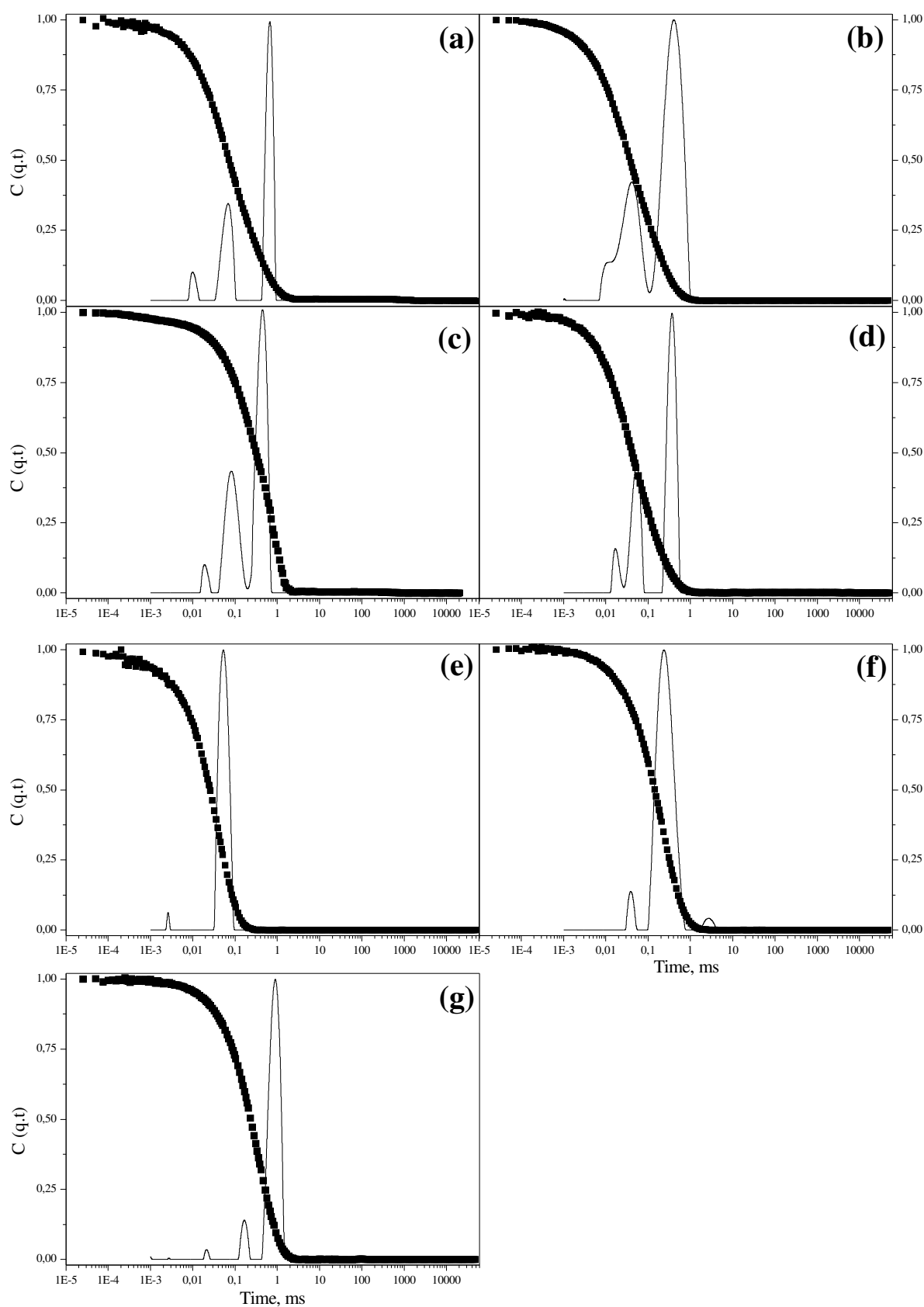


Figure 33. DLS autocorrelation function (squares) and relaxation-time distribution (solid line) for (a) Ag-Mal₇NacC₁₂, (b) Ag-XGONAcC₆ and (c) Ag-XGONAcC₁₂ (d) MalNOctD (e) Ag-MalNacC₁₂ (f) Ag-LacNacC₁₂ (g) MalNOcta nanoparticles at the optimal synthesis conditions (Table 9).

In order to confirm the micelles presence in Ag-MalNOcta system, its critical micelle concentration (*cmc*) was determined by light scattering. In the Figure 34 is presented the light scattering intensity and the hydrodynamic radius (R_h) variation as function of MalNOcta concentration. Both profiles show an abrupt change at $\sim 17 \text{ mg mL}^{-1}$, confirming that at MalNOcta concentration used to prepared Ag-MalNOcta nanoparticles there is micellar aggregates.

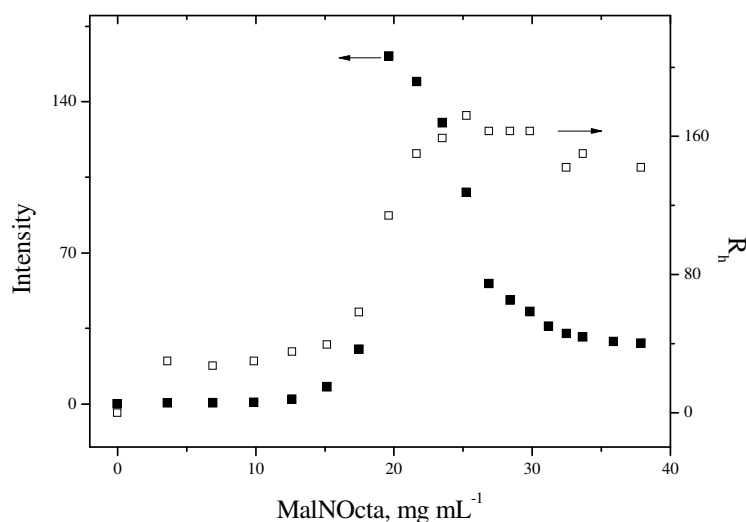


Figure 34. Light scattering intensity and the hydrodynamic radius (R_h) versus MalNOcta concentration.

5.2.3 Catalytic activity of AgNPs stabilized by oligosaccharides based amphiphiles

Although metal glyconanoparticles have been extensively used for many different applications, especially biology,^{117, 145-146} virtually no study has been performed on catalytic activities. Here it is describe the catalytic effects of these new oligosaccharides based nanomaterials on redox reactions and its behaviour in reaction medium mixtures of water/ethanol. The reduction of Nip to Amp by NaBH_4 was used again as a model reaction. Despite this reaction is easily performed in water medium, some intrinsic difficulties arise when a poor water soluble organic compound is used as a substrate. Thereby, solvents obtained from renewable sources, with low environmental hazards and which can to solubilise organic compounds, as ethanol for example, have been preferred.¹⁴⁷ In this sense, in this work was studied the effect of water/ethanol mixtures in the Nip reduction, by fixing the surface area of the metal nanoparticles, normalized to the unit volume of the reaction system (S), and using a 1000-fold excess of NaBH_4 over the concentration of Nip to assure *pseudo*-first-order conditions.

Figure 35 shows the influence of the water/ethanol mixtures in the apparent first-order rate constant (k_{app}). It can be observed that below 25% of water content no product formation was

observed after 2 hours, between 25 and 65% the Nip reduction takes place, but k_{app} values are very low and almost constant, above 65% k_{app} strongly increases until water content reaches 100%. Despite the structural differences between the amphiphile compounds, the same behaviour was observed for all systems.

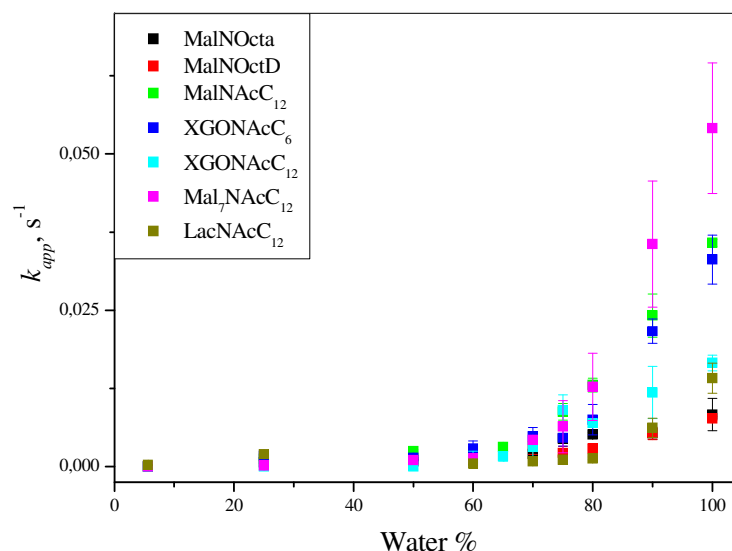


Figure 35. Plots of the apparent rate constant (k_{app}) as a function of water content in the composition mixtures with ethanol; $[Nip] = 8.8 \times 10^{-5} \text{ mol L}^{-1}$, $[NaBH_4] = 8.8 \times 10^{-2} \text{ mol L}^{-1}$ and the total surface area normalized by unit volume ($S = 0.0251 \text{ m}^2 \text{ L}^{-1}$) at 25.0°C .

Since the Ag-Mal₇NAC₁₂ system presented the highest solvent effect, it was selected for further detailed studies. A full set of kinetic data was obtained on the influence of the concentration of all reagents (Nip, Ag-NPs and NaBH₄) on the reaction at 100 and 75% of water content in the composition mixture with ethanol. The effects of the NaBH₄ and Nip concentrations for 75% of water are shown in Figure 36a and in Figure 36b for 100% of water. In a typical set of experiments, while one reactant concentration was varied, the concentration of other reactant (always above the saturation level) and catalyst were kept constant.

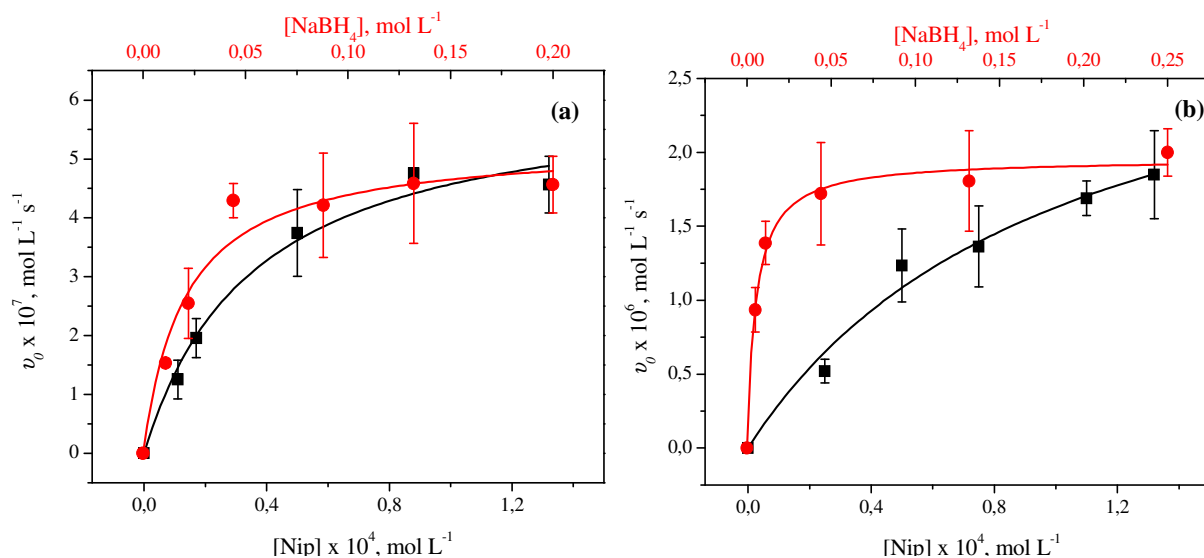


Figure 36. Plots of initial reaction rate (v_0) as function of $[\text{NaBH}_4]$ (red circles, $[\text{Nip}] = 1.32 \times 10^{-4} \text{ mol L}^{-1}$) and $[\text{Nip}]$ (black squares, $[\text{NaBH}_4] = 0.20 \text{ mol L}^{-1}$) for Ag-Mal₇NAC₁₂ glyconanoparticles in A 75% and B 100% of water content in the solvent composition with ethanol. The total surface area normalized by unit volume (S) was set to $0.0251 \text{ m}^2 \text{ L}^{-1}$ for (a) and $0.00791 \text{ m}^2 \text{ L}^{-1}$ for (b), the reaction temperature was set to 25.0°C .

It is observed in the kinetic profiles in Figure 36 that the initial reaction rate increases with the reactants concentration until saturation in both reaction medium, at 75% and 100% content of water. These concentration profiles can be interpreted as the result of *pseudo*-monomolecular surface reactions, as show in Figure 37. Such reaction consideration is possible because the concentrations of the reactants kept constant, Nip (black squares) and NaBH_4 (red circles), were chosen to be always above the saturation level (i.e., zero-order dependence), which means that the surface of the nanoparticles was always saturated by one of the reactants.

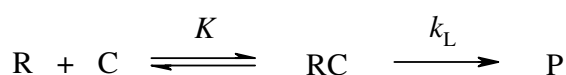


Figure 37. Scheme of the reaction mechanism for monomolecular surface reactions.

This experiment artifice has been recently proposed by our research group⁷⁵ as a way to simplify the data treatment, since the rate equation for bimolecular surface reactions takes in account a large number of variables (Equation 14, considering a homogeneous surface) and the nonlinear fitting procedures generate large standard errors.

$$\text{Equation 14. } v = \frac{k_L S K_{\text{Nip}} [\text{Nip}] K_{\text{BH}_4} [\text{BH}_4]}{(1 + K_{\text{Nip}} [\text{Nip}] + K_{\text{BH}_4} [\text{BH}_4])^2}$$

According to scheme in the Figure 37, the reactant R (BH_4^- at high concentration of Nip or Nip at a high concentration of BH_4^-) interacted with the active sites on the catalyst surface C (Ag-NPs) to form the adsorbed species RC, which underwent reaction to form the final product P (Amp).

At high concentrations of BH_4^- or Nip, the reaction occurred at the surface of Ag-NPs and the reaction rate was dependent on the fraction of catalyst surfaces covered by substrate, as described by the Langmuir model. Therefore, the global reaction law can be expressed by Equation 15:

$$\text{Equation 15. } v = k_L S \theta_R$$

where k_L is the Langmuir rate constant for the formation of the product normalized to S , the surface area of all nanoparticles normalized to the unit volume of the reaction system, and θ_R is the fraction of catalyst surface covered by the reactant, which can be expressed by Equation 16:

$$\text{Equation 16. } \theta_R = \frac{K[R]}{1+K[R]}$$

combining Equation 15 and Equation 16, we can obtain:

$$\text{Equation 17. } v = \frac{k_L S K [R]}{1+K[R]}$$

Applying Equation 17 to the experimental data for the Nip reduction shown in Figure 36, the Langmuir rate constant and the adsorption constants were calculated by means of nonlinear fitting procedures (Table 11).

Table 11 . Rate constants and adsorption constants of Nip and BH_4^- .

System	k_L^a , $\text{mol m}^{-2} \text{s}^{-1}$	$K_{\text{BH}_4^-}^b$, L mol^{-1}	K_{Nip}^b , L mol^{-1}
75% water	$(2.3 \pm 0.2) \times 10^{-5}$	37.3 ± 5.3	$(3.3 \pm 0.3) \times 10^4$
100% water	$(2.8 \pm 0.7) \times 10^{-4}$	135.8 ± 25.0	$(2.4 \pm 0.4) \times 10^4$

^a Langmuir rate constant normalized to total surface area of the nanoparticles per unit of volume. ^b Langmuir adsorption constant.

Although the similar values of K_{Nip} obtained for both solvents systems, the K_{BH_4} in 100% water is $\sim 3.5\times$ higher than in 75% water and $k_L \sim 12\times$ higher. These results indicate that the catalyst surface has been disturbed with the addition of the less polar solvent ethanol. Since it is assumed that the Nip reduction reaction occurs at the metal nanoparticle surface, and the surface tension is an interfacial property, we have explored a possible effect of the surface tension on k_{app} in different water/ethanol mixtures (Figure 38).

It is observed in Figure 38 that the k_{app} substantially increases until $\sim 37 \times 10^{-3} \text{ N m}^{-1}$, which corresponds to the surface tension of 90% of water content in the composition mixture with ethanol (dotted line). Interestingly, a similar behavior has been observed by Yano et al. in the study of adsorption isotherms of surface tension and vapor pressure as a function of molar fraction of different alcohols in water.¹⁴⁸ Yano has shown that the solution has a substantial deviation from ideality, with a discontinuity in surface tension profile, at approximately 10% of ethanol in water. These finding indicated the formation of alcohol monolayer in the surface of the solution.¹⁴⁸ The agreement made by the observations of Yano and the data obtained in our kinetic experiments is consistent with the possibility of ethanol molecules being adsorbed at the nanoparticles surface, in the formation of a monolayer, and competing with the reactants, specially the less surface-active BH_4^- ions, for the nanoparticles surface. This explains the difference in the adsorption constants for BH_4^- and consequently the difference in the Langmuir rate constants (Table 11).

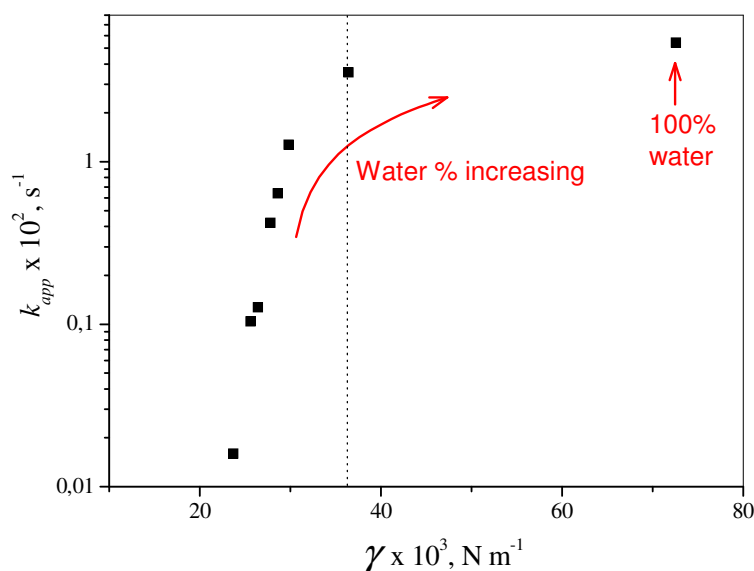


Figure 38. Apparent rate constant (k_{app}) for Nip reduction reaction by NaBH_4 , in the presence of $\text{Ag-Mal}_7\text{NAC}_{12}$ glyconanoparticles, as a function of surface tension γ in different % water content in the solvent composition with ethanol ($S = 0.0251 \text{ m}^2 \text{ L}^{-1}$, $[\text{Nip}] = 8.8 \times 10^{-5} \text{ mol L}^{-1}$ and $[\text{NaBH}_4] = 8.8 \times 10^{-2} \text{ mol L}^{-1}$) at 25.0°C .

Another way to evaluate the metal nanoparticles catalytic activity is the determination of k_1 , that is, the catalytic constant rate normalized to the surface area S per volume unit, as discussed in section 5.1.2. Using zero-order reaction conditions with respect to NaBH_4 , it is possible to apply the Equation 9 to determine the rate constant k_1 from a linear plot of k_{app} as a function of S (Figure 39 for 100% and 75% of water in the presence of Ag-Mal₇NAC₁₂ glyconanoparticles). It can be observed that the rate constant k_{app} is proportional to the total surface area of all metal nanoparticles in both systems; hence, it can be concluded that catalysis indeed takes place on the surface of the nanoparticles.

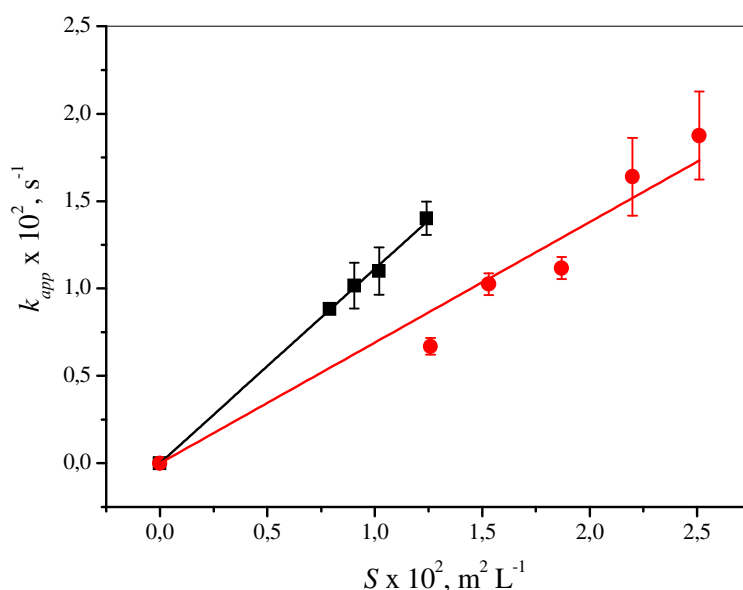


Figure 39. Plots of the apparent rate constant (k_{app}) as a function of the surface area of Ag-NPs normalized to the unit volume of the system (S) for 100% (black squares, $[\text{NaBH}_4] = 0.20 \text{ mol L}^{-1}$, $[\text{Nip}] = 0.75 \times 10^{-4} \text{ mol L}^{-1}$) and for 75% water in the solvent composition with ethanol (red circles, $[\text{NaBH}_4] = 0.20 \text{ mol L}^{-1}$, $[\text{Nip}] = 0.75 \times 10^{-4} \text{ mol L}^{-1}$) at 25.0°C .

The k_1 values determined from the angular coefficient of the plots of Figure 39 were found to be 1.11 ± 0.01 and $0.69 \pm 0.03 \text{ L m}^{-2} \text{ s}^{-1}$ for 100% and 75% of water, respectively. The difference in the magnitudes of k_1 , k_L and K_{BH_4} in the different reaction media clearly shows that the catalytic activity has a major influence from the solvent effect, which in turn seems to be dependent on the structure of the stabilizers. However, it is not possible at this point to quantify how much, if any, of the glyconanoparticle organic framework is responsible for the induction of monolayers formation, on the surface of metal nanoparticle, by the surface-active solvent molecules or if it is related with one of the several possible transport phenomena. Nevertheless, similar to what we have observed for other bulk stabilizers, as polymers^{74-75, 149} for example, the concentration-time profiles did present induction periods, and so, resistance of reactants to diffusion seems to be playing a part in

these catalytic glyconanoparticles systems. It is evident from this work that further studies need to be performed to elucidate the potential role of the stabilizer on these promising catalytic systems.

The Table 12 is an update of Table 6 with the k_I values obtained for the Ag-Mal₇NAC₁₂ system. Despite Ag-Mal₇NAC₁₂ system have lower k_I values than other two systems reported (one of them also develop in this thesis and the other in the same group) the values reported are between the five higher values reported in the literature. As discussed in the section 5.1.2, the comparison and rationalization of the values listed in this kind of table is rather difficult, and attribution of these catalytic effects to other reason than due the high surface area presented by metal nanoparticles is speculation. However, the data in the Table 12 clearly shows that the stabilizer play an important role in the catalysis and little changes in the stabilizer structure (entries 1 and 6) or solvent composition (entries 3 and 4) can cause significant effects in the catalytic constant k_I .

Table 12. Comparison between catalytic activities of silver nanoparticle systems in p-nitrophenol reduction.

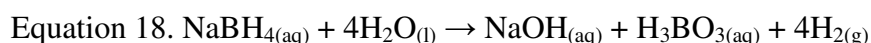
Entry	Stabilizer	Solvent	Temperature	D _m , nm ^b	k _I , (s ⁻¹ m ⁻² L) ^c
1	F1-LPEI ⁷⁵	Water	15.0°C	34 ± 9	1.66
2	Dextran T500 ^a	Water	25.0°C	6,1 ± 1.3	1.41
3	Mal ₇ NAC ₁₂ ^a	Water	25.0°C	3.16 ± 0.84	1.11
4	TiO ₂ ⁷⁷	Water	21.0°C	3	0.78
5	Mal ₇ NAC ₁₂ ^a	Water/ Ethanol ^d	25.0°C	3.16 ± 0.84	0.69
6	Derivatized PEI ¹⁰	Water	25.0°C	24.5 ± 4.1	0.57
7	F12-LPEI ⁷⁵	Water	25.0°C	30 ± 10	0.37
8	Carboxymethyl chitosan microgel ¹³⁶	Water	25.0°C	3.45 ± 0.65	0.196
9	Aminosilicate ¹³⁷	Water	25.0°C	~3,6	0.188
10	Quitosan ⁵⁸	Water	25.0°C	~3	0.15
11	Carboxymethyl chitosan microgel ¹³⁶	Water	25.0°C	2.81 ± 0.62	0.124
12	Anionic polyelectrolyte brush ¹³⁸	Water	25.0°C	3.0 ± 1.2	0.078

^a This work. ^b Diameter of metal nanoparticles. ^c Rate constant normalized to surface area of metal nanoparticles per volume unit. ^d Water 75% (v/v).

5.2.4 AgNPs stabilized by oligosaccharides based amphiphiles evaluation as lectins sensors

Metal glyconanoparticles have been applied in many different applications as for example HIV vaccine,¹⁵⁰ X-ray contrast agents,¹⁵¹ ligand screening and diagnostics.¹⁴⁵⁻¹⁴⁶ Normally, these metal glyconanoparticles are prepared by some of the many variations of Brust's method,¹⁵² i.e. the capping agent is presented in a carbohydrate-spacer-sulphur configuration and the metal nanoparticle synthesized in a two-step reaction. The success of this methodology is based on the strong interaction of sulphur atoms with the metal nanoparticles surface, especially gold, increasing its stability.

Despite the carboxylate anion interaction is less strong than a sulphur interaction, the silver glyconanoparticles prepared in this work were tested for lectins detection. Figure 40 shows the effect of lectin Concanavalin A (Con A) in the surface Plasmon resonance (SPR) band of Ag-Mal₇NAC₁₂. The Con A was chosen because it is a well characterized and commercially available lectin extracted from the jack-bean, in a homotetramer form and the molecular basis of interaction with sugars mannose and glucose are well know.¹⁵³ As can be observed in the Figure 40, when the Ag-Mal₇NAC₁₂ nanoparticles were dispersed in the saline phosphate buffer the SPR band was very disturbed, probably due to AgNPs precipitation. When Con A is in the system, however, the SPR is less affected and above a certain concentration no changes in the AgNPs spectra were observed. The precipitation of the AgNPs observed in absence of Con A is probably related with the pH changes. Since to reduce silver ions, in the Ag-Mal₇NAC₁₂ preparation, NaBH₄ was used in excess, this excess turns the pH of the medium basic (pH > 9) (Equation 18). Considering that the pK_a of Mal₇NAC₁₂ is near to the dodecanoic acid pK_a (7.5),¹⁵⁴ under such conditions all Mal₇NAC₁₂ molecules are ionized and a partition of Mal₇NAC₁₂ molecules between the nanoparticle surface and the solution is established. Dispersing Ag-Mal₇NAC₁₂ nanoparticles in the saline phosphate buffer, with pH 7.2, an equilibrium between the ionized and nonionized species is formed, decreasing the proportion of Mal₇NAC₁₂ in the AgNP surface. In this sense, the Con A addition prevents the Mal₇NAC₁₂ protonation probably by capping Ag-Mal₇NAC₁₂ glyconanoparticles, hampering the Mal₇NAC₁₂ desorption from the AgNP surface.



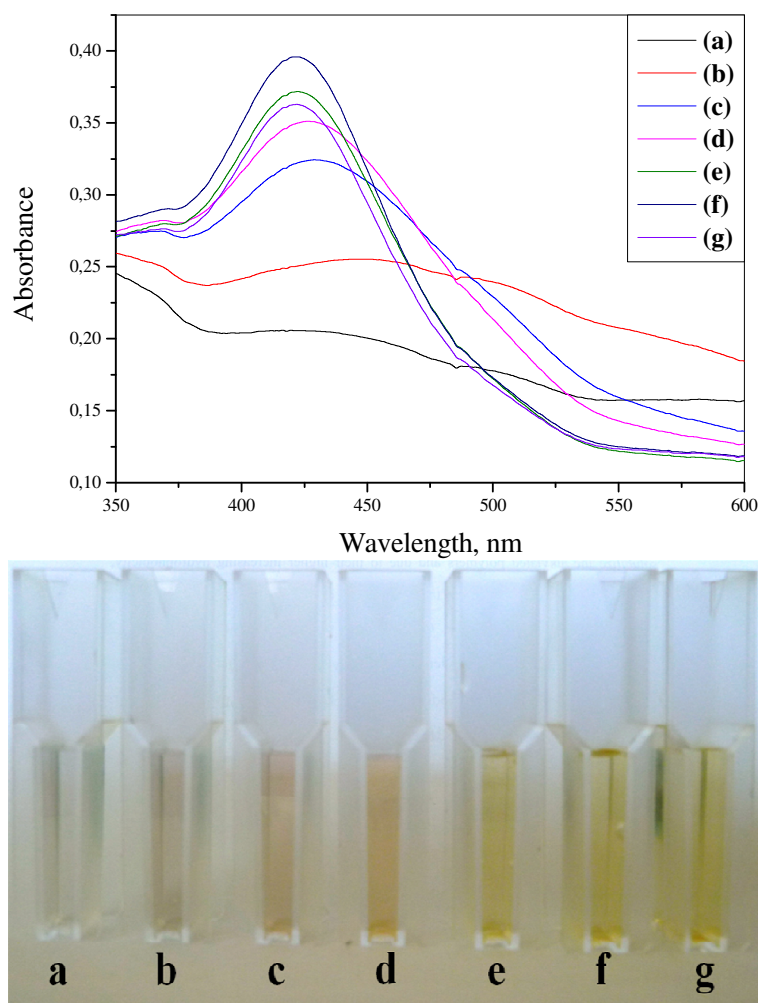


Figure 40. Absorption spectra of Ag-Mal₇NAC₁₂ ($S = 0.678 \text{ m}^2 \text{ L}^{-1}$) (up) and digital photography (down), with $a = 0$; $b = 0.0032$; $c = 0.0063$; $d = 0.0095$; $e = 0.0188$; $f = 0.0366$ and $g = 0.0701 \text{ mg mL}^{-1}$ of Con A, in phosphate buffer $\text{pH} = 7.2$ containing $150 \times 10^{-3} \text{ mol L}^{-1}$ of NaCl, $0.1 \times 10^{-3} \text{ mol L}^{-1}$ of CaCl_2 and MnCl_2 $0.1 \times 10^{-3} \text{ mol L}^{-1}$.

It was observed time dependence in Ag-Mal₇NAC₁₂ precipitation in saline phosphate buffer and Ag-Mal₇NAC₁₂ interaction with Con A. For better reproducibility in these experiments, the Ag-Mal₇NAC₁₂ SPR band was followed for 150 minutes (Figure 41). It is observed in Figure 41 that absorbance strongly decreases in the first minutes and after about sixty minutes, no significant change was observed. Similar profiles were obtained in presence of Con A, so all absorbance measures were realized after sixty minutes of Ag-Mal₇NAC₁₂/Con A mixing.

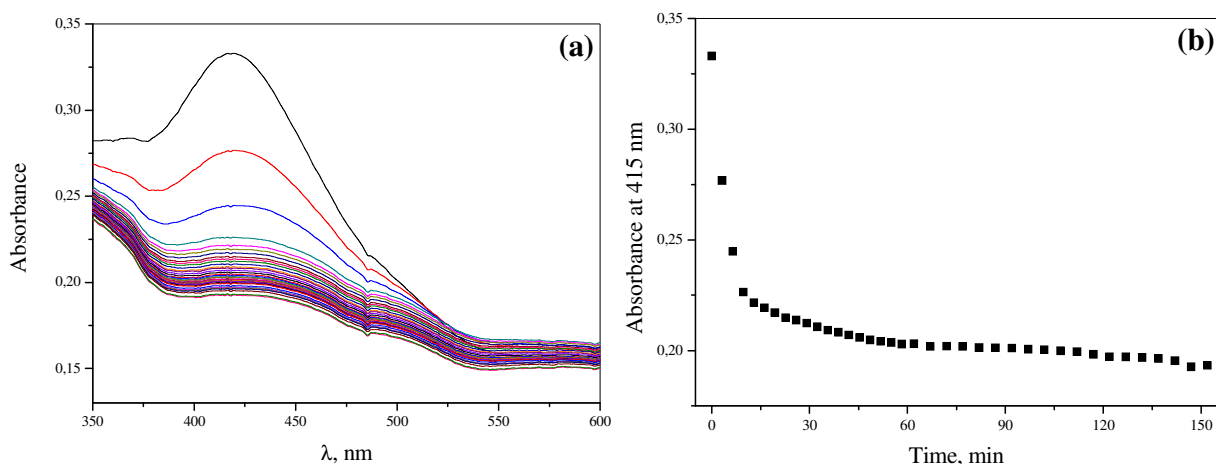


Figure 41. UV-vis spectral dependence of Ag-Mal₇NAC₁₂ with time (a) and absorbance at 415 nm vs. time (b). In phosphate buffer pH = 7.2 containing 0.150 mol L⁻¹ of NaCl, 0.1 × 10⁻³ mol L⁻¹ of CaCl₂ and MnCl₂ 0.1 × 10⁻³ mol L⁻¹ at 25.0 °C.

After the first experiments in cuvette scale, it was opted to use a microplate scale and all UV-vis experiments from this point were acquired in a microplate spectrophotometer. Figure 42 shows the linear relationship between Ag-Mal₇NAC₁₂ absorbance and Con A concentration, with a determination coefficient (R^2) of 0.98. To confirm the specificity in the interaction with Con A, experiments with peanut agglutinin lectin (PNA) were performed in the same concentration range used in Con A experiments. The PNA is a lectin extracted from peanuts which interacts specifically with galactose and lactose sugars. As expected, PNA concentration effect was not observed (the Ag-Mal₇NAC₁₂ precipitates in all PNA concentrations), demonstrating that the changes in Con A profile are due specific interaction with Ag-Mal₇NAC₁₂ nanoparticles. The detection limit calculated from Figure 42 for Con A was 0.66 μg ml⁻¹. Compared to other systems in the literature (Table 13), this value is lower than some colorimetric and microgravimetric methodologies without enhancement procediments. On the other hand, it is not much higher than the values obtained in more complex methodologies, being a good alternative for Con A detection.

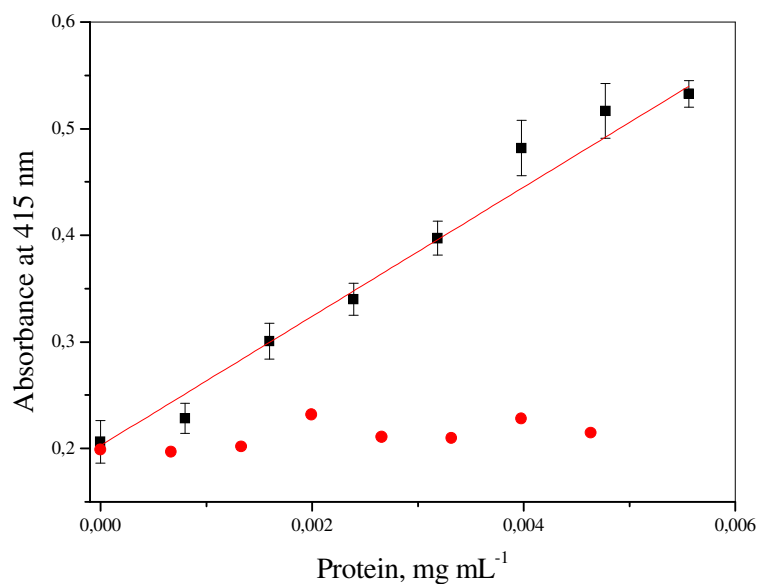


Figure 42. Absorbance Ag-Mal₇NAC₁₂ at 415 nm vs. Con A (■) and PNA (●) concentration. In phosphate buffer pH = 7.2 containing 0.150 mol L⁻¹ of NaCl, 0.1 x 10⁻³ mol L⁻¹ of CaCl₂ and MnCl₂ 0.1 x 10⁻³ mol L⁻¹ at 25.0 °C.

Table 13. Detection limits comparison for Con A determination with various lectin biosensing methods.

Entry	Lectin biosensing method	Detection limit (μg mL ⁻¹)
1	Colorimetric/mannose bilayers on nano-Au glass slide ¹⁵⁵	0.010
2	Microgravimetric/mannose-Au NPs induced signal enhancement ¹⁵⁶	0.013
3	Electrochemical/mannose-Au NPs and silver enhancement ²¹	0.070
4	Colorimetric/ AuNPs UV-vis SPR band ¹¹⁷	0.64
5	Colorimetric/ Ag-Mal ₇ NAC ₁₂ UV-vis SPR band (this work)	0.66
6	Colorimetric/Con A-induced mannose-Ag NPs aggregation ¹¹⁸	4.1
7	Microgravimetric/no signal enhancement ¹⁵⁷	9.2
8	Colorimetric/Con A-induced mannose-Au NPs aggregation ¹⁵⁸	10.3

As the XGO have some galactose residues, the Ag-XGONAcC₁₂ was tested as possible sensor to PNA lectin. Figure 43 shows the effects of PNA and Con A in the Ag-XGONAcC₁₂ nanoparticles absorbance. A strong effect was observed, but unfortunately, the interaction was not specific in this case, as demonstrated by the profile with Con A. In the same way, experiments were realized with Ag-LacNAcC₁₂ nanoparticles (Figure 44), but again no specific interaction was observed between the nanoparticles and the different lectins. Obviously, the protein interaction in both cases is not mediated by the sugar recognition moiety. It is accepted that amphiphiles can interact with proteins forming structures in solution by cooperative binding,¹⁵⁹⁻¹⁶⁰ and possibly, Ag-XGONAcC₁₂ and Ag-LacNAcC₁₂ systems are interacting with the Con A by this way.

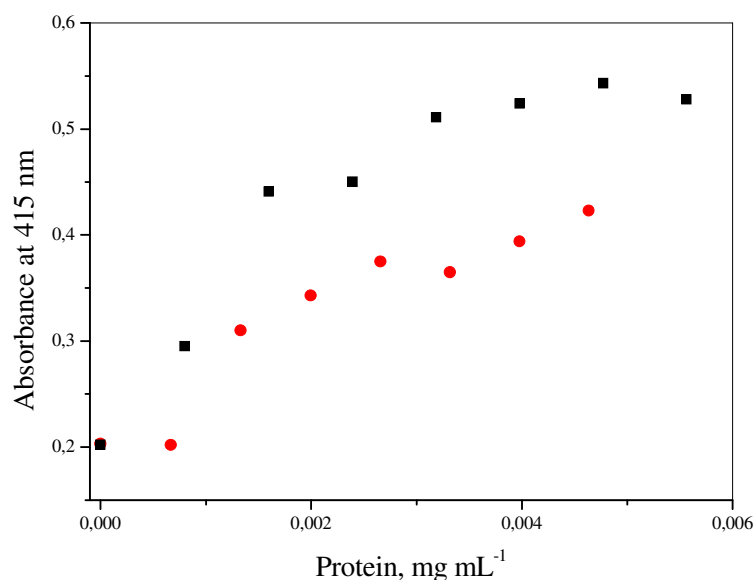


Figure 43. Absorbance Ag-XGONAcC₁₂ at 415 nm vs. Con A (■) and PNA (●) concentration. In phosphate buffer pH = 7.2 containing 0.150 mol L⁻¹ of NaCl, 0.1 x 10⁻³ mol L⁻¹ of CaCl₂ and MnCl₂ 0.1 x 10⁻³ mol L⁻¹ at 25.0 °C.

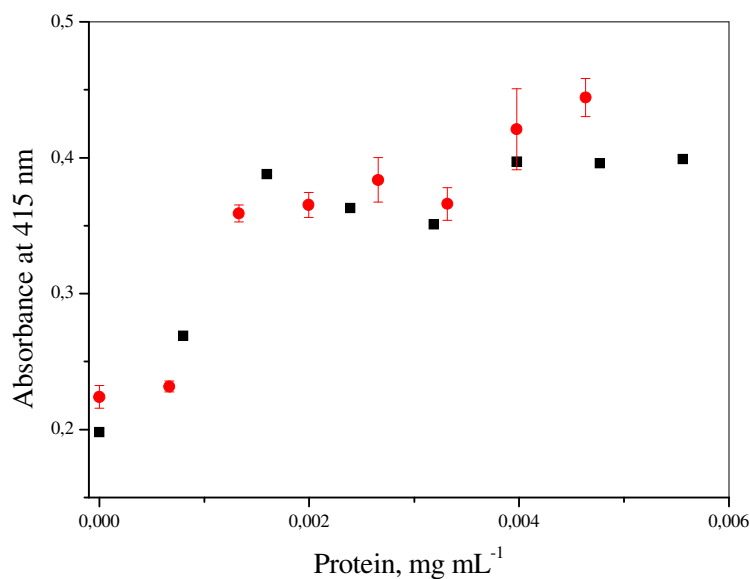


Figure 44. Absorbance Ag-LacNAcC₁₂ at 415 nm vs. Con A (■) and PNA (●) concentration. In phosphate buffer pH = 7.2 containing 0.150 mol L⁻¹ of NaCl, 0.1 × 10⁻³ mol L⁻¹ of CaCl₂ and MnCl₂ 0.1 × 10⁻³ mol L⁻¹ at 25.0 °C.

In this sense, if Ag-XGONAcC₁₂ and Ag-LacNAcC₁₂ interact cooperatively (non specifically) with Con A, why this behaviour is not observed with Ag-Mal₇NAC₁₂ system? Wang et al.¹¹⁷ studied systematically the influence of nanoparticle size, spacer length, ligand size, and density on the binding affinity of Con A with gold glyconanoparticles. Their results showed that the lectin binding affinity is profoundly affected by how the ligands are displayed in the gold nanoparticle (AuNP) surface, and the best results were obtained with bigger spacers between the sugar and AuNP surface and smaller sugar density at glyconanoparticle surface. Despite Mal₇NAC₁₂ amphiphile have the same hydrophobic structure of XGONAcC₁₂ and LacNAcC₁₂, the longer Mal₇NAC₁₂ amphiphilic structure is more likely to bond with its specific lectin, Con A. On the other hand, the short lactose and the branched XGO show non specific bond with Con A due their structures.

6 Conclusions

With the goal to develop silver nanoparticles stabilized by sugar based compound following some precepts of the green chemistry, in this work were obtained silver nanoparticles which showed very good catalytic activity towards *p*-nitrophenol reduction and good potential for lectin's sensors.

Nine different new compounds were synthesized and characterized in this work. All compounds have in its structure a functional group that can be used for additional modifications in the future, as for example to link a reducing agent, a chelant or to a resin. They are divided in two different types based in this modifiable group (carboxylic acid or alkyne). The yields obtained in the preparation of these compounds were affected by the balance hydrophilic/hydrophobic in the structure; the more hydrophilic compounds were obtained in better yields.

The multivariate analysis was successfully used in the determination of the best conditions for preparation of AgNPs for each stabilizer. All stable AgNPs systems were tested as catalyst in the reduction reaction of Nip, using NaBH_4 as reducing agent. The best catalytic activities were obtained for AgNPs-dextran and Ag-Mal₇NAC₁₂ systems and for both systems was performed a complete kinetic study. By the quasi-homogeneous treatment, the rate constants normalized by the surface area of AgNPs-dextran and Ag-Mal₇NAC₁₂ by volume unity (k_l) were 1.41 and 1.11 s⁻¹ m⁻² L, respectively. These values are between the five highest reported in the literature. Additionally the solvent effect in the Nip reduction was evaluated carrying the reaction in mixtures of water and ethanol. A complete kinetic study was done at 100% and 75% of water for Ag-Mal₇NAC₁₂ based in Langmuir-Hinshelwood mechanism, which considers that all reactants must be adsorbed in the catalyst surface for the reaction occurs. Applying a *pseudo*-monomolecular surface reaction as an experimental artifice, the obtained kinetic data were treated according to the Langmuir model, which combined with water/ethanol surface tension observations revealed that addition of ethanol inhibit the reaction, most probably by competing with BH_4^- ions for the nanoparticles surface, with the formation of a solvent monolayer.

Three different systems (Ag-Mal₇NAC₁₂, Ag-XGONAC₁₂ and Ag-LacNAC₁₂) were tested as sensor for lectin detection. Only Ag-Mal₇NAC₁₂ nanoparticles showed specific interaction with the respective lectin. The success in this system was correlated with its structure due the bigger spacing between the AgNP surface and the Ag-Mal₇NAC₁₂ surface.

7 Bibliography

1. N. Toshima, ed., *Metal nanoparticles for catalysis*. In: Liz-Marzán, et al. *Nanoscale Materials*, USA, 2007.
2. X. Jiang, Q. Zeng and A. Yu, *Nanotechnology*, 2006, **17**, 4929–4935.
3. P. V. Kamat, *The Journal of Physical Chemistry B*, 2002, **106**, 7729–7744.
4. S. Sun, C. B. Murray, D. Weller, L. Folks and A. Moser, *Science*, 2000, **287**, 1989–1992.
5. S. R. Nicewarner-Peña, R. G. Freeman, B. D. Reiss, L. He, D. J. Peña, I. D. Walton, R. Cromer, C. D. Keating and M. J. Natan, *Science*, 2001, **294**, 137–141.
6. L. A. Dick, A. D. Mcfarland, C. L. Haynes and R. P. Van Duyne, *The Journal of Physical Chemistry B*, 2001, **106**, 852–860.
7. D. Astruc, in *Nanoparticles and Catalysis*, ed. D. Astruc, Wiley Interscience, 2008, pp. 1–48.
8. J. Virkutyte and R. S. Varma, *Chemical Science*, 2010, **2**, 837.
9. C.-J. Jia and F. Schuth, *Physical Chemistry Chemical Physics*, 2011, **13**, 2457–2487.
10. A. M. Signori, K. d. O. Santos, R. Eising, B. L. Albuquerque, F. C. Giacomelli and J. B. Domingos, *Langmuir*, 2010, **26**, 17772 - 17779.
11. H. Bönemann and R. M. Richards, *European Journal of Inorganic Chemistry*, 2001, **10**, 2455 - 2480.
12. J. Dupont and J. D. Scholten, *Chemical Society Reviews*, 2010, **39**, 1780–1804.
13. E. J. Lenardão, R. A. Freitag, M. J. Dabdoub, A. C. F. Batista and C. d. C. Silveira, *Química Nova*, 2003, **26**, 123–129.
14. N. Nishida, H. Yao, T. Ueda, A. Sasaki and K. Kimura, *Chemistry of Materials*, 2007, **19**, 2831–2841.
15. J. F. Ciebien, R. T. Clay, B. H. Sohn and R. E. Cohen, *New Journal of Chemistry*, 1998, **22**, 685–691.
16. J. D. Aiken and R. G. Finke, *J. Mol. Catal. A: Chem.*, 1999, **145**, 1–44.
17. A. G. Barrientos, J. M. d. l. Fuente, M. Jiménez, D. Solís, F. J. Cañada, M. Martín-Lomas and S. Penadés, *Carbohydrate Research*, 2009, **344**, 1474 - 1478.
18. G. Bauer, F. Pittner and T. Schalkhammer, *Mikrochimica Acta*, 1999, **131**, 107 - 114.
19. S. Campuzano and J. Wang, *Electroanalysis*, 2011, **23**, 1289 - 1300.
20. Y. Ma, N. Li, C. Yang and X. Yang, *Anal Bioanal Chem*, 2005, **382**, 1044 - 1048.
21. I.-H. Min, L. Choi, K.-S. Ahn, B. K. Kim, B. Y. Lee, K. S. Kim, H. N. Choi and W.-Y. Lee, *Biosensors and Bioelectronics*, 2010, **26**, 1326 - 1331.
22. K. Akamatsu and S. Deki, *Nanostructured Materials*, 1997, **8**, 1121–1129.
23. G. Palasantzas, S. A. Koch, T. Vystavel and J. T. M. De Hosson, *Journal of Alloys and Compounds*, 2008, **449**, 237–241.
24. N. Toshima, *Nanoscale Materials*, Kluwer Academic Publishers, New York, 2003.
25. O. Schubert, Optical properties of Plasmonic Nano-Particles www.os-cs.de/.
26. V. Bastys, I. Pastoriza-Santos, B. Rodriguez-Gonzalez, R. Vaisnoras and L. M. Liz-Marzan, *Advanced Functional Materials*, 2006, **16**, 766 - 773.
27. A. Shipway and I. Willner, *Chemical Communications*, 2001, **20**, 2035 - 2045.
28. C. N. R. Rao, G. U. Kulkarni, P. J. Thomas and P. P. Edwards, *Chemistry European Journal*, 2002, **8**, 28 - 35.
29. D. V. Leff, P. C. Ohara, J. R. Heath and W. M. Gelbart, *The Journal of Physical Chemistry*, 1995, **99**, 7036 - 7041.
30. S. Link and M. A. El-Sayed, *The Journal of Physical Chemistry B*, 1999, **103**, 4212 - 4217.
31. W. J. Parak, D. Gerion, T. Pellegrino, D. Zanchet, C. Micheel, S. C. Williams, R. Boudreau, M. A. L. Gros, C. A. Larabell and P. Alivisatos, *Nanotechnology*, 2003, **14**, R15 - R17.

32. A. N. Shipway, E. Katz and I. Willner, *European Journal of Chemical Physics and Physical Chemistry*, 2000, **1**, 18 - 52.
33. M. Faraday, *Philosophical Transactions of the Royal Society*, 1857, **147**, 145 - 181.
34. J. Turkevich, P. C. Stevenson and J. Hillier, *Discuss. Faraday Soc.*, 1951, 55-75.
35. Y. Mei, G. Sharma, Y. Lu, M. Ballauff, M. Drechsler, T. Irrgang and R. Kempe, *Langmuir*, 2005, **21**, 12229.
36. A. Panacek, L. Kvítek, R. Prucek, M. Kolar, R. Vecerova, N. Pizurova, V. K. Sharma, T. j. Nevecna and R. Zboril†, *J. Phys. Chem. B*, 2006, **110**, 16248 - 16253.
37. D. V. Goia and E. Matijevic, *New Journal of Chemistry*, 1998, 1203-1215.
38. Y.-S. Shon and H. Choo, *Comptes Rendus Chimie*, 2003, **6**, 1009.
39. D. M. Vriezema, M. C. Aragone`s, J. A. A. W. Elemans, J. J. L. M. Cornelissen, A. E. Rowan and R. J. M. Nolte, *Chemical Reviews*, 2005, **2005**, 1445 - 1489.
40. G. Li, Y. Luo and H. Tan, *Journal of Solid State Chemistry*, 2005, **178**, 1038.
41. J. Z. Zhang and C. Noguez, *Plasmonics*, 2008, **3**, 127-150.
42. K. Holmberg, B. Jonsson, B. Kronberg and B. Lindman, *Surfactants and Polymers in Aqueous Solution*, John Wiley & Sons Ltda, Chichester, 2002.
43. T. K. Lindhorst, *Structure of saccharides, essentials of carbohydrate chemistry and biochemistry*, Wiley-VHC, 2007.
44. Y. Saito, J. J. Wang, D. N. Batchelder and D. A. Smith, *Langmuir*, 2003, **19**, 6857-6861.
45. L. Kvítek, R. Prucek, A. Panáček, R. Novotny, J. Hrbáča and R. Zboril, *Journal of Materials Chemistry*, 2005, **15**, 1099 - 1105.
46. C. V. Ramana, K. A. Durugkar, V. G. Puranik, S. B. Narute and B. L. V. Prasad, *Tetrahedron Letters*, 2008, **49**, 6227 - 6230.
47. S. Singh, P. Patel, S. Jaiswal, A. A. Prabhune, C. V. Ramana and B. L. V. Prasad, *New Journal of Chemistry*, 2009, **33**, 646 - 652.
48. S. Singh, V. D'Britto, A. A. Prabhune, C. V. Ramana, A. Dhawan and B. L. V. Prasad, *New Journal of Chemistry*, 2009, **34**, 294 - 301.
49. M. d. L. C. d. Silva, P. F. Martinez, N. L. Izeli, I. R. Silva, A. F. D. Vasconcelos, M. d. S. Cardoso, R. M. Stelutti, E. C. Giese and A. d. M. Barbosa, *Química Nova*, 2006, **29**, 85 - 92.
50. L. Yang and L. M. Zhang, *Carbohydrate Polymers*, 2009, **76**, 349 - 361.
51. W. Burchard, in *Soft Matter Characterization*, eds. R. Borsali and R. Pecora, NewYork, 2008.
52. K. Benaissi, L. Johnson, D. A. Walsh and W. Thielemans, *Green Chemistry*, 2010, **12**, 220 - 222.
53. V. L. Budarin, J. H. Clark, R. Luque, D. J. Macquarrie and R. J. White, *Green Chemistry*, 2008, **10**, 382 - 387.
54. J. Cai, S. Kimura, M. Wada and S. Kuga, *Biomacromolecules*, 2009, **10**, 87 - 94.
55. D. Wei, Y. Ye, X. Jia, C. Yuan and W. Qian, *Carbohydrate Research*, 2010, **345**, 74 - 81.
56. I.-W. Shim, W.-T. Noh, J. Kwon, J. Y. Cho, K.-S. Kim and D. H. Kang, *Bull. Korean Chem. Soc*, 2002, **23**, 563 - 566.
57. S. Li, Y. Zhang, X. Xu and L. Zhang, *Biomacromolecules*, 2011, **12**, 2864-2871.
58. A. Murugadoss and A. Chattopadhyay, *Nanotechnology*, 2008, **19**, 015603.
59. C. Tabor, R. Narayanan and M. A. El-Sayed, in *Model Systems in Catalysis*, ed. R. Rioux, Springer, New York, 2009, pp. 395 - 414.
60. H. Bonnemann and K. S. Nagabhushana, in *Metal Nanoclusters in Catalysis and Materials Science*, eds. B. Corain, G. Schidt and N. Toshima, Elsevier, Oxford, UK, 2008, pp. 21-48.
61. G. Rothenberg, *Catalysis - Concepts and Green Applications*, WILEY-VCH Verlag, Weinheim, 2008.
62. S. Panigrahi, S. Basu, S. Praharaj, S. Pande, S. Jana, A. Pal, S. K. Ghosh and T. Pal, *J. Phys. Chem. C*, 2007, **111**, 4596-4605.
63. H. Tsunoyama, H. Sakurai and T. Tsukuda, *Chemical Physics Letters*, 2006, **429**, 528-532.

-
64. A. P. Umpierre, G. Machado, G. H. Fecher, J. Morais and J. Dupont, *Advanced Synthesis & Catalysis*, 2005, **347**, 1404-1412.
65. N. Pradhan, A. Pal and T. Pal, *Colloids Surf., A*, 2002, **196**, 247.
66. Y. L. Hsin, K. C. Hwang and C.-T. Yeh, *Journal of the American Chemical Society*, 2007, **129**, 9999-10010.
67. M. M. Ramírez-Corredores, T. Romero, D. Djaouadi, Z. Hernández and J. Guerra, *Industrial & Engineering Chemistry Research*, 2002, **41**, 5385-5392.
68. N. R. Shiju and V. V. Gulians, *Applied Catalysis A: General*, 2009, **356**, 1-17.
69. Y.-C. Chang and D.-H. Chen, *Journal of Hazardous Materials*, 2009, **165**, 664.
70. S. Harish, J. Mathiyarasu and K. L. N. Phani, *Catalysis Letters*, 2009, **128**, 197-202.
71. M. Ahmaruzzaman and S. L. Gayatri, *Journal of Chemical & Engineering Data*, 2010, **55**, 4614-4623.
72. M. J. Vaidya, S. M. Kulkarni and R. V. Chaudhari, *Organic Process Research & Development*, 2003, **7**, 202-208.
73. T. Swathi and G. Buvaeswari, *Materials Letters*, 2008, **62**, 3900-3902.
74. R. Eising, A. M. Signori, S. b. Fort and J. B. Domingos, *Langmuir*, 2011, **27**, 11860-11866.
75. K. d. O. Santos, W. C. Elias, A. M. Signori, F. C. Giacomelli, H. Yang and J. B. Domingos, *J. Phys. Chem. C*, 2012, **116**, 4594-4604.
76. K. Esumi, R. Isono and T. Yoshimura, *Langmuir*, 2004, **20**, 237-243.
77. H. Zhang, X. Li and G. Chen, *Journal of Materials Chemistry*, 2009, **19**, 8223-8231.
78. J. Zeng, Q. Zhang, J. Chen and Y. Xia, *Nano Letters*, 2009, **10**, 30-35.
79. S. Saha, A. Pal, S. Kundu, S. Basu and T. Pal, *Langmuir*, 2010, **26**, 2885-2893.
80. Y. Khalavka, J. Becker and C. Sönnichsen, *Journal of the American Chemical Society*, 2009, **131**, 1871-1875.
81. S. Wunder, F. Polzer, Y. Lu, Y. Mei and M. Ballauff, *J. Phys. Chem. C*, 2010, **114**, 8814-8820.
82. A. Frattini, N. Pellegri, D. Nicastro and O. d. Sanctis, *Materials Chemistry and Physics*, 2005, **94**, 148-152.
83. I. Sondi and B. Salopek-Sondi, *Journal of Colloid and Interface Science*, 2004, **275**, 177-182.
84. J. R. Morones, J. L. Elechiguerra, A. Camacho, K. Holt, J. B. Kouri, J. T. Ramírez and M. J. Yacaman, *Nanotechnology*, 2005, **16**, 2346-2353.
85. E. Ülkür, O. Oncul, H. Karagoz, E. Yeniz and B. Çeliköz, *Burns*, 2005, **31**, 874-877.
86. V. Alt, T. Bechert, P. Steinrücke, M. Wagener, P. Seidel, E. Dingeldein, E. Domann and R. Schnettler, *Biomaterials*, 2004, **25**, 4383-4391.
87. G. Gosheger, J. Hardes, H. Ahrens, A. Streitburger, H. Buerger, M. Erren, A. Gunsel, F. H. Kemper, W. Winkelmann and C. von Eiff, *Biomaterials*, 2004, **25**, 5547-5556.
88. M. E. Rupp, T. Fitzgerald, N. Marion, V. Helget, S. Puumala, J. R. Anderson and P. D. Fey, *American Journal of Infection Control*, 2004, **32**, 445-450.
89. U. Samuel and J. P. Guggenbichler, *International Journal of Antimicrobial Agents*, 2004, **23**, Supplement 1, 75-78.
90. M. Bosetti, A. Massè, E. Tobin and M. Cannas, *Biomaterials*, 2002, **23**, 887-892.
91. H. J. Lee and S. H. Jeong, *TEXTILE RESEARCH JOURNAL*, **75**, 551-556.
92. T. Yuranova, A. G. Rincon, A. Bozzi, S. Parra, C. Pulgarin, P. Albers and J. Kiwi, *Journal of Photochemistry and Photobiology A: Chemistry*, 2003, **161**, 27-34.
93. W.-L. Chou, D.-G. Yu and M.-C. Yang, *Polymers for Advanced Technologies*, 2005, **16**, 600-607.
94. R. W.-Y. Sun, R. Chen, N. P. Y. Chung, C.-M. Ho, C.-L. S. Lin and C.-M. Che, *Chemical Communications*, 2005, 5059-5061.
95. Y. Shiraishi and N. Toshima, *Journal of Molecular Catalysis A: Chemical*, 1999, **141**, 187-192.

96. Y. Shiraishi and N. Toshima, *Colloids and Surfaces A: Physicochemical and Engineering Aspects*, 2000, **169**, 59-66.
97. E. Antolini and E. R. Gonzalez, *Journal of Power Sources*, 2010, **195**, 3431-3450.
98. K. Okajima, K. Nabekura, T. Kondoh and M. Sudoh, *Journal of The Electrochemical Society*, 2005, **152**, D117-D120.
99. C. Reichardt and T. Welton, *Solvents and Solvent Effects in Organic Chemistry*, Wiley-VCH Verlag GmbH & Co. KGaA, 2010.
100. M. H. Abraham, P. A. Grellier, J.-L. M. Abboud, R. M. Doherty and R. W. Taft, *Canadian Journal of Chemistry*, 1988, **66**.
101. L. Gilbert and C. Mercier, in *Studies in Surface Science and Catalysis*, eds. J. B. J. B. C. B. D. D. G. P. M. Guisnet and C. Montassier, Elsevier, 1993, vol. Volume 78, pp. 51-66.
102. S. Mukherjee and M. A. Vannice, *Journal of Catalysis*, 2006, **243**, 108-130.
103. S. Gómez-Quero, E. Díaz, F. Cárdenas-Lizana and M. A. Keane, *Chemical Engineering Science*, 2010, **65**, 3786-3797.
104. B. Hu, R. P. Fishwick, A. W. Pacek, J. M. Winterbottom, J. Wood, E. H. Stitt and A. W. Nienow, *Chemical Engineering Science*, 2007, **62**, 5392-5396.
105. B. S. Akpa, C. D'Agostino, L. F. Gladden, K. Hindle, H. Manyar, J. McGregor, R. Li, M. Neurock, N. Sinha, E. H. Stitt, D. Weber, J. A. Zeitler and D. W. Rooney, *Journal of Catalysis*, 2012, **289**, 30-41.
106. J. Masson, P. Cividino and J. Court, *Applied Catalysis A: General*, 1997, **161**, 191-197.
107. R. A. Rajadhyaksha and S. L. Karwa, *Chemical Engineering Science*, 1986, **41**, 1765-1770.
108. J. Wang, *Nucleic Acids Research*, 2000, **28**, 3011-3016.
109. G. Doria, J. Conde, B. Veigas, L. Giestas, C. Almeida, M. Assunção, J. Rosa and P. V. Baptista, *Sensors*, 2012, **12**, 1657-1687.
110. M. Vijayan and N. Chandra, *Current Opinion in Structural Biology*, 1999, **9**, 707-714.
111. R. Loris, *Biochimica et Biophysica Acta (BBA) - General Subjects*, 2002, **1572**, 198-208.
112. G. A. Tavares, I. Caracelli, R. Burger, M. T. S. Correia, L. C. B. B. Coelho and G. Oliva, *Acta Crystallographica Section D*, 1996, **52**, 1046-1047.
113. H. Lis and N. Sharon, *Chemical Reviews*, 1998, **98**, 637-674.
114. P. D. Bank, 2013.
115. A. E. Smith and A. Helenius, *Science*, 2004, **304**, 237-242.
116. Y. Koshi, E. Nakata, M. Miyagawa, S. Tsukiji, T. Ogawa and I. Hamachi, *Journal of the American Chemical Society*, 2007, **130**, 245-251.
117. X. Wang, O. Ramström and M. Yan, *Analytical Chemistry*, 2010, **82**, 9082-9089.
118. C. L. Schofield, A. H. Haines, R. A. Field and D. A. Russell, *Langmuir*, 2006, **22**, 6707-6711.
119. E. Farkas, L. Jánosy, J. Harangi, L. Kandra and A. Lipták, *Carbohydrate Research*, 1997, **303**, 407-415.
120. J. P. Simon, S. Arnaud, F. Bley, J. F. Berar, B. Caillot, V. Comparat, E. Geissler, A. d. Geyer, P. Jeantey, F. Livet and H. Okuda, *Journal of Applied Crystallography*, 1997, **30**, 900-904.
121. L. P. Cavalcanti, I. L. Torriani, T. S. Plivelic, C. L. P. Oliveira, G. Kellermann and R. Neuenschwander, *Rev. Sci. Instrum.*, 2004, **75**, 4541-4546.
122. J. Kohlbrecher, *Software package SASfit for fitting small-angle scattering curves*, 2010, URL: <http://kur.web.psi.ch/sans1/SANSSoft/sasfit.html>.
123. M. Reza, *Journal of Controlled Release*, 2000, **69**, 1-25.
124. R. B. Grubbs, *Polym. Rev. (Philadelphia, PA, U. S.)*, 2007, **47**, 197-215.
125. J. P. Wilcoxon and B. L. Abrams, *Chemical Society Reviews*, 2006, **35**, 1162-1194.
126. P. K. Jain, X. Huang, I. H. El-Sayed and M. A. El-Sayed, *Accounts of Chemical Research*, 2008.
127. S. K. Ghosh, M. Mandal, S. Kundu, S. Nath and T. Pal, *Appl. Catal., A*, 2004, **268**, 61-66.

128. J. Zeng, Q. Zhang, J. Chen and Y. Xia, *Nano Letters*, 2010, **10**, 30-35.
129. X. Chen, D. Zhao, Y. An, Y. Zhang, J. Cheng, B. Wang and L. Shi, *Journal of Colloid and Interface Science*, 2008, **322**, 414-420.
130. S. E. J. Bell and N. M. S. Sirimuthu, *Journal of Physical Chemistry A*, 2005, **109**, 7405-7410.
131. Y. Lu, Y. Mei, M. Schrunner, M. Ballauff, M. W. Moller and J. Breu, *J. Phys. Chem. C*, 2007, **111**, 7676-7681.
132. D. Astruc, F. Lu and J. R. Aranzaes, *Angewandte Chemie International Edition*, 2005, **44**, 7852-7872.
133. P. L. Kuo, C. C. Chen and M. W. Jao, *J. Phys. Chem. B*, 2005, **109**, 9445-9450.
134. K. Kuroda, T. Ishida and M. Haruta, *J. Mol. Catal. A: Chem.*, 2009, **298**, 7-11.
135. P. A. Padmanabhan, D.-S. Kim, D. Pak and S. J. Sim, *Carbohydrate Polymers*, 2003, **53**, 459-468.
136. J. T. Zhang, G. Wei, T. F. Keller, H. Gallagher, C. Stotzel, F. A. Muller, M. Gottschaldt, U. S. Schubert and K. D. Jandt, *Macromol. Mater. Eng.*, 2010, **295**, 1049-1057.
137. S. Harish, R. Sabarinathan, J. Joseph and K. L. N. Phani, *Mater. Chem. Phys.*, 2011, **127**, 203-207.
138. Y. Mei, Y. Lu, F. Polzer, M. Ballauff and M. Drechsler, *Chem. Mater.*, 2007, **19**, 1062.
139. Y. Q. Ma, J. Z. Yi and L. M. Zhang, *J. Macromol. Sci. Part A-Pure Appl. Chem.*, 2009, **46**, 643-648.
140. S. Panigrahi, S. Kundu, S. K. Ghosh, S. Nath and T. Pal, *Journal of Nanoparticle Research*, 2004, **6**, 411-414.
141. M. Saura-Valls, R. Fauré, S. Ragàs, K. Piens, H. Brumer, T. T. Teeri, S. Cottaz, H. Driguez and A. Planas, *Biochemical Journal*, 2006, **395**, 99 -106.
142. H. C. Kolb, M. G. Finn and K. B. Sharpless, *Angewandte Chemie Int. Ed.*, 2001, **40**, 2004 - 2021.
143. R. E. B. Bruns, I. S. Scarminio and B. d. Barros Neto, *Planejamento e Otimização de Experimentos*, Editora da UNICAMP, Campinas - SP, 1995.
144. A. C. Felipe, I. C. Bellettini, R. Eising, E. Minatti and F. C. Giacomelli, *Journal of the Brazilian Chemical Society*, 2011, **22**, 1539 - 1548.
145. G. Coullerez, P. H. Seeberger and M. Textor, *Macromol. Biosci.*, 2006, **6**, 634-647.
146. X. Wang, O. Ramström and M. Yan, *Advanced Materials*, 2010, **22**, 1946-1953.
147. C. Capello, U. Fischer and K. Hungerbühler, *Green Chemistry*, 2007, **9**, 927-934.
148. Y. F. Yano, *J. Colloid Interface Sci.*, 2005, **284**, 255-259.
149. A. M. Signori, K. d. O. Santos, R. Eising, B. L. Albuquerque, F. C. Giacomelli and J. B. Domingos, *Langmuir*, 2010, **26**, 17772.
150. B. Arnáiz, O. Martínez-Ávila, J. M. Falcon-Perez and S. Penadés, *Bioconjugate Chem.*, 2012, **23**, 814-825.
151. A. L. Brown and A. M. Goforth, *Chem. Mater.*, 2012, **24**, 1599-1605.
152. M. Brust, M. Walker, D. Bethell, D. J. Schiffrin and R. Whyman, *J Chem Soc Chem Comm*, 1994, 801-802.
153. R. Loris, T. Hamelryck, J. Bouckaert and L. Wyns, *Biochimica et Biophysica Acta (BBA) - Protein Structure and Molecular Enzymology*, 1998, **1383**, 9-36.
154. J. R. Kanicky and D. O. Shah, *Langmuir*, 2003, **19**, 2034-2038.
155. C. Guo, P. Boullanger, L. Jiang and T. Liu, *Biosensors and Bioelectronics*, 2007, **22**, 1830-1834.
156. Y.-K. Lyu, K.-R. Lim, B. Y. Lee, K. S. Kim and W.-Y. Lee, *Chemical Communications*, 2008, **0**, 4771-4773.
157. Y. Zhang, S. Luo, Y. Tang, L. Yu, K.-Y. Hou, J.-P. Cheng, X. Zeng and P. G. Wang, *Analytical Chemistry*, 2006, **78**, 2001-2008.
158. D. C. Hone, A. H. Haines and D. A. Russell, *Langmuir*, 2003, **19**, 7141-7144.

159. M. G. Semenova, L. E. Belyakova, Y. N. Polikarpov, M. M. Il'in, T. A. Istarova, M. S. Anokhina and E. N. Tsapkina, *Biomacromolecules*, 2005, **7**, 101-113.
160. H. Sjögren, C. A. Ericsson, J. Evenäs and S. Ulvenlund, *Biophysical Journal*, 2005, **89**, 4219-4233.

8 Appendix

8.1 ANOVA table for AgNPs-Dextran optimization

Table 14. Analysis of variance (ANOVA) for AgNPs-Dextran optimization

Factor	ANOVA; Var.:Resposta; R-sqr=,97762; Adj.:95244 (Otimização1,3) 3 factors, 1 Blocks, 18 Runs; MS Pure Error=,0274187 DV: Resposta				
	SS	df	MS	F	p
(1)Dex molL ⁻¹ (L)	2,72234	1	2,72234	99,288	0,002151
Dex molL ⁻¹ (Q)	0,01118	1	0,01118	0,408	0,568467
(2)AgNO ₃ mmolL ⁻¹ (L)	35,28349	1	35,28349	1286,842	0,000048
AgNO ₃ mmolL ⁻¹ (Q)	0,36783	1	0,36783	13,415	0,035179
(3)NaBH ₄ mmolL ⁻¹ (L)	0,92451	1	0,92451	33,718	0,010166
NaBH ₄ mmolL ⁻¹ (Q)	0,10015	1	0,10015	3,653	0,151953
1L by 2L	1,10475	1	1,10475	40,292	0,007909
1L by 3L	0,29296	1	0,29296	10,685	0,046822
2L by 3L	0,12723	1	0,12723	4,640	0,120234
Lack of Fit	0,85308	5	0,17062	6,223	0,081651
Pure Error	0,08226	3	0,02742		
Total SS	41,79160	17			

8.2 ¹H and ¹³C NMR spectra for synthesized amphiphilic compounds.

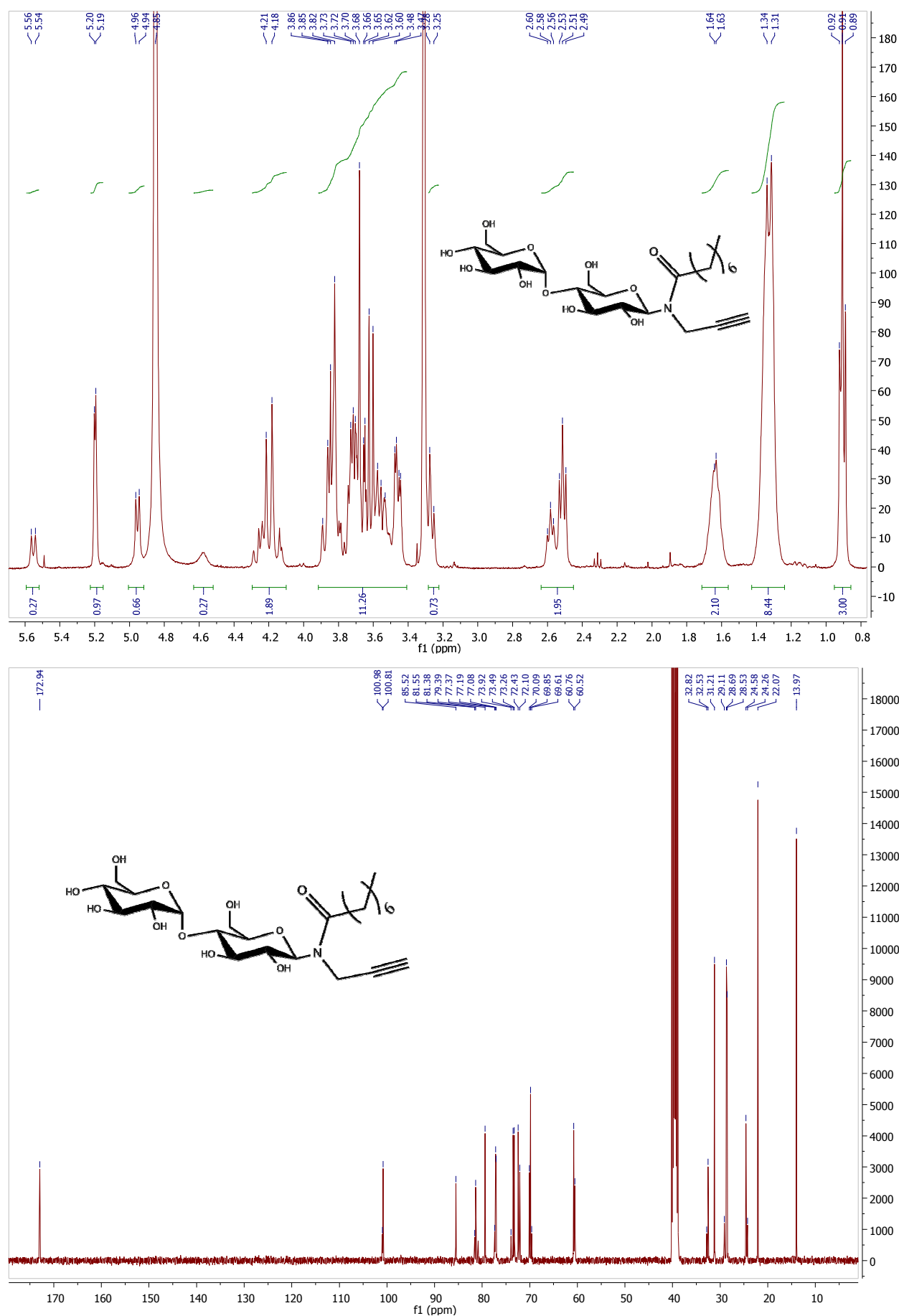


Figure 45. ^1H NMR (top) and ^{13}C NMR (down) of MalNOcta.

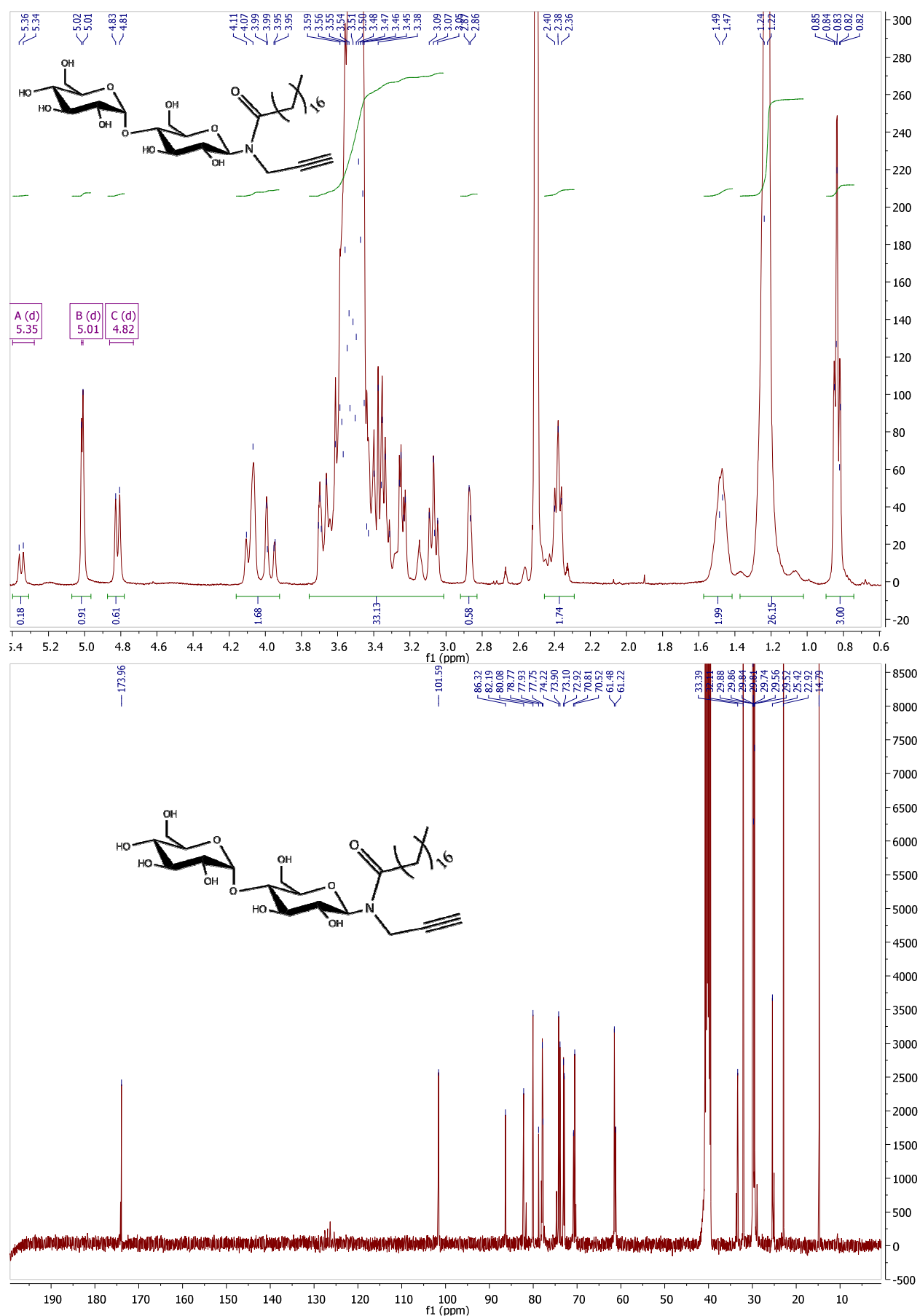


Figure 46. ¹H NMR (up) and ¹³C NMR (down) of MalNOctD.

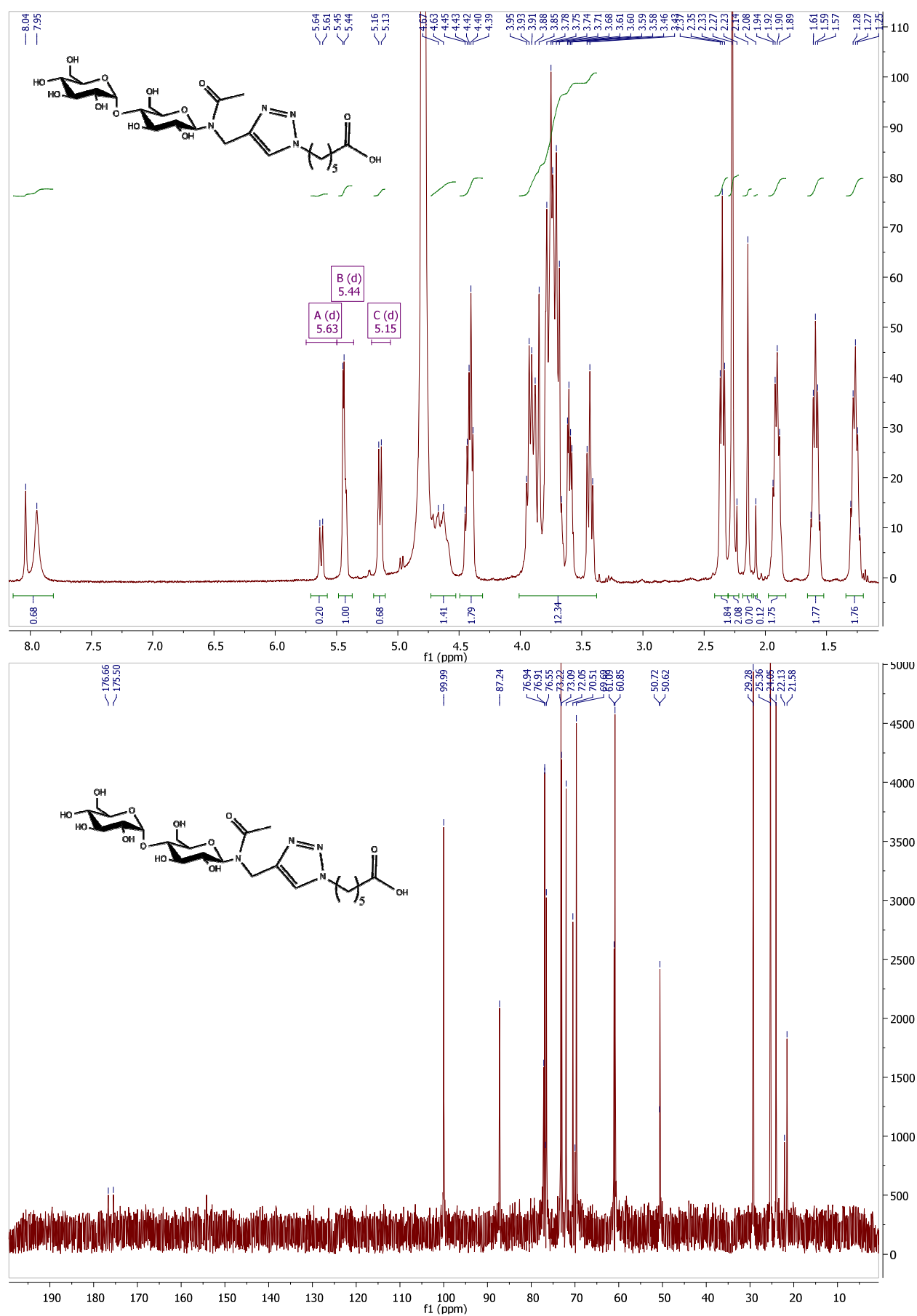


Figure 47. ¹H NMR (top) and ¹³C NMR (down) of MalNacC₆.

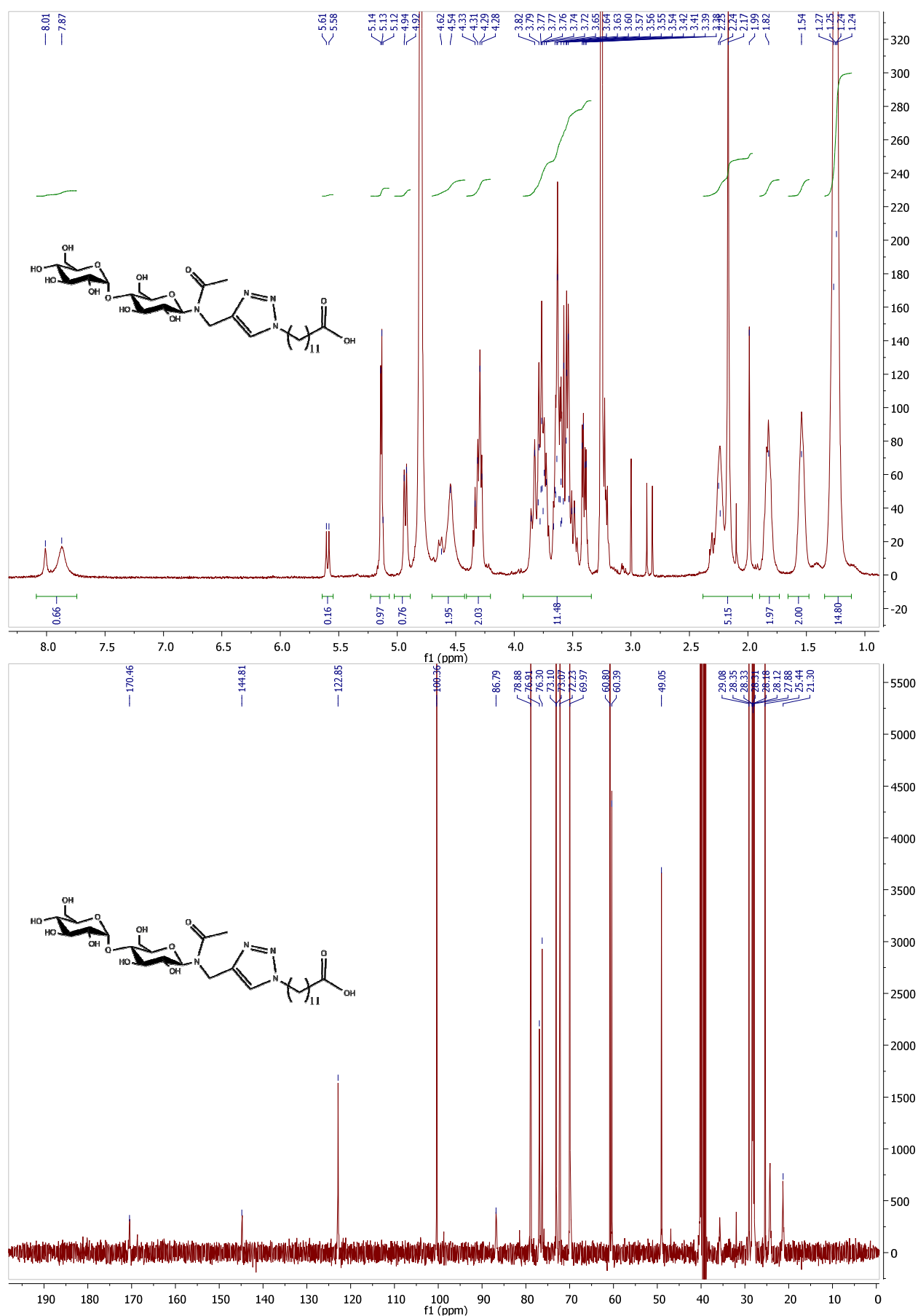


Figure 48. ^1H NMR (top) and ^{13}C NMR (down) of MalNacC₁₂.

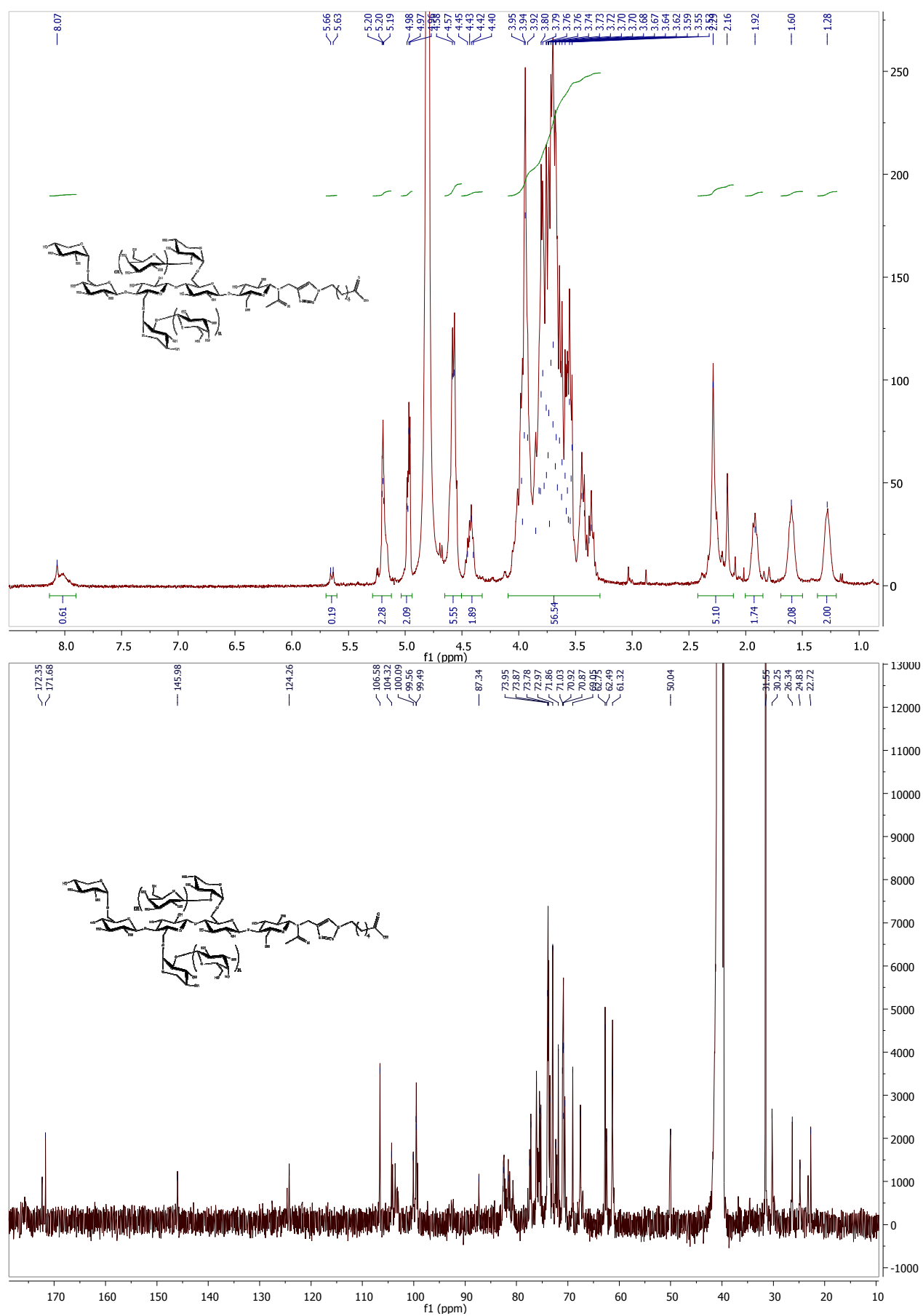


Figure 49. ¹H NMR (top) and ¹³C NMR (down) of XGONAcC₆.

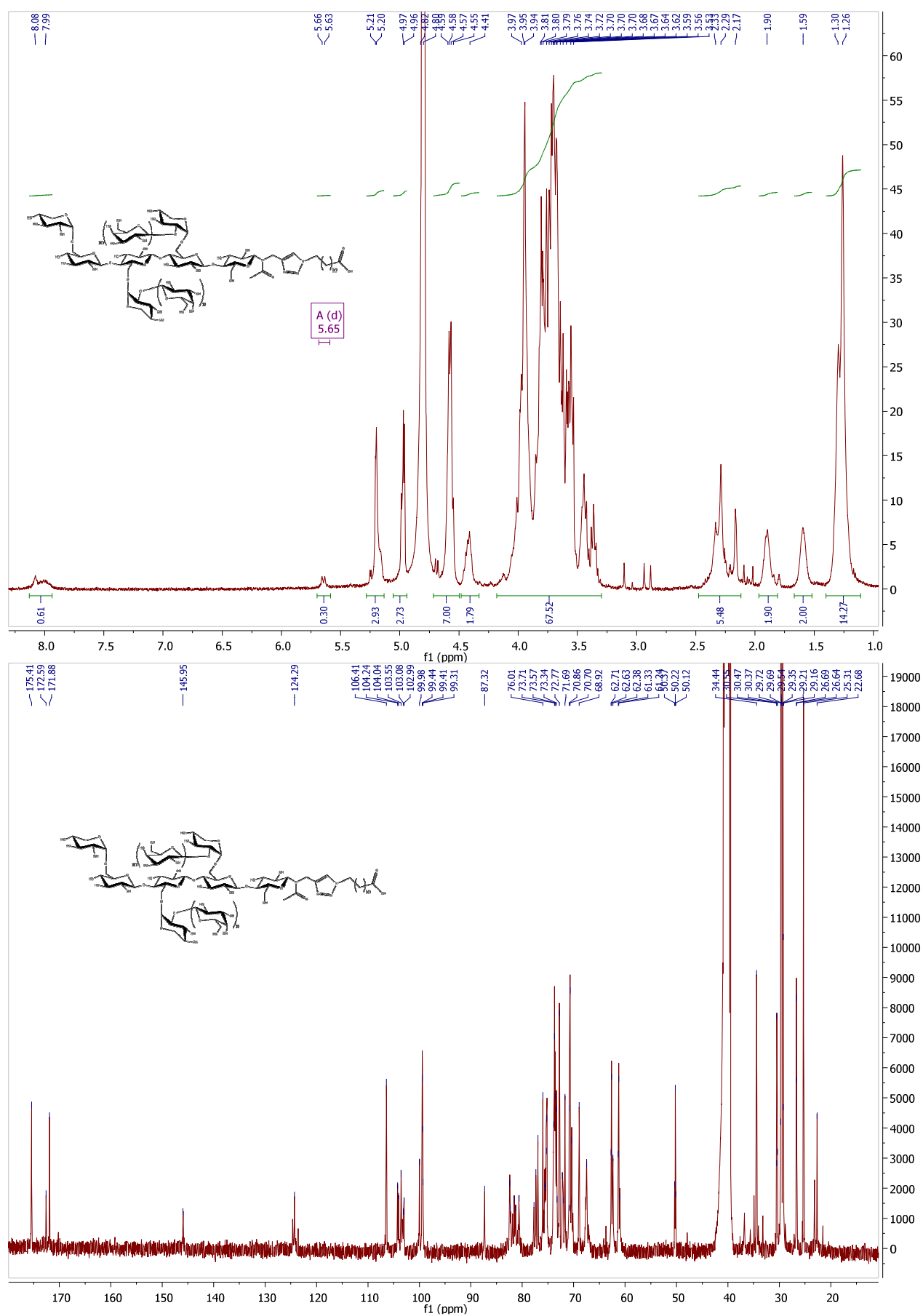


Figure 50. ¹H NMR (top) and ¹³C NMR (down) of XGONAcC₁₂.

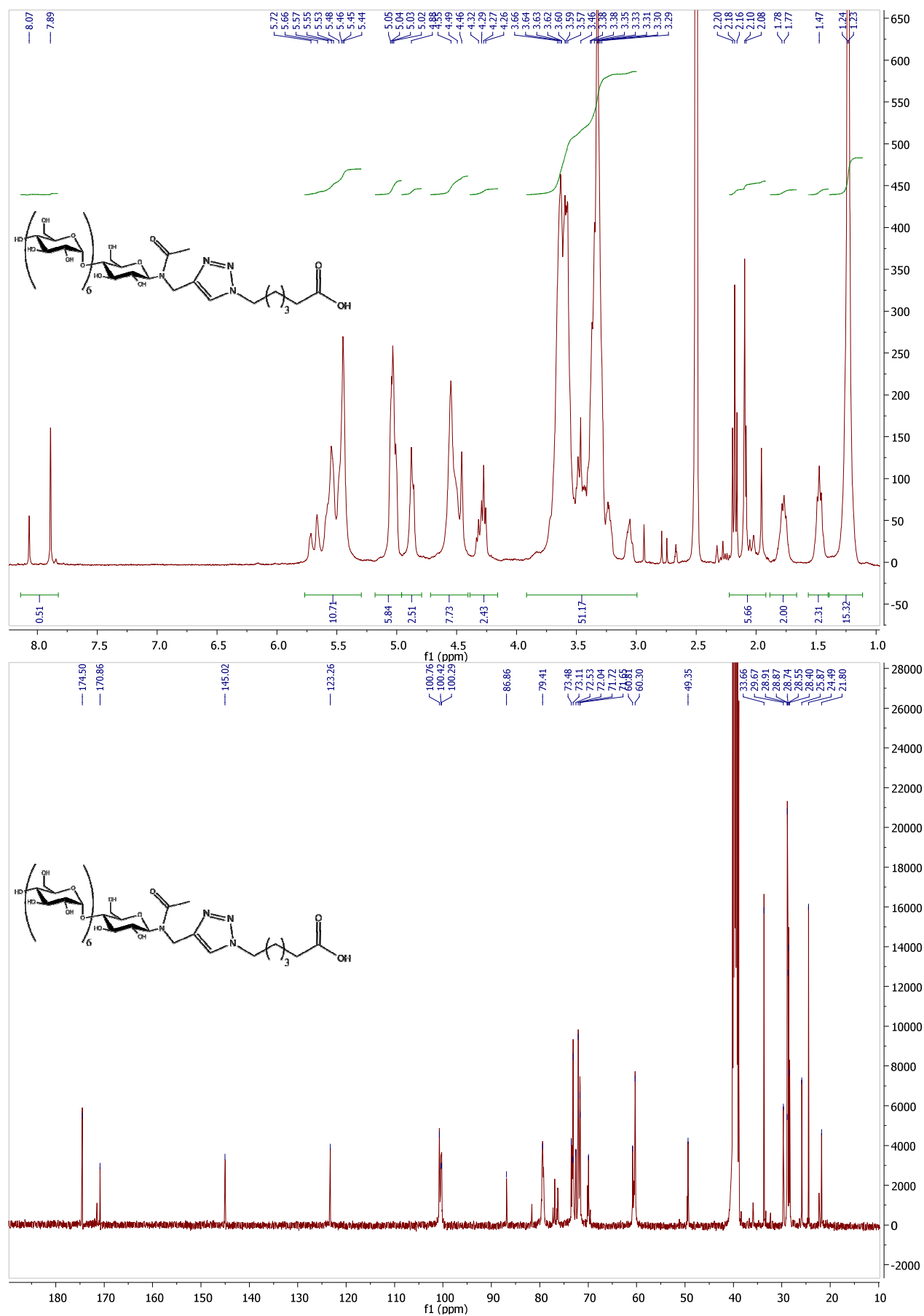


Figure 51. ^1H NMR (top) and ^{13}C NMR (down) of Mal_7NAC_6 .

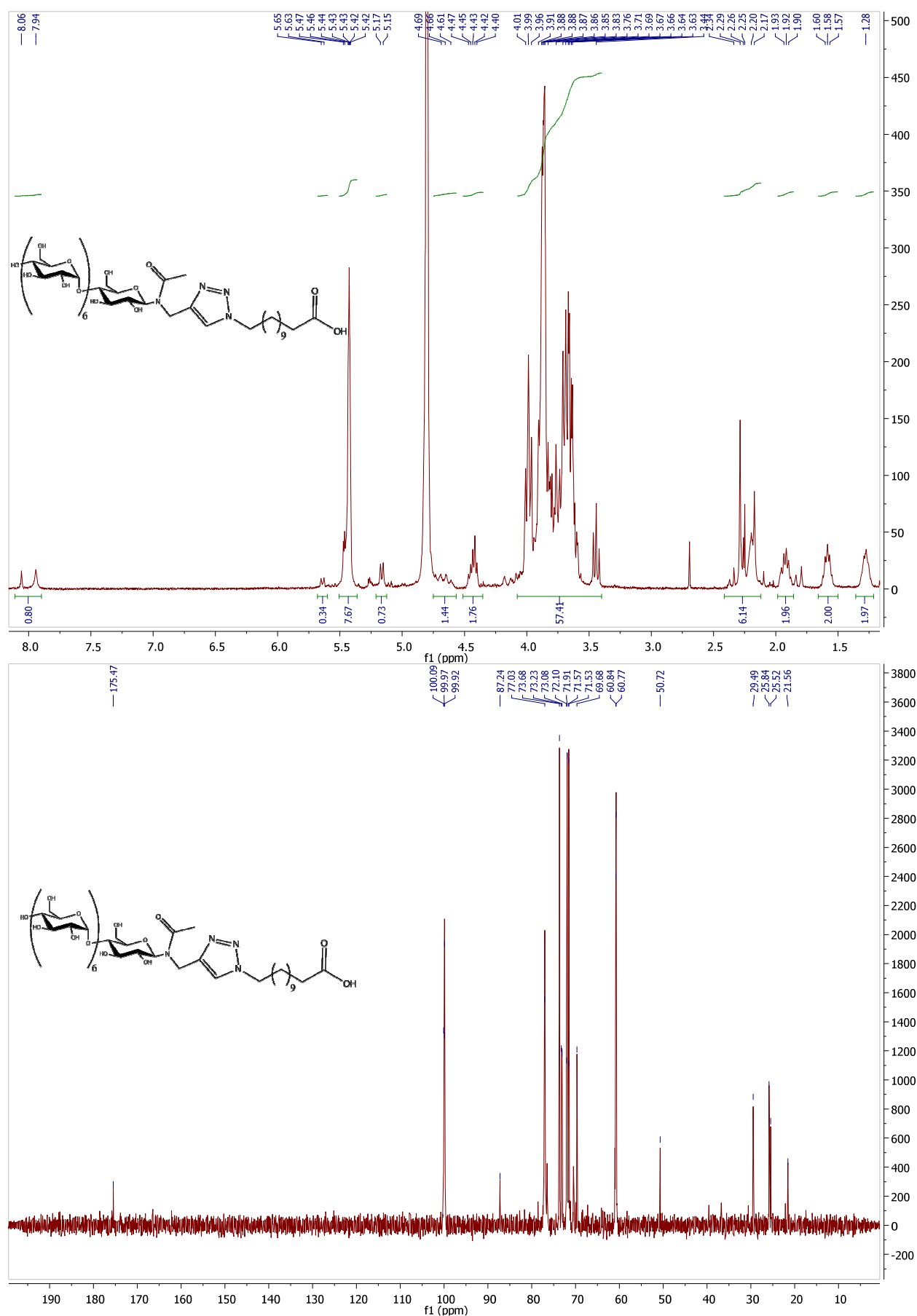


Figure 52. ¹H NMR (top) and ¹³C NMR (down) of Mal₇NAcC₁₂.

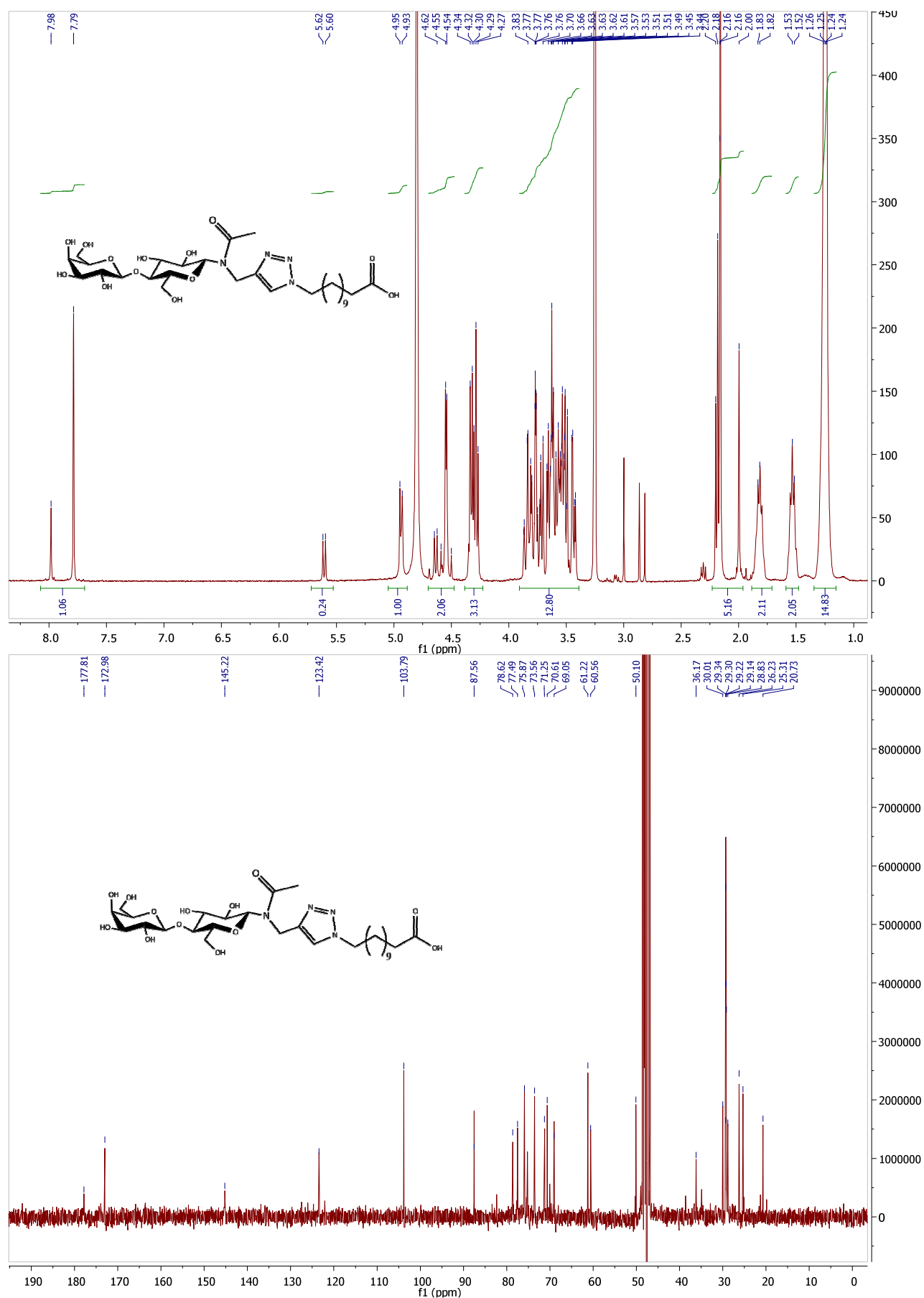


Figure 53. ^1H NMR (left) and ^{13}C NMR (right) of LacNAc $_{12}$.

8.3 ANOVA table for AgNPs-Amphiphilic compounds optimization

Table 15. Analysis of variance (ANOVA) for AgNPs-MalNOctD optimization.

Factor	ANOVA; Var.:Response Nor; R-sqr=0.86998; Adj:0.76163 2 factors, 1 Blocks, 12 Runs; MS Pure Error=0.001383 DV: Response Nor				
	SS	df	MS	F	p
(1)MalNOctD mg mL ⁻¹ (L)	0,004846	1	0,004846	3,5042	0,157947
MalNOctD mg mL ⁻¹ (Q)	0,004422	1	0,004422	3,1973	0,171716
(2)NaBH ₄ x 10 ⁻³ molL ⁻¹ (L)	0,290907	1	0,290907	210,3429	0,000711
NaBH ₄ x 10 ⁻³ molL ⁻¹ (Q)	0,076603	1	0,076603	55,3886	0,005021
1L by 2L	0,003323	1	0,003323	2,4026	0,218910
Lack of Fit	0,052135	3	0,017378	12,5655	0,033216
Pure Error	0,004149	3	0,001383		
Total SS	0,432894	11			

Table 16. Analysis of variance (ANOVA) for AgNPs-MalNacC₁₂ optimization.

Factor	ANOVA; Var.:Response Nor; R-sqr=0.85146; Adj:0.75862 2 factors, 1 Blocks, 14 Runs; MS Pure Error=0.0015161 DV: Response Nor				
	SS	df	MS	F	p
(1)MalNacC ₁₂ mg mL ⁻¹ (L)	0,110706	1	0,110706	73,0190	0,013420
MalNacC ₁₂ mg mL ⁻¹ (Q)	0,108834	1	0,108834	71,7838	0,013646
(2)NaBH ₄ x 10 ⁻³ molL ⁻¹ (L)	0,441927	1	0,441927	291,4840	0,003413
NaBH ₄ x 10 ⁻³ molL ⁻¹ (Q)	0,058705	1	0,058705	38,7200	0,024867
1L by 2L	0,243675	1	0,243675	160,7217	0,006164
Lack of Fit	0,169556	6	0,028259	18,6391	0,051787
Pure Error	0,003032	2	0,001516		
Total SS	1,161875	13			

Table 17. Analysis of variance (ANOVA) for AgNPs-XGONacC₆ optimization.

Factor	ANOVA; Var.:Response Nor; R-sqr=0.99199; Adj:0.98398 2 factors, 1 Blocks, 12 Runs; MS Pure Error=0.0001251 DV: Response Nor				
	SS	df	MS	F	p
(1)Stabilizer mg mL ⁻¹ (L)	0,014734	1	0,014734	117,768	0,008385
Stabilizer mg mL ⁻¹ (Q)	0,156867	1	0,156867	1253,852	0,000797
(2)NaBH ₄ x 10 ⁻³ molL ⁻¹ (L)	0,112377	1	0,112377	898,238	0,001111
NaBH ₄ x 10 ⁻³ molL ⁻¹ (Q)	0,147777	1	0,147777	1181,192	0,000846
1L by 2L	0,027325	1	0,027325	218,409	0,004547
Lack of Fit	0,005074	3	0,001691	13,520	0,069653
Pure Error	0,000250	2	0,000125		
Total SS	0,664764	10			

Table 18. Analysis of variance (ANOVA) for AgNPs-XGONAcC₁₂ optimization.

	ANOVA; Var.:Response Nor; R-sqr=0.98467; Adj:0.9719 2 factors, 1 Blocks, 12 Runs; MS Pure Error=0.0002395 DV: Response Nor				
Factor	SS	df	MS	F	p
(1)XgoNAC ₁₂ mg mL ⁻¹ (L)	0,585261	1	0,585261	2443,563	0,000018
XgoNAC ₁₂ mg mL ⁻¹ (Q)	0,263365	1	0,263365	1099,593	0,000060
(2)NaBH ₄ x 10 ⁻³ molL ⁻¹ (L)	0,023994	1	0,023994	100,179	0,002123
NaBH ₄ x 10 ⁻³ molL ⁻¹ (Q)	0,018725	1	0,018725	78,181	0,003049
1L by 2L	0,002414	1	0,002414	10,078	0,050303
Lack of Fit	0,012924	3	0,004308	17,987	0,020192
Pure Error	0,000719	3	0,000240		
Total SS	0,889994	11			

Table 19. Analysis of variance (ANOVA) for AgNPs-Mal₇NAC₆ optimization.

	ANOVA; Var.:Response Nor; R-sqr=0.98979; Adj:0.98127 2 factors, 1 Blocks, 12 Runs; MS Pure Error=0.0045765 DV: Response Nor				
Factor	SS	df	MS	F	p
(1)Mal ₇ NAC ₆ mg mL ⁻¹ (L)	2,804060	1	2,804060	612,7090	0,000145
Mal ₇ NAC ₆ mg mL ⁻¹ (Q)	0,042868	1	0,042868	9,3670	0,054969
(2)NaBH ₄ x 10 ⁻³ molL ⁻¹ (L)	3,501142	1	3,501142	765,0269	0,000104
NaBH ₄ x 10 ⁻³ molL ⁻¹ (Q)	0,000000	1	0,000000	0,0000	0,999114
1L by 2L	0,013130	1	0,013130	2,8690	0,188874
Lack of Fit	0,051974	3	0,017325	3,7856	0,151580
Pure Error	0,013729	3	0,004576		
Total SS	6,432249	11			

Table 20. Analysis of variance (ANOVA) for AgNPs-Mal₇NAC₁₂ optimization.

	ANOVA; Var.:Response Nor; R-sqr=0.98382; Adj:0.96763 2 factors, 1 Blocks, 12 Runs; MS Pure Error=,0007115 DV: Response Nor				
Factor	SS	df	MS	F	p
(1)Mal ₇ NAC ₁₂ mg mL ⁻¹ (L)	1,145161	1	1,145161	1609,478	0,000621
Mal ₇ NAC ₁₂ mg mL ⁻¹ (Q)	1,019999	1	1,019999	1433,568	0,000697
(2)NaBH ₄ x 10 ⁻³ molL ⁻¹ (L)	0,115049	1	0,115049	161,697	0,006128
NaBH ₄ x 10 ⁻³ molL ⁻¹ (Q)	0,076213	1	0,076213	107,114	0,009207
1L by 2L	0,085993	1	0,085993	120,860	0,008173
Lack of Fit	0,037805	3	0,012602	17,711	0,053917
Pure Error	0,001423	2	0,000712		
Total SS	2,423888	10			

Table 21. Analysis of variance (ANOVA) for AgNPs-LacNAcC₁₂ optimization.

ANOVA; Var.:Response Nor; R-sqr=0.94454; Adj:0.89832 2 factors, 1 Blocks, 12 Runs; MS Pure Error=0.0008002 DV: Response Nor					
Factor	SS	df	MS	F	p
(1)LacNAcC ₁₂ mg mL ⁻¹ (L)	0,601055	1	0,601055	751,0968	0,000107
LacNAcC ₁₂ mg mL ⁻¹ (Q)	0,029501	1	0,029501	36,8649	0,008968
(2)NaBH ₄ x 10 ⁻³ molL ⁻¹ (L)	0,082012	1	0,082012	102,4854	0,002053
NaBH ₄ x 10 ⁻³ molL ⁻¹ (Q)	0,152910	1	0,152910	191,0809	0,000819
1L by 2L	0,023945	1	0,023945	29,9219	0,012010
Lack of Fit	0,048208	3	0,016069	18,0809	0,017288
Pure Error	0,002401	3	0,000800		
Total SS	0,912460	11			

8.4 Response surface for AgNPs-Amphiphilic compounds optimization.

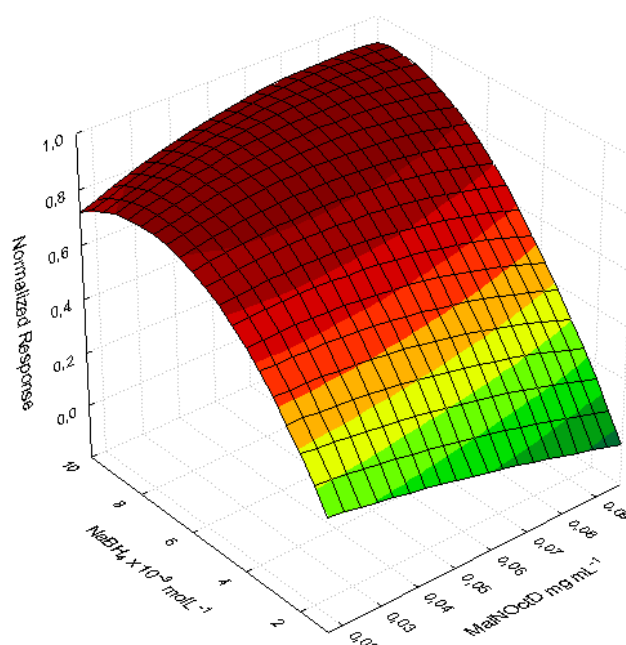


Figure 54. Response surface for MalNOctD.

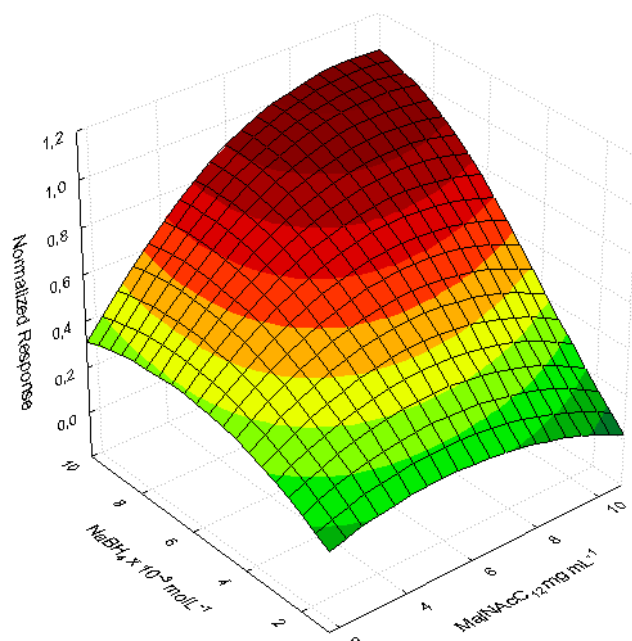


Figure 55. Response surface for MalNAcC₁₂.

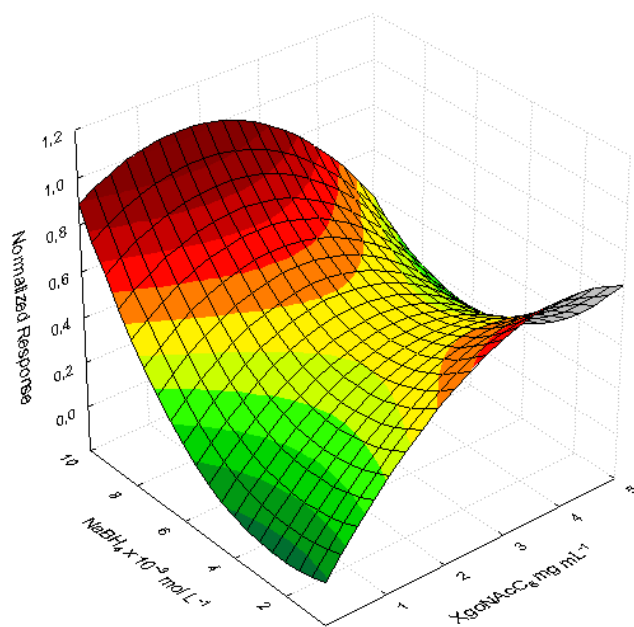


Figure 56. Response surface for XGONAcC₆.

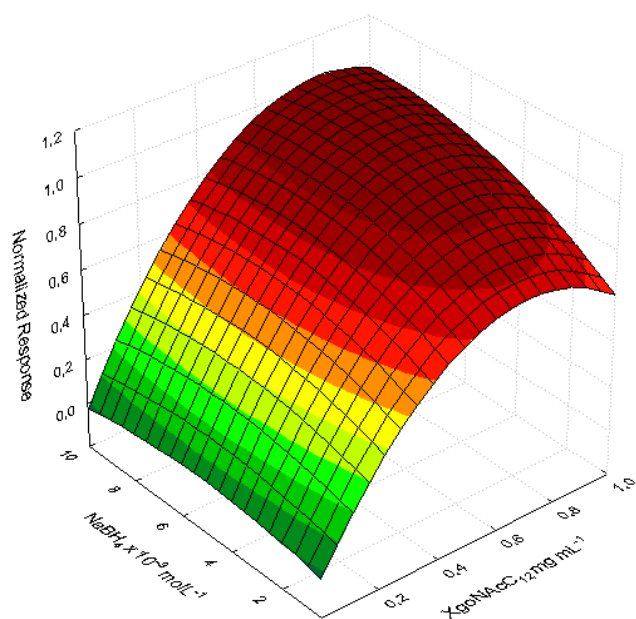


Figure 57. Response surface for XGONAcC₁₂.

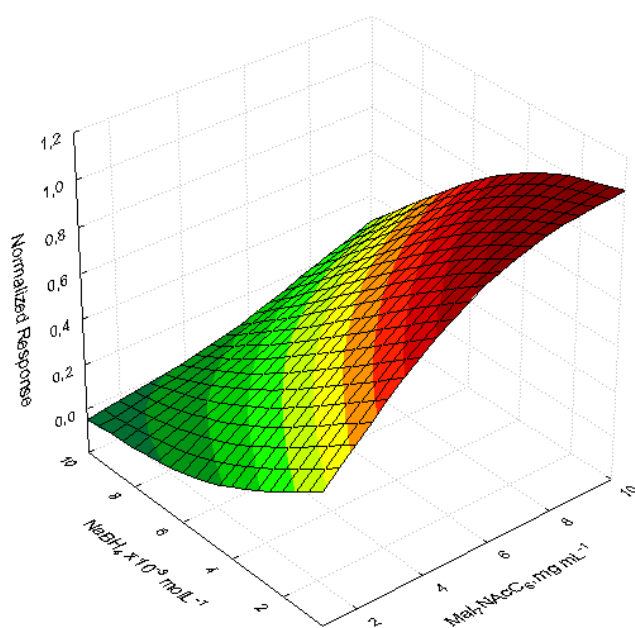


Figure 58. Response surface for Mal₇NAC₆.

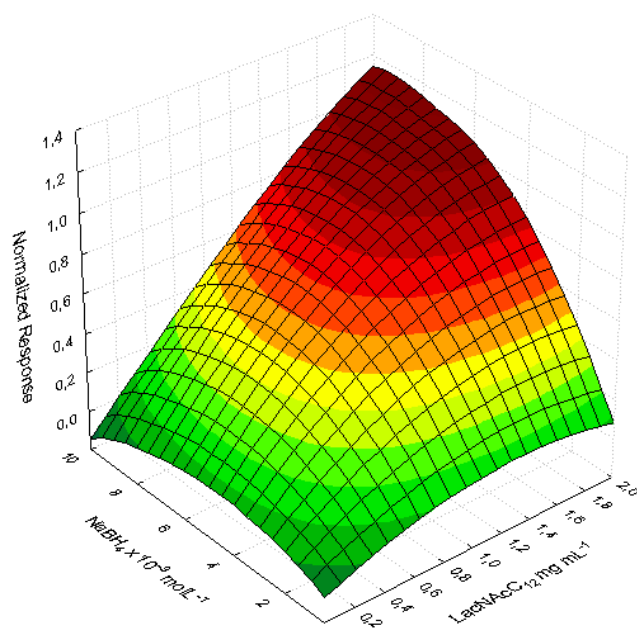


Figure 59. Response surface for LacNAcC₁₂.